Double-Beta Decay of ^{150}Nd to Excited Final States

by

M. F. Kidd

Department of Physics
Duke University

Date: ______________________

Approved:

____
Werner Tornow, Advisor

____
Kate Scholberg

____
Steffen Bass

____
Calvin Howell

____
Ying Wu

Dissertation submitted in partial fulfillment of the requirements for the degree of
Doctor of Philosophy in the Department of Physics
in the Graduate School of Duke University
2010

Abstract

(Double-Beta Decay)

Double-Beta Decay of ^{150}Nd to Excited Final States

by

M. F. Kidd

Department of Physics
Duke University

Date: ______________________

Approved:

____
Werner Tornow, Advisor

____
Kate Scholberg

____
Steffen Bass

____
Calvin Howell

____
Ying Wu

An abstract of a dissertation submitted in partial fulfillment of the requirements for
the degree of Doctor of Philosophy in the Department of Physics
in the Graduate School of Duke University
2010

Abstract

An experimental study of the two-neutrino double-beta ($2\nu\beta\beta$) decay of ^{150}Nd to various excited final states of ^{150}Sm was performed at Triangle Universities Nuclear Laboratory (TUNL). Such data provide important checks for theoretical models used to predict $0\nu\beta\beta$ decay half lives.

The measurement was performed at the recently established Kimballton Underground Research Facility (KURF) in Ripplemeade, Virginia using the TUNL-ITEP double-beta decay setup. In this setup, two high-purity germanium detectors were operated in coincidence to detect the deexcitation gamma rays of the daughter nucleus. This coincidence technique, along with the location underground, provides a considerable reduction in background in the regions of interest.

This study yields the first results from KURF and the first detection of the coincidence gamma rays from the 0_1^+ excited state of ^{150}Sm. These gamma rays have energies of 334.0 keV and 406.5 keV, and are emitted in coincidence through a $0_1^+ \rightarrow 2_1^+ \rightarrow 0_{gs}^+$ transition. The enriched Nd_2O_3 sample obtained from Oak Ridge National Laboratory consists of 40.13 g ^{150}Nd. This sample was observed for 391 days, producing 29 raw events in the region of interest. This count rate gives a half life of $T_{1/2} = (0.72^{+0.36}_{-0.18} \pm 0.04(syst.)) \times 10^{20}$ years, which agrees within error with another recent measurement, in which only the single deexcitation gamma rays were detected (*i.e.*, no coincidence was employed). Lower limits were also obtained for decays to higher excited final states.

To Kenneth P. Kidd

Contents

List of Tables

List of Figures

List of Abbreviations and Symbols

Symbols

β	beta, as in beta decay
$\beta\beta$	double-beta (decay)
$2\nu\beta\beta$	two-neutrino double-beta (decay)
$0\nu\beta\beta$	neutrinoless double-beta (decay)
ECEC	double electron capture
Z	number of protons in a nucleus
N	number of neutrons in a nucleus
A	mass number of nucleus corresponding to $Z + N$

Abbreviations

ADC	Analog-to-Digital Converter
DAQ	Data-Acquisition
HPGe	High-Purity Germanium
ITEP	Institute for Theoretical and Experimental Physics
KURF	Kimballton Underground Research Facility
LBCF	Low Background Counting Facility
LN	Liquid Nitrogen
m.w.e.	Meters Water Equivalent
NaI	Sodium Iodide

Nd_2O_3	Neodymium Oxide
NME	Nuclear Matrix Elements
NSM	Nuclear Shell Model
OFHC	Oxygen Free High Conductivity
PMT	Photomultiplier Tube
QRPA	Quasi-Random Phase Approximation
ROI	Region of Interest
SNO	Sudbury Neutrino Observatory
SNO+	The next phase of the Sudbury Neutrino Observatory
TAC	Time-to-Amplitude Converter
TUNL	Triangle Univerisities Nuclear Laboratory
UPS	Uninterruptible Power Supply

Acknowledgements

I would like to thank several people for their assistance with this experiment: Bret Carlin, Richard O'Quinn, Chris Westerfeldt, John Dunham and Patrick Mulkey. Without their input, especially on the planning and execution of the move to Kimballton, my life would have been much harder. James Esterline has put in valuable time helping me with both theory and experimental questions. Thank you, Brenda West, for handling the multitude of trips I have taken to Blacksburg, VA. I'm also grateful for Dr. Alexander Barabash and Dr. Vladimir Umatov of ITEP for their input regarding the efficiency determination. I appreciate the shared trips to Kimballton and help with filling LN dewars over the last two years from the UNC collaboration at Kimballton, specifically Reyco Henning, Sean MacMullin, Paddy Finnerty, Graham Giovanetti, and Jacquie Strain. Finally, I would like to thank Dr. Bruce Vogelaar at Virginia Tech for the immense amount of hard work which brought about the existence of the Kimballton Underground Research Facility.

More personally, there are a number of people who have provided moral support throughout my time here. Thanks go to Joel Greenberg, Julie Keys, Jonathan Cranford, James Esterline (again!), Kristine Callan, Leah Broussard, Brian Bunton and others over the years. My wonderful family has always stood behind me, supported me, and inspired me. Thanks, Mom, for being unfailingly encouraging.

Finally, I would like to thank Dr. Werner Tornow who I have had the privilege to work with for the past six years. I could not have asked for a better advisor!

1

Introduction

In this thesis, a study of the rate of the double-beta decay of ^{150}Nd to excited final states of ^{150}Sm will be described. This work took place both at Triangle Universities Nuclear Laboratory (TUNL) and at the recently established Kimballton Underground Research Facility (KURF). The main motivation for studying double-beta decay is clear: to shed light upon the nature of the neutrino. Though much has been discovered in the field of the neutrino since its conception and later discovery, some very basic traits remain unknown. Two of these are the Majorana or Dirac nature of the neutrino, and the particle's mass. Observation of neutrinoless double-beta decay would answer the question of the nature of the neutrino while simultaneously determining the mass, assuming the nuclear matrix elements for that particular nuclear transitions are known. Here, the study of two-neutrino double-beta decay can prove useful by providing experimental data which can be used to test and calibrate theoretical models. This chapter will further motivate the experiment by expanding upon these issues.

1.1 Background

1.1.1 Neutrino History

The history of the neutrino is intimately connected with one of the earliest observed nuclear phenomena. This discovery was the emission of electrons from a nucleus, known as beta (β) decay. The simplest picture of β decay consists of the transformation of a nuclear neutron into a proton with the release of an electron. In the 1920s, physicists were puzzled when they observed the electron's continuous energy spectrum. This spectrum consisted of electrons with energies ranging from zero to the endpoint energy, the difference in energies of the initial and final atomic states. In 1931, Pauli proposed that the missing energy could be accounted for by introducing a second particle in the decay process. To conserve charge, the particle would be neutral. In addition, angular momentum considerations set the spin of the particle to be $\frac{1}{2}$. Later, Fermi called this particle the *neutrino*. Beta decay in the nucleus can be written as

$$^{A}_{Z}X_{N} \rightarrow_{Z+1}^{A} X'_{N-1} + e^{-} + \bar{\nu}_{e}. \tag{1.1}$$

A related process, involving the emission of a positron, e^{+}, was observed in 1934 by the Joliot-Curies and can be written as

$$^{A}_{Z}X_{N} \rightarrow_{Z-1}^{A} X'_{N+1} + e^{+} + \nu_{e}. \tag{1.2}$$

Building on Pauli's neutrino hypothesis, Fermi developed a theory of beta decay in 1934 [33]. Using Fermi's theory, Bethe and Peierls showed that the neutrino's interaction with matter was so small as to be insignificant. About this conclusion Pauli famously said, "I have done a terrible thing. I have postulated a particle that cannot be detected." [42] Experimental evidence for the existence of the neutrino remained elusive until the 1950s. In 1951, Reines and Cowan proposed an experiment to directly detect electron anti-neutrinos by observing their capture by protons. They realized they could utilize the newly developed organic scintillating liquids to build the massive detector which would be needed for such a rarely interacting particle. After considering placing the detector near an atomic-bomb explosion, they instead decided to install it near an operating nuclear reactor. Though their first attempts were foiled by cosmic-ray backgrounds, they succeeded in 1956 when they observed the interaction in Equation 1.3 [12].

$$\bar{\nu}_e + p \rightarrow e^+ + n \tag{1.3}$$

The positron annihilated with an atomic electron almost immediately, producing two 511 keV gamma rays. Within 10 ms the neutron was captured by a cadmium nucleus dissolved in a water tank, producing more gamma rays. By detecting both gamma-ray bursts in delayed coincidence in the surrounding scintillator, the interaction was confirmed [12].

Following this success, the muon neutrino was discovered in 1962 by Lederman, Schwarz, and Steinberger at Brookhaven National Laboratory. They used the Alternating Gradient Synchrotron to produce intense, high-energy beams of protons. These protons were impinged upon a beryllium target to produce pions and kaons. These particles were then allowed to decay, producing neutrinos and other charged particles. The charged particles were absorbed in 12 meters of steel shielding, while the neutrinos continued to the detection chamber, which was a 10-ton spark chamber consisting of aluminum plates. It was still at that point unknown as to whether the neutrinos produced in muon interactions were different from the neutrinos produced in electron interactions. In this experiment, it was thought that if the neutrinos were distinct, those neutrinos produced from the kaon or pion decays would interact in the aluminum and produce long muon tracks. Their results showed that the neutrinos which were produced with muons were distinct from those produced with electrons. Afterward, the terms "electron-neutrino" and "muon-neutrino" began to be used [12].

Not until 2000 was it announced that the tau neutrino was experimentally verified by the DONUT group of Fermilab [36]. DONUT, which stands for Direct Observation of NU Tau, is a detection system consisting of a series of emulsion targets followed by a spectrometer. An 800 GeV beam of protons produced in the TeVatron at Fermi National Accelerator Laboratory was collided into a block of tungsten to create the charm meson D_s, composed of charm and strange quarks. D_s decays to tau lepton and an anti-tau neutrino. The tau lepton has a lifetime of 2.9×10^{-13} s, and decays with a 17.85% branching ratio to a tau neutrino, electron and electron anti-neutrinos, and with a 17.36% branching ratio to a tau neutrino, muon and muon anti-neutrino; the rest of the time it decays via hadrons and a tau neutrino. The tau neutrinos interact with the silver bromide crystals suspended in the emulsion sheets. In the emulsion sheet, this looks like a primary interaction vertex with a bend in one of the tracks, signifying the decay of a tau lepton [38].

The field of neutrino physics was not in stasis during this 40-year period. Attempts to observe solar neutrinos were spearheaded by Davis and Bahcall in the 1950s and 1960s. The first results from their Homestake detector were published in 1968. According to solar models, their result for neutrino flux from the sun was quite difference from the predicted value. This discrepancy became known as the solar neutrino problem. The next generation of solar neutrino detectors, which relied on neutrino capture by gallium, confirmed the discrepancy [18]. Neutrino oscillations, first suggested by Pontecorvo in 1958, provided an explanation. Once they were confirmed by Super-Kamiokande in 1998, neutrinos were known to have mass (See Section 1.1.3).

1.1.2 The Standard Model and the Neutrino

Also during this time, a new picture of subatomic physics was being developed, which became known as the Standard Model of particle physics. This model categorized the fundamental spin $\frac{1}{2}$ particles, the six quarks and six leptons, as the constituents of all matter. The leptons consist of the charged electron, muon, and tau, and the neutral neutrinos, which come in three ”flavors”, electron, muon, and tau. The quarks carry a fractional charge; up, charmed and top carry a charge of $+\frac{2}{3}|e|$, and down, strange and bottom carry a charge of -$\frac{1}{3}|e|$. The Standard Model also details the interactions between these particles. These interactions are mediated by characteristic bosons. The quarks interact via the strong force, which is mediated by the exchange of the gluon. Though leptons do not experience the strong force, both quarks and leptons are subject to the electroweak force. Electromagnetic interactions are mediated by photon exchange, and weak interactions are mediated by the $W^{\pm}$ and Z^0 bosons. Finally, gravitational interactions involve all particles, and is theorized to be mediated by the exchange of a spin-2 boson, the graviton [40].

This organizational work culminates in the arrangement of the lepton and quark pairs into generations by mass hierarchy:

$$M_{1^{st}} = \begin{pmatrix} u \\ d \\ e^- \\ \nu_e \end{pmatrix} \quad M_{2^{nd}} = \begin{pmatrix} c \\ s \\ \mu^- \\ \nu_\mu \end{pmatrix} \quad M_{3^{rd}} = \begin{pmatrix} t \\ b \\ \tau^- \\ \nu_\tau \end{pmatrix}. \tag{1.4}$$

Note that each multiplet contains two leptons and two quarks. The first generation contains the lightest quarks, charged leptons and possibly, the lightest neutrino. These particles compose all stable matter.

The Standard Model is one of the most successful physics models, and it is interesting to discuss its features and predictions. Some properties include separate lepton- and baryon-number conservation, left-handed charged-current interactions,

First Generation		Second Generation		Third Generation	
Particle	Mass	Particle	Mass	Particle	Mass
u	2.4 MeV	c	1.27 GeV	t	171.2 GeV
d	4.8 MeV	s	104 MeV	b	4.2 GeV
e^-	0.511 MeV	μ^-	105.7 MeV	τ^-	1.777 GeV
ν_e	<2.2 eV	ν_μ	<0.17 MeV	ν_τ	<15.5 MeV

Table 1.1: Summary of the masses of the fundamental particles in the Standard Model.

and positron-proton charge equivalence. Addressing the neutrino, the Standard Model does not include a neutrino mass, nor right-handed neutrinos or left-handed anti-neutrinos. Some predictions include the stability of the proton and it forbids neutrinoless double-beta decay. Free parameters in the Standard Model include the quark, charged lepton, and gauge boson masses, as well as the coupling constants and quark-mixing parameters. These parameters have been determined by experimental modern physics.

Even though the Standard Model assumes a neutrino mass of zero, it can accommodate a non-zero mass in a way similar to the mixing matrix in the quark sector. An examination of the first generation column in Table 1.1 raises significant questions. The masses of the charged constituents of the multiplet are within a certain range, the electron neutrino is at least 5 or 6 orders of magnitude lighter, a difference in mass scale so far unexplained.

One possible explanation for this mass-scale difference is called the see-saw mechanism. First, a review of the neutrino mass problem in the Glashow-Weinberg-Salam (GWS) theory is needed. In GWS theory, the first generation of quarks and leptons are represented as shown in Equation 1.5.

$$\begin{pmatrix} u_\alpha \\ d_\alpha \end{pmatrix}_L, u_{\alpha R}, d_{\alpha R}, \begin{pmatrix} \nu_e \\ e^- \end{pmatrix}_L, e^-_R. \tag{1.5}$$

Here, α =1,2,3 is a color index and $L(R)$ are the chiral projections. In this representation, the neutrino must be massless because the Dirac mass term cannot be present as there is no ν_R, and there can be no Majorana mass term because the theory implies lepton conservation. To include neutrino mass at the electroweak level, extensions must be applied.

The left- and right-handed components of a Dirac four-spinor is defined as $\psi_{L,R} = [(1 \mp \gamma_5)/2]\psi$. Only left-handed neutrinos interact in the Standard Model, but since they are neutral, there is another way to construct a left-handed neutrino field. Independent neutrino fields which are their own antiparticles (Majorana particles) can be defined as seen in Equation 1.6.

$$\nu = \frac{\psi_L + (\psi_L)^c}{\sqrt{2}}, X = \frac{\psi_R + (\psi_R)^c}{\sqrt{2}}. \tag{1.6}$$

The most general mass term in the Lagrangian couples these two fields to themselves and each other, and takes the form

$$\mathcal{L}_M = -M_L \bar{\nu}\nu - M_R \bar{X} X - M_D(\bar{\nu} X + \bar{X}\nu). \tag{1.7}$$

M_L and M_R are known as Majorana masses for the ν and X fields and M_D is the Dirac mass, coupling the two fields. In the generic case of N flavors of neutrinos, these can be arranged in a matrix.

$$\mathcal{L}_M = -(\bar{\nu}\bar{X})\mathcal{M}\left(\begin{array}{c} \nu \\ X \end{array}\right) \quad \mathcal{M} = \left(\begin{array}{c} \mathcal{M}_L \mathcal{M}_D^T \\ \mathcal{M}_D \mathcal{M}_R \end{array}\right). \tag{1.8}$$

Now, the matrices $\mathcal{M}_L, \mathcal{M}_R$ and $\mathcal{M}_D$ are $N \times N$. If $\mathcal{M}_L$ and $\mathcal{M}_R$ are zero, then the ν field pairs with the X field to form N Dirac neutrinos.

Another such extreme also explains the mass-scale difference referenced a few paragraphs earlier. This extreme is known as the see-saw mechanism formulated by Gell-Mann, Ramond, and Slanksky and Yanagida (see [8] and references therein). Dropping down to the simpler one flavor, if $M_L << M_D << M_R$, then the eigenstates are Majorana neutrinos with the lightest mass being $m \sim M_D^2/M_R$.

1.1.3 Mass Searches

Neutrino mass searches have been ongoing almost since the particle's proposal. The search has been explored from many different angles, but they all fall into two categories: direct and indirect. Direct measurements utilize information gleaned from careful decay kinematics observations or time-of-flight measurements of supernova neutrinos incident on the large neutrino detectors scattered around the globe.

Upper limits on the mass of the electron neutrino were set as early as 1948 using the endpoint of the beta-decay spectrum [12]. Fermi realized early on that if the neutrino were to have a rest mass, it would change the location of the endpoint of the beta-decay energy spectrum, as well as the shape of the beta-decay energy spectrum. Measuring this change is extremely difficult due to the low statistics near the endpoint. For several reasons, tritium is an excellent nucleus for this experiment. Because of its small decay energy of 18.6 keV, the endpoint and shaping would be affected more if a finite neutrino mass existed [18]. Also, the beta decay of tritium is superallowed, it has simple nuclear properties, and simple atomic structure. The first such measurement by Curran, Angus, and Cockroft set a limit of $M_{\nu_e} < 1$ keV. The current best upper limit using this strategy is 2.3 eV by the Mainz collaboration in 2005 [34]. Though massive improvements in this measurement have been made over the past 60 years, a more sensitive means of measuring the neutrino mass is needed.

Other direct methods include muon momentum measurements from pion decay, and invariant-mass studies of multi-particle semileptonic decays of the τ. Also, time of flight measurements were done when Supernova 1987A occurred.

A strength of direct measurements lies in the very few theoretical assumptions of neutrino properties made. In contrast, indirect measurements of neutrino mass through methods such as neutrinoless double-beta decay or cosmological calculations require many theoretical assumptions. Neutrinoless double-beta decay requires lepton number nonconservation, and cosmological estimates depend on the models employed.

1.1.4 The Majorana Question

The neutrino, as the only neutral fermion, raises an interesting possibility. In the Standard Model, the charged fermions are all Dirac particles, with distinct antiparticles. The massless, neutral neutrinos are represented by Weyl spinors. With the revelation that neutrinos are not massless, a different representation must be adopted. So far, since the other fermions in the Standard Model are Dirac particles, neutrinos were also classified as Dirac. Therefore, a right-handed neutrino and left-handed antineutrino exist, but do not interact.

An alternative was suggested in 1937 by Italian physicist Majorana; the neutrino is its own antiparticle. This is only possible if the particle is charge neutral to satisfy CPT invariance. As discussed in Section 1.1.2, the Standard Model treats neutrinos as massless and left-handed, and anti-neutrinos are massless and right-handed. Thus, the only distinction between the two are their assigned lepton numbers. If neutrinos are Majorana particles, lepton number is not a conserved quantity.

Visualizing the Difference

Following the arguments of Kayser laid out by Boehm and Vogel [8], start by assuming the existence of a left-handed neutrino which has mass, ν_ℓ. If CPT invariance is assumed, then there must also exist ν_ℓ's CPT image, a right-handed anti-neutrino, $\bar{\nu_r}$. Because ν_ℓ is massive, it travels slower than light, and a reference frame exists

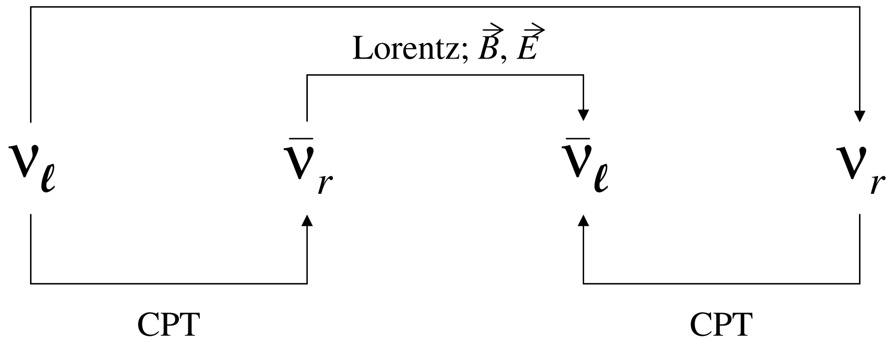

FIGURE 1.1: The four distinct states of the Dirac neutrino [8].

that is faster than ν_ℓ. From the view of this frame, ν_ℓ is going in the other direction, yet its spin remains the same. Thus, it is now seen to be a right-handed neutrino, ν_r, in the Lorentz-transformed frame. ν_r also has its own CPT image, $\bar{\nu_\ell}$. The question is whether ν_r is identical to $\bar{\nu_r}$, the CPT image of ν_ℓ. If they are distinct, there exist four distinct states with the same mass, and this is called the Dirac neutrino. If they are not distinct, then there exist only two states: a Majorana neutrino.

In the case of a Dirac neutrino, it may have a magnetic and electric dipole moment, and so the helicity state can by altered by a Lorentz transformation as stated above, and also by the torque exerted by an external $\overrightarrow{E}$ or $\overrightarrow{B}$ field. However, in the case of a Majorana neutrino, the magnetic and electric dipole moments must vanish. Consider a neutrino at rest in an external static field. Its interaction energy would be $-\mu < \overrightarrow{s} \cdot \overrightarrow{B} > -d < \overrightarrow{s} \cdot \overrightarrow{E} >$, where $\overrightarrow{s}$ is the neutrino spin operator, and μ and d are the magnetic and electric dipole moments, respectively. Performing a CPT transformation results in the Majorana spin vector changing direction, but no change to the $\overrightarrow{E}$ and $\overrightarrow{B}$ fields. If CPT invariance must hold, μ and d must vanish accordingly [8].

Though it is now shown that neutrinos are massive particles, it is still interesting to note that the difference between Majorana and Dirac neutrinos vanishes as the

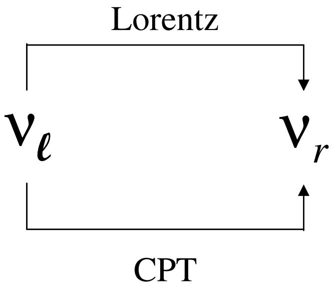

FIGURE 1.2: The two distinct states of the Majorana neutrino [8].

mass approaches zero. Referring to the above visualization, with a massless neutrino, the helicity state could not be altered with a Lorentz transformation since the neutrino would be traveling at the speed of light. Furthermore, the dipole moment would vanish as it is proportional to mass. The states $|\nu_\ell >$ and $|\bar{\nu_r} >$ become decoupled from the other two states, $|\bar{\nu_\ell} >$ and $|\nu_r >$. The latter states cannot interact via the weak interaction, and may as well not exist. Thus, only two states are apparent, and they cannot be differentiated from the two Majorana states.

Measuring the Difference

One possibility for determining the Majorana/Dirac nature of the neutrino other than neutrinoless double beta-decay is through electromagnetic properties. As discussed above, though they are electrically neutral, Dirac neutrinos can have a non-zero magnetic and electric dipole moment. In contrast, Majorana neutrinos must have no magnetic and electric dipole moment. Another option for distinguishing between Majorana and Dirac neutrinos relies on neutrino decay and neutrino-electron scattering. However, it seems that the simplest, most elegant experimental method for determining the neutrino's nature is neutrinoless double-beta decay, described in the following section.

1.2 Double-Beta Decay

Beta decay, as discussed in Section 1.1.1, is a general term for any nuclear decay process which changes a proton into a neutron, or a neutron into a proton, keeping the same mass number, A. Fermi's theory of beta decay, developed in 1934, treats the beta decay as a transition probability between initial and final states which interact weakly. This treatment results in Fermi's Golden Rule, which says any transition rate is proportional to the weak coupling strength and the density of final states available. Using this rule, beta decay is a first-order process. Double-beta ($\beta\beta$) decay is a rare process by which Z changes by two units, while A remains constant. This process is therefore a second-order process in Fermi's calculations.

Due to both the weak coupling constant and the fact that it is a higher-order process, double-beta decay has an extremely long half-life; it is usually on the order of 10^{20}-10^{23} years. Such a rare decay process is consequently very difficult to detect. Regular β decay normally dominates in most nuclei. However, there are some nuclei in which β decay is not possible due to energy considerations, and experimentalists capitalize on this property in double-beta decay detection experiments.

Recall the functional dependence of atomic mass M_A on the nuclear charge Z. Near its minimum, it can be approximated by a parabola with Equation 1.9,

$$M_A(Z,A) = constant + 2b_{sym}\frac{(A/2-Z)^2}{A^2} + b_{Coul}\frac{Z^2}{A^{1/3}} + m_e Z + \delta, \tag{1.9}$$

where the symmetry energy coefficient, b_{sym}, is about 50 MeV, and the Coulomb energy coefficient, b_{Coul}, is on the order of 0.7 MeV. In this case, the $m_e Z$ term, which is the binding energy of the electrons, is small and can be ignored. Finally, δ is the nuclear pairing term, and represents the increased binding which occurs when like pairs of nucleons are coupled with zero angular momentum. δ is approximately given by $\pm 12/A^{1/2}$ MeV for the cases of odd N and odd Z, or even N and even Z.

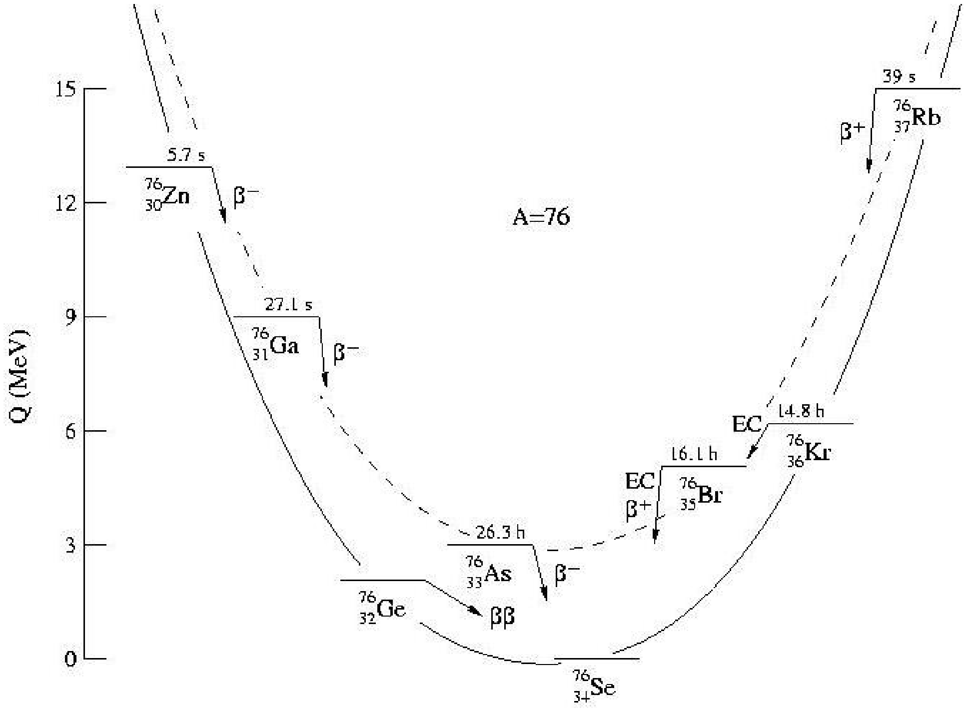

FIGURE 1.3: The parabola which represents the dependence of atomic mass on nuclear charge. The two parabolas represent the two values available to the pairing term in equation 1.9 [8].

For odd A, δ is zero [8]. Because of the pairing term, there exist two parabolas for even values of A, as can be seen in Figure 1.3.

Here, ^{76}Ge cannot simply β decay to ^{76}As because of energy considerations. Instead, the nuclear charge changes by two units as it decays by the second order weak process known as double-beta decay. For odd A, the pairing term is the same for odd-even and even-odd nuclei and so only a single parabola exists. Thus, as seen in Figure 1.3, double-beta decay occurs in nuclei which have even Z and N. Since the ground states of all even-even nuclei are 0^+, the transitions are predominantly

$0^+ \rightarrow 0^+$.

1.2.1 Double-Beta Decay Modes

The possible modes of double-beta decay are listed in Equations 1.10-1.13, with e_b representing a bound electron.

$$
\begin{aligned}
{}^A_Z X_N &\rightarrow {}_{Z+2}^{A} X_{N-2} + e^- + e^- + \bar{\nu_e} + \bar{\nu_e}, && (1.10)\\
{}^A_Z X_N &\rightarrow {}_{Z-2}^{A} X_{N+2} + e^+ + e^+ + \nu_e + \nu_e, && (1.11)\\
{}^A_Z X_N + e_b^- &\rightarrow {}_{Z-2}^{A} X_{N+2} + e^+ + \nu_e + \nu_e, && (1.12)\\
{}^A_Z X_N + e_b^- + e_b^- &\rightarrow {}_{Z-2}^{A} X_{N+2} + \nu_e + \nu_e. && (1.13)
\end{aligned}
$$

These modes are basically analogous to single-beta decay, positron decay, and electron capture. The interaction expressed in Equation 1.10 is what is normally referred to as two-neutrino double-beta ($2\nu\beta\beta$) decay, and is subject to the condition:

$$M_A(Z,A) > M_A(Z+2,A). \tag{1.14}$$

For practical consideration, it can also be required that single-beta decay is suppressed either by $M_A(Z,A) < M_A(Z+1,A)$, or by other means. These modes of double-beta decay were first laid out in 1935 by Goeppert-Mayer [21]. In the years following, Majorana [35], Racah [41], and Furry [19] began to explore another mode of double-beta decay. This fifth mode is available if the following sequence in Equation 1.15, known as the Racah sequence, is considered.

$$
\begin{aligned}
n_1 \rightarrow p_1 + e_1^- + \quad &{}''\nu''\\
&{}''\nu'' \quad + n_2 \rightarrow p_2 + e_2^-,
\end{aligned}
\tag{1.15}
$$

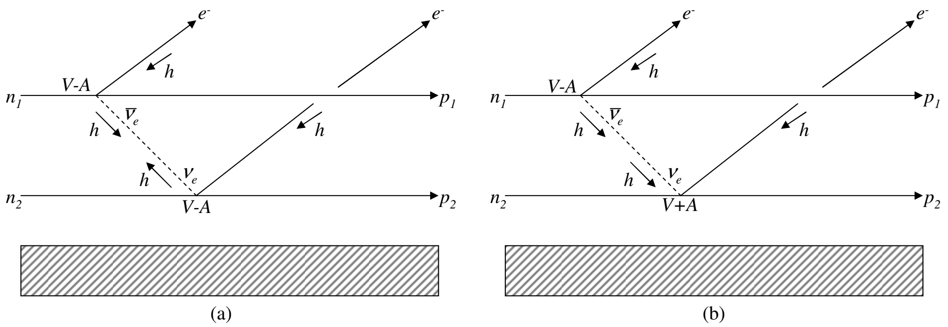

(a) (b)

FIGURE 1.4: In this $0\nu\beta\beta$ decay schematic, the arrows represent the neutrino helicity [8].

This process, known as neutrinoless double-beta ($0\nu\beta\beta$) decay, can occur only if the neutrino emitted in the first step, an electron anti-neutrino, is identical to the neutrino captured in the second step, an electron neutrino. If the neutrino is a Dirac particle, this process will not proceed. Also, if the neutrino is a massless particle, the sequence will not occur. There is also a helicity mismatch in the Racah sequence. The anti-neutrino emitted in the first interaction is right-handed, but the neutrino absorbed in the second interaction needs to be left-handed for the sequence to proceed. Finally, $0\nu\beta\beta$ decay violates lepton number conservation. Thus, observing $0\nu\beta\beta$ decay would be evidence of physics beyond the standard model [8].

1.2.2 Double-Beta Decay Candidates

Now that these conditions for double-beta decay are defined, the nuclei which can undergo double-beta decay processes can be identified. There are 35 nuclei that undergo the mode in Equation 1.10, but only 11 have a Q value which is practical for experimental use. This Q-value restriction is about 2 MeV; below that, such a rare decay could get swamped by natural radiation. These 11 nuclei are listed in Table 1.2. Note that only one of the nuclei has a natural abundance greater than about 12 percent. The Q value is also a very important consideration regarding the

Double-beta decay Candidates	Q-Value (keV)	Natural Abundance (%)	$(G^{2\nu})^{-1}$	$(G^{0\nu})^{-1}$
^{48}Ca→^{48}Ti	4271 ± 4	0.187	2.52E16	4.10E24
^{76}Ge→^{76}Se	2039.6 ± 0.9	7.8	7.66E18	4.09E25
^{82}Se→^{82}Kr	2995 ± 6	9.2	2.30E17	9.27E24
^{96}Zr→^{96}Mo	3350 ± 3	2.8	5.19E16	4.46E24
^{100}Mo→^{100}Ru	3034 ± 6	9.6	1.06E17	5.70E24
^{110}Pd→^{110}Cd	2013 ± 19	11.8	2.51E18	1.86E25
^{116}Cd→^{116}Sn	2802 ± 4	7.5	1.25E17	5.28E24
^{124}Sn→^{124}Te	2288.1 ±1.6	5.64	5.93E17	9.48E24
^{130}Te→^{130}Xe	2533 ± 4	34.5	2.08E17	5.89E24
^{136}Xe→^{136}Ba	2479 ± 8	8.9	2.07E17	5.52E24
^{150}Nd→^{150}Sm	3367.1 ± 2.2	5.6	8.41E15	1.25E24

Table 1.2: Double-beta decay candidates (with Q-values greater than 2 MeV) and their characteristics. The quantities $G^{2\nu}$ and $G^{0\nu}$ will be further discussed in Section 2.3.1.

decay rate, as will be shown in Section 2.2. The quantities $(G^{2\nu})^{-1}$ and $(G^{0\nu})^{-1}$, given in Table 1.2 will also be explained later, and they have a large effect on the decay rates for $2\nu\beta\beta$ decay and $0\nu\beta\beta$ decay as well.

For a double-beta decay experiment, selection of the best nucleus is very important. As mentioned earlier, Q value is an important consideration, but not the only one. Other quantities which can be considered in order to maximize the experiment's success in detecting double-beta decay include natural abundance, availability of the isotope, possibility of enrichment, and source cost. Many of these quantities are entwined. To optimize the source efficiency, the number of isotope nuclei must be maximized, which is heavily dependent on the abundance, enrichment possibility, and availability of the isotope. These factors can all also affect the source cost.

Of the 11 aforementioned nuclei, the double-beta decay to the ground state of nine has been measured: ^{48}Ca, ^{76}Ge, ^{82}Se, ^{96}Zr, ^{100}Mo, ^{116}Cd, ^{128}Te, ^{130}Te, ^{150}Nd, and (not listed in Table 1.2) ^{238}U (see [3] for an excellent compilation of these results). However, the neutrinoless mode has not yet been observed.

Excited-State Decays

As well as transitions to the ground state, transitions to various excited states are also possible. Detection of double-beta decay to the ground state requires either detection of the final nucleus, or the emitted electrons, which is not always an easy task (See Section 3.1). With a decay to an appropriate excited final state, however, the characteristic de-excitation gamma rays create a very nice signal. In addition to the emitted electrons, detecting the gamma rays in coincidence can greatly reduce the background. Sometimes even the emitted electrons need not be detected for a clear signal; the discrete gamma-ray energies provide a much more clear-cut signal than the electron spectrum. Detecting only the gamma rays also allows more freedom in source material. When the electrons need to be detected, the source must be extremely thin so as to minimize the attenuation of the electrons. Electrons in the energy range involved in double-beta decay have an interaction length on the order of millimeters, thus the source thicknesses must be well below this thickness. When detecting only the gamma rays, the sources can be much thicker, resulting in a much higher number of potential nuclei. However, depending on the energy of the excited state, the half life for transitions to excited states are an order of magnitude larger than those to the ground state. Of course, double-beta decay data to excited states cannot distinguish between $0\nu\beta\beta$ and $2\nu\beta\beta$ modes of decay.

Studying double-beta decay to excited states can supplement knowledge of double-beta decay in general. The main focus, in terms of neutrinoless double-beta decay, is the experimental determination of the nuclear matrix elements. As will be further discussed in Sections 2.2 and 2.3, the knowledge of the nuclear matrix elements have a large impact on the extent of the information which can be gleaned from measuring neutrinoless double-beta decay. Another motivation for excited-state studies involves detecting neutrinoless double-electron capture to an excited state. There is possibly

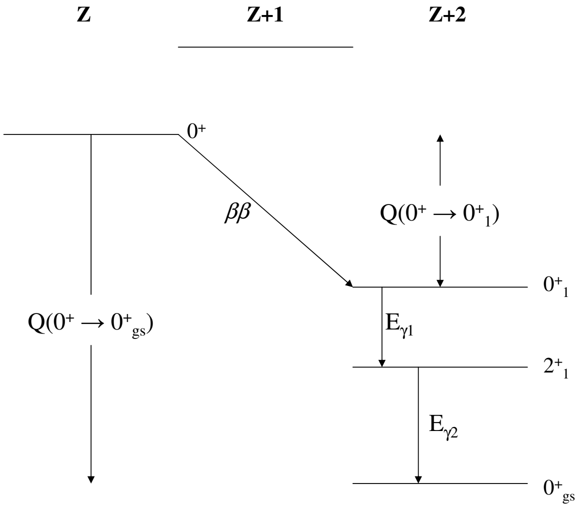

FIGURE 1.5: Generic decay scheme for double-beta decay to an excited final state, and the subsequent $\gamma - \gamma$ cascade.

a resonance condition which exists when the excited final state is within less than 100 eV of the mass difference. In this case, the effective Majorana neutrino mass can be probed with high sensitivity. (See [27] and references therein for more details.)

The most probable excited states to be accessed by double-beta decay are the 0^+_1 states. The 2^+_1 state in Figure 1.5 can also be populated, but not only is it strongly suppressed, but it also is very difficult to detect due to the single-gamma emission and low energy of the level. The 0^+_1 state decays will be the main focus of the remaining discussion.

If a 0^+_1 state is populated by double-beta decay, the nucleus will de-excite via gamma-ray emission. Due to the angular momentum selection rules, $0^+ \rightarrow 0^+$ transitions are suppressed. However, as shown in Figure 1.5, there is often an intermediate 2^+ state which can facilitate the decay. Thus, there is a de-excitation $0^+ \rightarrow 2^+ \rightarrow 0^+$

sequence producing two characteristic gamma rays which are essentially in coincidence.

The first nucleus studied using the TUNL-ITEP double-beta decay setup was ^{100}Mo. (See [23] and [28] for further details.) The nucleus which will be more fully discussed in Chapter 3 is ^{150}Nd. ^{150}Nd was also previously studied by the TUNL-ITEP double-beta decay setup, but no enriched sample was available, and only a half-life limit of the decay to the first excited 0_1^+ state was established. However, as will be discussed, an enriched sample of ^{150}Nd was obtained to improve this limit or, if possible, to determine a value for the half life for this transition.

2

Theory

In this chapter, the process of determining neutrino properties from the $0\nu\beta\beta$-decay rate will be discussed. This decay rate is only as useful as the certainty of nuclear structure properties associated with the decay. Thus, the experimental link between $0\nu\beta\beta$ decay and $2\nu\beta\beta$ decay is established through these nuclear properties. To illuminate this, the decay rates are calculated for single-beta decay, $2\nu\beta\beta$ decay, and $0\nu\beta\beta$ decay. Methods used to explore and calculate nuclear structure properties involved in these decays will be discussed. Information obtained from the $2\nu\beta\beta$-decay mode can be used to clarify these procedures for $0\nu\beta\beta$ decay.

2.1 Beta-Decay Rate

Before calculating the decay rates for $2\nu\beta\beta$ and $0\nu\beta\beta$ decay, it is useful to go through the exercise with β decay. The first step is to start with Fermi's Golden Rule, which relates the decay rate, λ to the nuclear matrix element, $\langle\phi_k(\overrightarrow{r})|H_\beta|\phi_0(\overrightarrow{r})\rangle$ and the density of states, $\rho(E_f)$, shown in Equation 2.1.

$$d\lambda = \frac{2\pi}{\hbar}|\langle\phi_k(\overrightarrow{r})|H_\beta|\phi_0(\overrightarrow{r})\rangle|^2\rho(E_f)\delta(E_0 - E_\nu - E_e). \tag{2.1}$$

Here, $|\phi_0(\overrightarrow{r})\rangle = |J_i M_i \zeta\rangle$ is the initial state, which is simply the parent nucleus with angular momentum quantum numbers J_i and M_i and with ζ denoting quantum numbers besides J and M but also associated with angular momentum. Also, E_0 is the maximum possible energy carried by the electron. Then, $E_0 = E_e + E_\nu$ where E_e is the kinetic energy of the electron and E_ν is the kinetic energy of the neutrino. E_0 is more commonly known as the Q value. The final state, $|\phi_k(\overrightarrow{r})\rangle$, is more complicated as it consists of the daughter nucleus, electron, and electron anti-neutrino. For the time being, the Coulomb effect of the daughter nucleus on the electron will be ignored. The wavefunctions of the electron and neutrino are then described by plane waves with respective momenta $\mathbf{k_e}$ and $\mathbf{k}_\nu$.

$$|\phi_k(\overrightarrow{r})\rangle = \frac{1}{\sqrt{V}}e^{i\mathbf{k_e}\cdot\mathbf{r}}\frac{1}{\sqrt{V}}e^{i\mathbf{k}_\nu\cdot\mathbf{r}}|J_f M_f \xi\rangle. \tag{2.2}$$

Now, $|J_f M_f \xi\rangle$ describes the final state of the nucleus with angular momentum quantum numbers J_f, M_f, and ξ. Here, V is a volume used to normalize the wavefunction. Let $k = |\mathbf{k_e} + \mathbf{k}_\nu|$ and θ be the angle between $\mathbf{k}$ and $\mathbf{r}$. Then, expand the product of the exponentials in terms of Legendre polynomials and Bessel functions,

$$|\phi_k(\overrightarrow{r})\rangle = \frac{1}{V}\sum_{\ell=0}^{\infty}(2\ell+1)i^\ell J_\ell(kr)P_\ell(\cos\theta)|J_f M_f \xi\rangle. \tag{2.3}$$

The operator H_β must have the following properties. In β decay, the neutron is changed to a proton. At the quark level, this is equivalent to changing a down quark to an up quark. Thus, the beta-decay operator must have an isospin-raising operator. To have the correct properties of the weak interaction, there must be an axial-vector component to the operator which will be represented by the spin operator multiplied by the isospin-raising operator. Each component of the operator has an associated coupling strength, G_V and G_A respectively. The above relations can now be used to calculate the matrix elements.

$$\begin{aligned}\langle \phi_k(\overrightarrow{r})|H_\beta|\phi_0(\overrightarrow{r})\rangle = \quad & \langle J_i M_i \zeta| \textstyle\sum_{j=1}^{A}(G_V \hat{\tau}_+(j) + G_A \hat{\sigma}(j)\hat{\tau}_+(j)) \\ & \cdot \tfrac{1}{V} \textstyle\sum_{\ell=0}^{\infty}(2\ell+1) i^\ell j_\ell(kr) P_\ell(\cos\theta)|J_f M_f \xi\rangle. \end{aligned} \tag{2.4}$$

The leading-order terms corresponding to $\ell = 0$ in the expression in Equation 2.4 describe "allowed" decays, and the higher-order terms describe "forbidden" decays. These forbidden decays are suppressed in β decay and even more so in double-beta decay, thus they will be ignored.

$$\langle \phi_k(\overrightarrow{r})|H_\beta|\phi(\overrightarrow{r})\rangle_{allowed} =$$

$$\frac{1}{V}\langle J_i M_i \zeta| \sum_{j=1}^{A}(G_V \hat{\tau}_+(j) + G_A \hat{\sigma}(j)\hat{\tau}_+(j)) \frac{\sin(kr)}{kr}|J_f M_f \xi\rangle. \tag{2.5}$$

Furthermore, the $\frac{\sin(kr)}{kr}$ term is typically kept only to leading order,

$$\langle \phi_k(\overrightarrow{r})|H_\beta|\phi(\overrightarrow{r})\rangle_{allowed} \approx$$

$$\frac{G_V}{V}\langle J_i M_i \zeta| \sum_{j=1}^{A}(\hat{\tau}_+(j) + g_A \hat{\sigma}(j)\hat{\tau}_+(j))|J_f M_f \xi\rangle, \tag{2.6}$$

with $g_A = \frac{G_A}{G_V} \approx 1.26$ for nuclear systems. The first term corresponds to Fermi decay and the second to Gamow-Teller decay.

Finally, the density of final states, $\rho(E_f)$ must be computed. The neutrino rarely interacts with the surrounding matter and can be described as a free particle. Statistical mechanics for a free particle says that for a given momentum p_ν, the number of states with that momentum is given by Equation 2.7. The V in Equation 2.7 is the same as the one used to normalize the wavefunction.

$$dn_\nu = \frac{V}{2\pi^2\hbar^3} p_\nu^2 dp_\nu. \tag{2.7}$$

By utilizing Equation 2.7 and $E_\nu^2 = m_\nu^2 + p_\nu^2$, and after integrating over the delta function, dn_ν can be written as seen in Equation 2.8.

$$n_\nu = \frac{V}{2\pi^2\hbar^3}(E_0 - E_e)\{(E_0 - E_e)^2 - m_\nu^2\}^{1/2}. \tag{2.8}$$

Because of the Coulomb interaction, the electron cannot be regarded as a free particle. This can be accounted for by a correction factor, $F(Z, E_e)$, which is included in a free particle density of states of the electron with momentum p_e as seen in Equation 2.9.

$$dn_e = \frac{V}{2\pi^2\hbar^3} F(Z, E_e) p_e^2 dp_e. \tag{2.9}$$

Now, everything can be substituted into Equation 2.1.

$$\begin{aligned} d\lambda = \; & \tfrac{G_V^2}{2\pi^3\hbar^7}\{\langle J_i M_i \zeta | \textstyle\sum_{j=1}^{A}(\hat{\tau}_+(j))|J_f M_f \xi\rangle_F^2 + \langle J_i M_i \zeta | \textstyle\sum_{j=1}^{A}(g_A \hat{\sigma}(j)\hat{\tau}_+(j))|J_f M_f \xi\rangle_{GT}^2\} \\ & \cdot (E_0 - E_e)\{(E_0 - E_e)^2 - m_\nu^2\}^{1/2} F(Z, E_e) p_e^2 dp_e. \end{aligned} \tag{2.10}$$

Performing the final integration over p_e requires the use of the dimensionless Fermi integral, which is defined below in Equation 2.11.

$$f(Z, E_0) \equiv \int F(Z, E_e)\left(\frac{p_e}{m_e}\right)^2 \frac{(E_0 - E_e)}{m_e^3}\sqrt{(E_0 - E_e)^2 - m_\nu^2}\, dp_e. \tag{2.11}$$

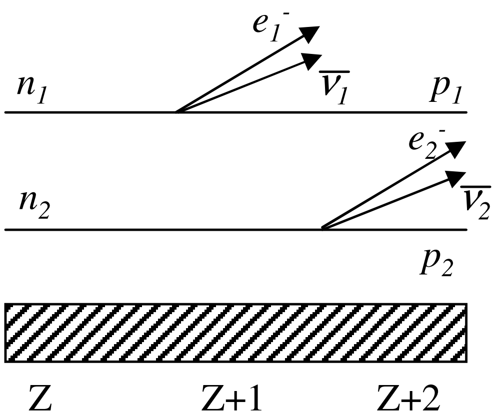

FIGURE 2.1: Diagram for $2\nu\beta\beta$ decay in the two-nucleon mechanism, where the cross-hatched bar represents the spectator nucleons in the nucleus.

Finally, the decay rate for single-beta decay is shown in Equation 2.12.

$$\begin{aligned}\lambda = \ & \tfrac{G_V^2 m_e^5}{2\pi^3\hbar^7} f(Z,E_0)\{\langle J_i M_i \zeta | \textstyle\sum_{j=1}^{A}(\hat{\tau}_+(j))|J_f M_f \xi\rangle_F^2 \\ & +\langle J_i M_i \zeta | \textstyle\sum_{j=1}^{A}(g_A \hat{\sigma}(j)\hat{\tau}_+(j))|J_f M_f \xi\rangle_{GT}^2\}. \end{aligned} \tag{2.12}$$

2.2 Two Neutrino Double-Beta Decay Rate

The two neutrino mode of double-beta decay is a second-order weak decay and is represented in the diagram shown in Figure 2.1. As before with single-beta decay, Fermi's Golden Rule will be implemented, but now the second-order form is required (see Equation 2.13).

$$d\lambda = 2\pi\delta(E_0 - \sum_f E_f)\left|\sum_{m,\beta}\frac{\langle f|H_\beta|m\rangle\langle m|H^\beta|i\rangle}{E_i - E_m - p_\nu - E_e}\right|^2. \tag{2.13}$$

Here, E_i, E_m, and E_f are the initial, intermediate, and final nuclear energies. The states labeled $|m\rangle$ represent the intermediate nuclear states. The matrix elements can be split into Fermi and Gamow-Teller components. The cross-terms vanish when summed over. The Fermi matrix elements ($M_F^{2\nu}$) and Gamow-Teller matrix elements ($M_{GT}^{2\nu}$) are shown in Equation 2.14 and 2.15 respectively.

$$M_F^{2\nu} = \sum_m \frac{\langle f| \sum_\ell \tau_\ell^+ |m\rangle \langle m| \sum_k \tau_k^+ |i\rangle}{E_m - (M_i + M_f)/2}, \tag{2.14}$$

$$M_{GT}^{2\nu} = \sum_m \frac{\langle f| \sum_\ell \sigma_\ell \tau_\ell^+ |m\rangle \cdot \langle m| \sum_k \sigma_k \tau_k^+ |i\rangle}{E_m - (M_i + M_f)/2}. \tag{2.15}$$

As with single-beta decay, the density of states is dominated by the neutrinos and electrons. Since there are two pairs of identical particles emitted, there is a factor of $\frac{1}{4}$ in front (see Equation 2.16).

$$\rho(E_f) = \frac{1}{4} \left(\frac{V}{2\pi^2 \hbar^3} p_{\nu_1}^2 dp_{\nu_1} \right) \left(\frac{V}{2\pi^2 \hbar^3} p_{\nu_2}^2 dp_{\nu_2} \right)$$
$$\left(\frac{V}{2\pi^2 \hbar^3} F(Z, E_{e_1}) p_{e_1}^2 dp_{e_1} \right) \left(\frac{V}{2\pi^2 \hbar^3} F(Z, E_{e_2}) p_{e_2}^2 dp_{e_1} \right). \tag{2.16}$$

Now the decay rate can be written as follows in Equation 2.17,

$$\lambda = \frac{G_V^4 m_e^{11}}{32\pi^7 \hbar^{12}} |M_F^{2\nu} - M_G^{2\nu} T|^2 f^{2\nu\beta\beta}(Z, E_0), \tag{2.17}$$

with

$$f^{2\nu\beta\beta}(Z, E_0) = \frac{1}{m_e^{11}} \int_0^{E_0} F(Z, E_{e_1}) p_{e_1}^2 dp_{e_1} \int_0^{E_0 - E_1} F(Z, E_{e_1}) p_{e_2}^2 dp_{e_2}$$
$$\int_0^{E_0 - E_1 - E_2} p_{\nu_2}^2 dp_{\nu_2} E_{\nu_1} \sqrt{E_{\nu_1}^2 - m_{\nu_1}^2}, \tag{2.18}$$

and

$$E_{\nu_1} = E_0 - E_{e_1} - E_{e_2} - E_{\nu_2}. \tag{2.19}$$

Alternately, this equation can be rewritten as

$$\lambda = G^{2\nu}(Z, E_0)|M_F^{2\nu} - M_G^{2\nu}T|^2, \tag{2.20}$$

and $G^{2\nu}(Z, E_0)$ contains all integrations over phase space and relevant constants. Refer back to Table 1.2 for values of $G^{2\nu}(Z, E_0)$.

2.3 Neutrinoless Double-Beta Decay Rate

As detailed in Section 1.2.1, neutrinoless double-beta decay will only proceed if lepton number conservation is violated and if the emitted neutrinos have a common helicity component. As discussed, a Majorana neutrino will fulfill the first condition. The helicity condition can be fulfilled by either a non-vanishing neutrino mass or a right-handed admixture to the weak interaction.

Start with Fermi's Golden Rule as seen in Equation 2.1. The lepton part of the amplitude can be written as

$$\bar{e}(x)\gamma_\rho \frac{(1-\gamma_5)}{2}\nu_j(x)\bar{e}(y)\gamma_\sigma \frac{(1-\gamma_5)}{2}\nu_k(y) \tag{2.21}$$

Here, γ_ρ, γ_σ and γ_5 represent the Dirac matrices, ν_j and ν_k are neutrino mass eigenstates j and k with vertices x and y, e represents the electron field, and there is a contraction over the fields which is only allowed if the neutrinos are Majorana particles.

Next, the neutrino propagator is substituted and integration over the virtual neutrino momentum q is performed. The lepton part of the amplitude now looks like

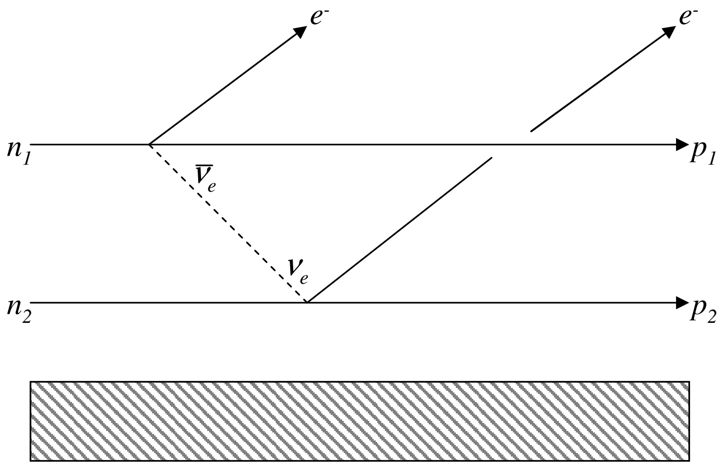

FIGURE 2.2: Diagram for $0\nu\beta\beta$ decay in the two-nucleon mechanism, where the cross-hatched bar represents the spectator nucleons in the nucleus.

$$-i\delta_{jk}\int\frac{d^4q}{(2\pi)^4}\frac{e^{-iq(x-y)}}{q^2-m_j^2}\bar{e}(x)\gamma_\rho\frac{(1-\gamma_5)}{2}(q^\mu\gamma_\mu+m_j)\frac{(1-\gamma_5)}{2}\gamma_\sigma e^C(y). \tag{2.22}$$

Now, the relations stated in Equations 2.23 and 2.24 can be utilized to reduce Equation 2.22 to Equation 2.25,

$$\frac{(1-\gamma_5)}{2}\gamma_\mu\frac{(1-\gamma_5)}{2}=0, \tag{2.23}$$

$$\frac{(1-\gamma_5)}{2}\frac{(1-\gamma_5)}{2}=\frac{(1-\gamma_5)}{2}, \tag{2.24}$$

$$-i\delta_{jk}\int\frac{d^4q}{(2\pi)^4}\frac{e^{-iq(x-y)}}{q^2-m_j^2}\bar{e}(x)m_j\gamma_\rho\frac{(1-\gamma_5)}{2}\gamma_\sigma e^C(y). \tag{2.25}$$

Equation 2.25 demonstrates that the amplitude is proportional to the neutrino Majorana mass m_j. Integrating out the virtual neutrino energy leads to a path integral whose solution is to replace the propagator $(q^2 - m_j^2)^{-1}$ with the residue π/ω_j where $\omega_j = (\overrightarrow{q}^2 + m_j^2)^{1/2}$. The remaining integration over $d\overrightarrow{q}$ gives an expression which shows the effect of the neutrino propagation between the two nucleons (see Equation 2.26). This "neutrino potential," $H(r, E_n)$, introduces a dependence on the distance between the two nucleons, r, and a weak dependence on the energy of the excited intermediate state, $(E_n - E_i)$, to the transition operator (E_e in Equation 2.26 is the energy of the electron released in the first decay).

$$H(r, E_n) = \int \frac{d^3q}{2\pi^2} \frac{e^{-i\overrightarrow{q}\cdot\overrightarrow{r}}}{\omega(\omega + E_n - E_i + E_e)}. \tag{2.26}$$

The nuclear matrix elements can then be written

$$M_F^{0\nu} =< 0_f^+ | \sum_{j=1}^{A} \sum_{k=1}^{A} \tau_j^+ \tau_k^+ H(r, E_n) | 0_i^+ >, \tag{2.27}$$

$$M_{GT}^{0\nu} =< 0_f^+ | \sum_{j=1}^{A} \sum_{k=1}^{A} \overrightarrow{\sigma}_j \cdot \overrightarrow{\sigma}_k \tau_j^+ \tau_k^+ H(r, E_n) | 0_i^+ > . \tag{2.28}$$

A good approximation of the neutrino potential is to adopt a Yukawa form as seen in Equation 2.29.

$$H(r, E_n) \simeq \frac{e^{-m_j r}}{r}. \tag{2.29}$$

Note that $m_j r$ is very small, on the order of or smaller than 10^{-8}, so the potential is basically $(r)^{-1}$. The expansion of $(r)^{-1}$ contains all orders of spherical harmonics. Thus, unlike $2\nu\beta\beta$ decay, all values of ΔJ are allowed and the Fermi matrix elements are no longer suppressed.

The phase-space calculation is very similar to that of single-beta decay, given that the only two outgoing particles are electrons. Refer back to Equation 2.9, and integrate over the energy delta function in Equation 2.13 utilizing $E_{e_2}^2 = m_e^2 + p_{e_2}^2$. The result is

$$n_{e_2} = \frac{V}{2\pi^2\hbar^3} F(Z, E_0 - E_{e_1})(E_0 - E_{e_1})[(E_0 - E_{e_1})^2 - m_e^2]^{1/2}. \tag{2.30}$$

Inserting Equation 2.30 into the full density of final states, another Fermi integral is obtained,

$$f^{0\nu\beta\beta}(Z, E_0) = \int F(Z, E_{e_1})F(Z, E_0 - E_{e_1})p_{e_1}^2(E_0 - E_{e_1})[(E_0 - E_{e_1})^2 - m_e^2]^{1/2} dp_{e_1}. \tag{2.31}$$

At last the decay rate λ can be written as

$$\lambda = \frac{G_V^4}{\pi^4}|M_F^{0\nu} - M_{GT}^{0\nu}|^2 f^{0\nu\beta\beta}(Z, E_0)m_j^2, \tag{2.32}$$

or, more frequently as

$$\lambda = G^{0\nu}(Z, E_0)|M_F^{0\nu} - M_{GT}^{0\nu}|^2 m_j^2. \tag{2.33}$$

where now $G^{0\nu}(Z, E_0)$ contains all relevant constants and the lepton phase-space integrals. Again, refer back to Table 1.2 for values of $G^{0\nu}(Z, E_0)$.

2.3.1 Phase-Space Factors

For performing the phase-space integrals analytically, the Primakoff-Rosen approximation is often used [8]. For this approximation, a simplified relativistic Coulomb expression is used for $F(Z, E)$,

$$F(Z,E) = \frac{E}{p}\frac{2\pi Z\alpha}{1-e^{-2\pi Z\alpha}}. \tag{2.34}$$

The Primakoff-Rosen approximation does a good job at approximating the electron-energy spectrum, but is not a reliable calculation of the overall decay rate. However, it is still useful in considering the differences in $2\nu\beta\beta$ and $0\nu\beta\beta$ decay phase spaces. For $2\nu\beta\beta$ decay, the approximation reveals a decay rate proportional to Q^{11}, while for $0\nu\beta\beta$ decay, the rate is proportional to Q^5. Keep in mind also that in the $2\nu\beta\beta$ mode, there are four outgoing particles in the final state, while $0\nu\beta\beta$ decay has only two particles in the final state. This, in addition to the large average momentum of the virtual neutrino actually makes the $0\nu\beta\beta$ mode of decay about 10^5 faster than the $2\nu\beta\beta$ mode, if $< m_\nu >$ were on the order of the electron mass [8]!

2.4 Nuclear Matrix Elements

The accuracy to which the neutrino mass can be determined from the $0\nu\beta\beta$-decay rate is related to how well the nuclear matrix elements (NME) are known. There are two main approaches to evaluate the NME, the quasi-random phase approximation (QRPA), and the nuclear shell model (NSM). To complicate matters further, ^{150}Nd and ^{150}Sm are strongly deformed nuclei. This condition hinders the theoretical predictions of the NME, making experimental $2\nu\beta\beta$-decay data very important.

For $2\nu\beta\beta$ decay, the Gamow-Teller nuclear matrix elements dominate the decay rate. The intermediate states are then 1^+ virtual states of the intermediate nucleus. Referring back to Equation 2.15, the first factor in the numerator describes the (n,p) amplitude for the final nucleus, called the β^+ amplitude. Similarly, the second factor represents the (p,n), or β^- amplitude for the initial nucleus. In principle, to calculate the decay rate for $2\nu\beta\beta$ decay, all Gamow-Teller amplitudes for β^+ and β^- processes must be known. However, in practice, it has been seen that a sum over only a few low-lying states is enough to determine the matrix element for some nuclei.

For $0\nu\beta\beta$ decay, there are a few distinct differences from $2\nu\beta\beta$ decay NME. Because of the radial dependence of the operators, all virtual intermediate states contribute instead of just the 1^+ states. The rapid convergence when summing over intermediate states seen in $2\nu\beta\beta$ decay does not occur in $0\nu\beta\beta$ decay; all possible states contribute comparatively. Also, the isospin selection rule which previously resulted in the Gamow-Teller matrix elements governing the decay rate no longer applies, so the Fermi matrix elements are also included.

2.4.1 NME Evaluation Methods

The neutron-proton QRPA was first used in 1967 as a tool for calculating energies and excitation strengths for collective states. For double-beta decay calculations, approximations are made even before the QRPA is applied. A diagonalized one-body potential is added to the Hamiltonian. This potential provides a single-particle basis to handle the two-body Hamiltonian determined by nucleon scattering data. This potential would later be subtracted off in a complete calculation, but in most nuclear-structure calculations, it is retained and truncated. The energy of the QRPA-calculated double-beta decay states usually extends about 10 to 20 MeV above the Fermi surface, and the one-body potential is adjusted to reproduce properties of states with one nucleon outside a closed shell [25].

The two-body interaction is also approximated before QRPA is applied. An effective Hamiltonian is constructed which has the same eigenvalues and matrix elements for low-lying states in the truncated single-particle state as would the full Hamiltonian. Then, data are used to scale certain components of the interaction. For example, all 0^+ matrix elements are multiplied by a factor of 1.1 to reproduce experimental odd-A–even-A mass differences, and short-range correlations which are involved in converting the bare Hamiltonian to the effective one are also taken care of.

The application of QRPA to double-beta decay required the addition of a particle-particle residual interaction as well as the particle-hole interaction already present. The particle-hole interaction is attractive, and its strength is determined by adjusting the calculated positions of the Gamow-Teller giant resonances to experimental values. The particle-particle interaction is a repulsive one. The parameter which represents this interaction is typically referred to as g_{pp}, which takes values between 0.8 and 1.2. Its strength is typically set by the two neutrino double-beta decay half lives (for calculation of $0\nu\beta\beta$ nuclear matrix elements) or by β^+ rates.

However, there are critiques of QRPA. One of them is the sensitivity of the decay rate to g_{pp}, which undermines the reliability of the predictions made by the model. Secondly, adjusting the value of g_{pp} for satisfactory reproduction of the $2\nu\beta\beta$ or β^+ decay rates results in QRPA solutions which are close to their critical value, indicating a rearrangement of the ground state of the nucleus. QRPA is not fully applicable when its solutions are that close to "collapse"; its purpose is to describe small deviations to the ground state.

Thus, two questions remain to improve QRPA calculations. One, how can this over-sensitivity to the g_{pp} parameter be rectified? Two, which observables should fix the value of g_{pp}? Variations of QRPA are attempting to resolve the first question, and while none of them are clearly more superior than the others, if g_{pp} is adjusted via $2\nu\beta\beta$ decay, they all give results within about 30%. It is also difficult to resolve the second question. When single-beta decay data are used to fix g_{pp}, the nuclear matrix elements for $0\nu\beta\beta$ decay are different from those when $2\nu\beta\beta$ decay is used. This results from QRPA not being able to reproduce $0\nu\beta\beta$ decay and $2\nu\beta\beta$ decay at the same time. There is also debate about the importance of the dependence on the inclusion of short-range correlations, which affect $0\nu\beta\beta$, but not $2\nu\beta\beta$. Until theorists resolve these issues, QRPA cannot predict the nuclear matrix elements to better than a factor of 2 [25].

Finally, QRPA calculations have typically treated all nuclei as spherically symmetric. Besides ^{150}Nd, other, rather important double-beta decay nuclei such as ^{76}Ge are known to be non-spherical. Work on this problem involving the use of a "deformed QRPA" has been instigated for $2\nu\beta\beta$ decay, but $0\nu\beta\beta$ decay studies using these methods are still forthcoming. Another development in QRPA research is the inclusion of the continuum, or treating all nucleons so that there is no inert core. There are also versions of this which include deformed nuclei. However, in double-beta decay calculations, these new methods would still be very sensitive to g_{pp}.

Recently, there has been one group which has computed matrix elements for $2\nu\beta\beta$ decay for deformed nuclei ^{76}Ge, and ^{150}Nd using QRPA with a deformed potential [47]. They found that not only were the results very sensitive to g_{pp}, but that the inclusion of the deformation has a large effect on both the nuclear matrix elements and their dependence on g_{pp}. Thus it is very necessary for this to be explored further and perhaps an excited-state with deformation calculation should be completed.

The nuclear shell model is another valuable tool for calculating the double-beta decay nuclear matrix elements. The NSM was introduced in the 1950's to explain the nuclear properties attributed to magic numbers. In this model, the two-body nucleon-nucleon interaction is modeled by a mean field, which is represented as a harmonic oscillator potential summed with a spin-orbit force. The exact solution is approximated by choosing a valence space (consisting of an inert core and active shells) and writing an effective interaction within that valence space. The advantage to this treatment is that for a large domain of nuclei, a number of properties such as energies of low-lying states can be described. However, for some nuclei, the valence spaces which are usable in the NSM are too small to effectively describe the desired properties [10]. From another angle, because the valence space is small, it can contain as many correlations as needed, whereas in QRPA, the necessary correlations are often not included because the computation becomes too complex.

As in QRPA, the energies of single-particle states are matched to spectra of nuclei with one nucleon outside a closed shell. An effective interaction is constructed, and the transition operator is again modified for short-range correlations, as in QRPA. In the nuclei which are of interest for double-beta decay, the Hamiltonian matrices can be $10^9 \times 10^9$ or indeed larger. For heavily deformed nuclei, such as ^{150}Nd or ^{238}U, the required bases are too large for the shell model to give accurate results, though truncated shell-model calculations have been completed [9]. Work which seems to have yielded a more realistic representation of the NME has been completed for nuclei such as ^{48}Ca, ^{76}Ge, ^{82}Se, ^{136}Xe, ^{116}Cd, ^{128}Te, and ^{130}Te.

Compared to QRPA, large-scale NSM calculations tend to produce slightly smaller results for the NME by factors as large as 2 or 3. Some of the uncertainties, specifically the effect of the short-range correlations, are similar to those in QRPA. Others, such as the truncation and determination of the effective Hamiltonian, are specific to NSM. Besides simply going to larger spaces, which in fact becomes more possible every day due to new methods of factorization and larger, better computers, the next step in improving the NSM could be a better understanding of the effective decay operator in the shell-model space [25].

In the case of ^{150}Nd, there have been several attempts in both QRPA and its extensions and NSM to calculate the NME to the ground state. However, calculations to the 0_1^+ are harder to find. In QRPA, the dependence on g_{pp} is less sensitive when the final state is excited. In such a circumstance, the calculated NME are somewhat more reliable, and comparatively easier to calculate, in general [44]. One such calculation in the truncated NSM framework gives an experimental half-life calculation of $T_{1/2} = 8.6 \times 10^{21}$ years with a nuclear deformation $\beta = 0.19$. Current experimental results in both this work, and [6] give an answer which is a full order of magnitude below this calculation. The same procedure was used to calculate the transition to the ground state, recently measured by [17] as $T_{1/2} = 9.11^{+0.25}_{-0.22} \pm 0.63 \times 10^{18}$ years. This calculation gave a half life of $T_{1/2} = 6.0 \times 10^{18}$ years.

While QRPA and NSM are the two main tools being used to evaluate NME, there exist other methods. While less popular, other and more recent methods can be a valuable check to these calculations. One such method, the microscopic interacting boson model [7] starts with different assumptions than QRPA, deals with nuclear deformation in a different way, and yet reproduces QRPA results quite well. Another method, called the microscopic anharmonic vibrator approach (MAVA) has computed the NME to excited final states for ^{100}Mo as well as to the ground state [32]. Their computed NME nicely reproduces the half-life measurement to the excited final state of ^{100}Ru made by the TUNL-ITEP double-beta decay apparatus as seen in [23] and [28]. It would be very interesting to see what their treatment of ^{150}Nd would provide.

3

Experimental Methods and the TUNL-ITEP Double-Beta Decay Setup

3.1 Previous Measurements

Detection of double-beta decay is a challenge which requires several experimental conditions. First, background must be reduced. This particular challenge has resulted in the evolution of experimental procedures to accomplish very low background rates. Another condition is the acquisition of double-beta decay source material, often enriched. Most double-beta decay nuclei are less than 10% naturally abundant, and can be expensive to acquire. Maximizing the chance of observing the double-beta decay is another vital condition.

Historically, the geochemical method was used to first confirm the existence of double-beta decay. Ancient minerals containing the parent nucleus were inspected for the accumulation of daughter products from double-beta decay interactions. This does not determine the mode of double-beta decay, but can be used to set limits on the total decay rate. A similar radiochemical procedure is employed when the daughter nucleus is radioactive. These methods are indirect methods of detection with no information about the accompanying particles in the decay or the energy information. They therefore cannot distinguish between 2ν and 0ν modes of decay [12].

Later methods incorporated direct detection of the outgoing electron energies released in the decay. Because of the long half-life, this detection requires very low background, or other information, such as tracking of the electrons. Direct detection methods can be further subdivided into active- and passive-sources. Active-source experiments are those in which the double-beta decay nucleus is also the detector, and passive-source experiments, in which the detector and source are separated. Active-source experiments, such as Majorana, GERDA, and CUORE, are extremely promising for measuring $0\nu\beta\beta$ decay because of the higher detection efficiency and large source strength. For measuring $2\nu\beta\beta$ decay, however, passive-source experiments are sufficient.

To detect the double-beta decay to the ground state, the outgoing electron energies must be observed. The measured sum-energy spectrum of the electrons can then distinguish between 2ν and 0ν modes of decay. The first of these experiments searching for the $2\nu\beta\beta$ decay of ^{150}Nd was performed underground at Baskan Neutrino Observatory at a depth equivalent to an overburden of 660 meters water equivalent (m.w.e.). An amount of $\mathrm{Nd_2O_3}$ enriched to contain 50.5 g of ^{150}Nd was sandwiched between plastic scintillators for 2000 h. These scintillators were positioned to detect the sum-energy electron spectrum for double-beta decays to the ground state of ^{150}Sm, and measured a half-life limit of $\mathrm{T}_{1/2} \geq 1.8 \times 10^{19}$ y [30].

Several subsequent measurements used a time-projection chamber to collect the two electrons. They found a $2\nu\beta\beta$ decay half life of $\mathrm{T}_{1/2} = [1.88^{+0.66}_{-0.39}(stat.) \pm 0.19(syst.)] \times 10^{19}$ [2] and $\mathrm{T}_{1/2} = [6.75^{+0.37}_{-0.42}(stat.) \pm 0.68(syst.)] \times 10^{18}$ [43]. According to [3], the appropriate average value to be used for the decay of ^{150}Nd to the ground state is $\mathrm{T}_{1/2} = (7.8 \pm 0.7) \times 10^{18}$ years. Since then, NEMO-3, a gaseous

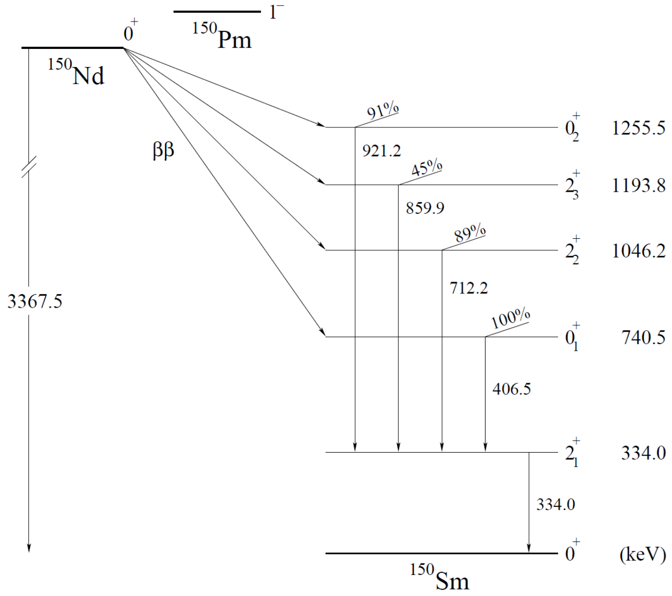

FIGURE 3.1: Level scheme of ^{150}Nd double-beta decay to higher excited states of ^{150}Sm.

tracking detector has published a value of $T_{1/2} = (9.11^{+0.25}_{-0.22}(stat) \pm 0.63(syst)) \times 10^{18}$ years [17].

Very recently though, the $2\nu\beta\beta$ decay half life to the excited 0_1^+ state of ^{150}Sm has been measured by Barabash *et al.* [6] to be $T_{1/2} = (1.33^{+0.36}_{-0.23}(stat)^{+0.27}_{-0.13}(syst)) \times 10^{20}$ y. Only limits have been established for $2\nu\beta\beta$ decay to other excited final states. (see Figure 3.1 and Table 3.1) Previously, only limits had been established for the decay to the 0_1^+ state of ^{150}Sm [29],[15],[13],[14]. These results in [6] were obtained using a single high-purity germanium (HPGe) detector whose endcap was surrounded by 3046 g of natural Nd_2O_3, which has a natural abundance of 5.64% ^{150}Nd. The total exposure was 1732 kg-h. These data do not take advantage of the coincidence technique used in the present thesis and so has significantly higher background in the regions of interest. Furthermore, Barabash *et al.* must take into account the

Final State in ^{150}Sm	γ-ray Energy (keV)	$(T_{1/2}^{0\nu+2\nu})_{exp}$ (y) previous works
$0_{g.s.}$	0.0	$(9.11^{+0.25}_{-0.22}(stat) \pm 0.63(syst)) \times 10^{18}$[17]
2_1^+	333.97	$> 2.2 \times 10^{20}$[6]
0_1^+	333.97, 406.5	$(1.33^{+0.36}_{-0.23}(stat)^{+0.27}_{-0.13}(syst)) \times 10^{20}$[6]
2_2^+	712.21, 333.97	$> 8.0 \times 10^{20}$[6]
2_3^+	1193.83	$> 5.4 \times 10^{20}$[6]
0_2^+	921.2, 333.97	$> 4.7 \times 10^{20}$[6]

Table 3.1: Previous values for ^{150}Nd $2\nu\beta\beta$ half lives as measured by NEMO and Barabash *et al.* [6]

Isotope	Intensity (%)	Energy (keV)	Decay Chain
^{214}Bi	0.065	333.37	^{238}U
^{214}Bi	0.036	334.78	^{238}U
^{214}Bi	0.169	405.72	^{238}U
^{228}Ac	0.40	332.37	^{232}Th
^{227}Th	1.54	334.37	^{238}U
^{211}Pb	3.78	404.853	^{238}U

Table 3.2: The most likely candidates for contamination in the regions of interest for ^{150}Nd.

numerous γ-ray lines which contaminate the regions of interest which are listed in Table 3.2. None of these γ rays have coincident partners in the regions of interest and are therefore not likely to enter our spectra.

3.2 Experimental Method

The TUNL-ITEP double-beta decay setup consists of two HPGe detectors surrounded by several layers of active and passive shielding. These detectors operate in coincidence in order to detect de-excitation γ rays from an excited final state of a nucleus which has undergone double-beta decay. The implementation of the coincidence technique here has two results. First, requiring two distinct gamma-ray energies simultaneously immediately reduces the occurrence of background events significantly. Second, although the efficiency for detecting these two gamma rays is reduced compared to single-gamma detection, the uniqueness of the signal means a generally unambiguous result.

Sodium iodide (NaI) detectors and germanium semiconductor detectors are the most commonly used gamma-ray detectors. Due to their large size, NaI detectors can have a very high detection efficiency, but they suffer from poor energy resolution. Germanium detectors have vastly superior energy resolution, but have a much lower detection efficiency. The coincidence technique is often used for detection purposes in many different configurations. Perhaps the most common purpose is to utilize a coincidence between detectors as a veto, as in the TUNL-ITEP setup. Another common use of the coincidence technique is found in positron emission tomography (PET), where a positron-emitting radionuclide is introduced into the subject of the scan. The imager detects coincidences between the resulting 511 keV gamma rays. Using this information, a three-dimensional image of the tracer concentration can be reconstructed by a computer.

Some past experiments have used the coincidence technique for double-beta decay detection. Often, these experiments used either two NaI detectors or multiple NaI detectors and one germanium detector in coincidence. For example, in [46], two NaI detectors and two proportional counters were utilized in an experiment to detect the $2\nu\beta\beta$ decay of ^{96}Zr to excited final states of ^{96}Mo. The NaI detectors were operated in coincidence to detect the gamma rays from the excited states decay, while the proportional counters detected the electrons emitted from the sample. In [37], the neutrinoless double-beta decay of ^{76}Ge was studied to the first excited state of ^{76}Se. One germanium detector, which served as the source material as well as recorded the emission of the electrons, was placed in the middle of an annulus of NaI detectors, which detected the de-excitation gamma ray. Though these experiments were unsuccessful, they were instrumental in the important science of background reduction.

Because of the comparatively low detection efficiency of germanium detectors, it was considered impractical to use two such detectors in a coincidence scheme. Coincidence detection efficiency behaves roughly as the products of the two individual efficiencies, and so it was assumed that the combined efficiency would be too low to observe a positive result for double-beta decay. However, as the TUNL-ITEP setup operated at TUNL was the first to demonstrate in [23], that is not the case. The double-beta decay of ^{100}Mo to the 0_1^+ excited final state of ^{100}Ru was detected via the coincident gamma rays. One unsuccessful attempt was made by [29] using four germanium detectors in coincidence in the search for the double-beta decay of ^{150}Nd and ^{76}Ge to excited final states.

3.2.1 High-Purity Germanium Detectors

Germanium detectors were chosen for the TUNL-ITEP double-beta decay setup for several reasons. Though they have low efficiency compared to many other types of detectors, their superior energy resolution makes up for it. Germanium crystals are by nature of very high purity, having less than one part in 10^{12} impurity concentrations [20]. Also, there are no primordial radioactive isotopes of germanium with a natural abundance. However, background peaks due to the germanium can occur from activation and excitation from cosmic-ray interactions. This background will be further discussed in 4.3.3. Finally, other materials used in the manufacturing of the detectors can contain small amounts of contaminants. Since the TUNL-ITEP double-beta decay setup relies on low backgrounds, all contamination must be well-understood.

The manufacturing of the crystal begins with electronics-grade germanium, which is already very pure. It is then further purified via a process known as zone refining, which can reduce impurities by as much as a factor of 100. Once purified, the germanium is melted into a crucible and a cylindrical crystal is ”pulled” via the insertion and slow removal of a seed crystal. Finally, the crystal is cut and ground. If the detector is coaxial, a hole is machined into one end for a central contact, and the edge of the other end is typically rounded off, or bulletized. Depending on the net amount of impurities, the crystal is p-type (there are more acceptor impurities) or n-type (there are more donor impurities). For p-type coaxial germanium detectors such as the ones in the TUNL-ITEP double-beta decay setup, a layer of lithium about 600 μm thick is diffused over the outer surface where an electrical n-type contact is made. A layer of boron less than 0.3 μm thick is ion-implanted in the central hole, where the other electrical p-type contact is made [20].

A high voltage reverse-bias is applied across these electrical contacts. It is called a reverse-bias because a positive voltage is connected to the n-type contact, while a negative voltage is connected to the p-type contact. The result of this bias is to enhance the depletion region formed at the p-n junction of the germanium and lithium; the excess electrons are attracted to the positive voltage and the excess holes are attracted to the negative voltage. When ionizing radiation interacts with the depletion region, resulting electron-hole pairs are swept to their respective contacts, which creates an electrical signal. The excellent energy resolution of germanium detectors can be understood by considering the energy required to create an electron-hole pair in the crystal, which is only 2.96 eV. Such a small energy means a great number of pairs are created per interaction, and the number created is in proportion to the total energy of the interaction.

Because of the ease of promoting an electron to the conduction band in germanium, at room temperature, thermal fluctuations result in a leakage current. Therefore, germanium crystals must be cooled to reduce the thermal fluctuations. This is accomplished by keeping the detector in a cryostat with a copper cold finger in thermal contact with liquid nitrogen (LN) at 77 K. As a safety precaution, the pream-

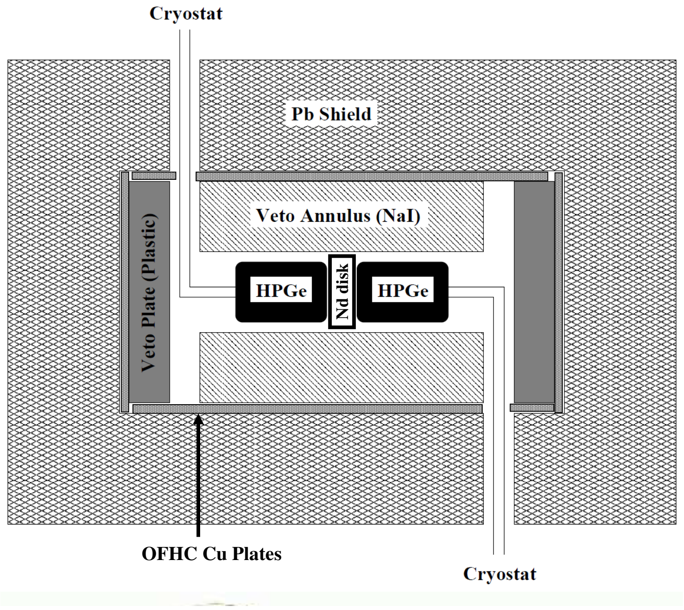

FIGURE 3.2: Diagram of the TUNL-ITEP double-beta decay setup detailing the surrounding lead housing, OFHC copper plates, and sodium iodide annulus for shielding. Modified from [23].

plifier has a circuit which turns off the high-voltage if the temperature of the crystal becomes too high. This prevents potential damage to the crystal.

The HPGe detectors of the TUNL-ITEP double-beta decay setup are about 8.8 cm in diameter and 5.0 cm in thickness. The endcap of each detector is nickel-plated magnesium about 2.54 mm thick at the front face. The detector assembly is connected to the cryostat in the j-type configuration. To reduce background, the preamplifier and high-voltage filter are housed away from the crystal near the LN dewar. This type of configuration also easily allows the detectors to be inserted into the veto annulus, which is further discussed in Section 3.2.5. A diagram of the setup is shown in Figure 3.2

The detectors were manufactured by EG&G Ortec using low-background components. They were delivered with performance specifications, and are each quoted as having 85.7% relative efficiency at 1.33 MeV. The FWHM energy resolution at 1.33 MeV is quoted as 1.8 keV, and at 0.122 MeV it is 0.8 keV. The standard 30-liter LN dewars require filling every week.

3.2.2 Gamma-Ray Detection

To explain how these types of detectors work, it can be beneficial to first consider how gamma rays interact with matter. Detection of any particle or radiation is dependent upon the secondary particles which are produced. These are collected by the detector to produce the electrical signal indicating the interaction. While charged particles ionize or excite detector material directly, the uncharged gamma-ray photon interacts in ways that transfer its energy to the electrons in the detector material. There are three such mechanisms which dominate gamma-ray interactions in matter: photoelectric absorption, Compton scattering, and pair production. At low energies, photoelectric interactions are dominant, Compton scattering overwhelms middle-range energies, and pair production dominates at high energies. Other, less common interactions include coherent scattering and photonuclear reactions. The former of these occurs when the gamma ray is absorbed, then re-admitted with the same energy, but a different direction. Though this might affect attenuation, no energy is imparted to the detector due to this interaction, and thus produces no signal. For photonuclear reactions, the cross sections are small enough below 5 MeV as to be insignificant [20].

Photoelectric absorption occurs when the gamma-ray photon interacts with one of the atomic orbital electrons. The electron is ejected from the atom with energy equivalent to the gamma energy minus the binding energy of the electron. The excited atom then relaxes to equilibrium by either distributing the excitation energy between the remaining atomic electrons, resulting in the release of Auger electrons, or the vacancy of the ejected electron could be filled from electrons from higher shells. This results in the emission of characteristic X rays, which may then interact via photoelectric absorption repeatedly until all the gamma-ray energy has been absorbed. Because all the gamma-ray energy is absorbed in this process, photoelectric absorption produces a full-energy peak in the energy spectrum.

Compton scattering occurs when a gamma ray interacts directly with an electron in the detector. Part of the gamma-ray energy is imparted to the electron, while the gamma ray carries the remainder of the energy away at an angle $0\leq \theta \leq \pi$. At all scattering angles, a Compton-scattered gamma never fully transfers its energy to the electron, thus the energy absorbed by the detector is less than the full energy, contributing to the background at energies lower than the full-energy peak.

Finally, pair production is the result of a gamma ray interacting with the entire atom. Within the Coulomb field of the nucleus, a gamma ray is converted into an electron-positron pair. The gamma ray must have had at least 1022 keV, equivalent to the total rest mass of the two particles, for pair production to occur. Any energy in excess of this limit is shared between the particles, and they lose the energy as they interact within the detector. Once the positron reaches near-thermal energy, it annihilates with an electron, producing two 511 keV gamma rays [20].

3.2.3 Double-Beta Decay Source

^{150}Nd is an excellent candidate for double-beta decay study for several reasons. Its high Q-value, even to excited final states, makes it a viable isotope for the TUNL-ITEP double-beta decay setup. Despite the fact that double-beta decay to the ground state has been observed in ten nuclei, ^{150}Nd is only the second isotope in which double-beta decay to an excited final state has been observed. Very little information is currently available regarding the nuclear matrix elements of ^{150}Nd. Finally, ^{150}Nd is the nuclide of choice for the next phase of the Solar Neutrino Observatory, called SNO+, which will attempt to measure $0\nu\beta\beta$ decay of ^{150}Nd. In this case, the $2\nu\beta\beta$ decay will be a large background factor and must be well-understood. Also, methods of producing the enriched ^{150}Nd result in different types of backgrounds in the source. SNO+, which is still under development, needs to have information about the contaminants in the various types of sources.

For the study of the $2\nu\beta\beta$ decay of ^{150}Nd to the 0_1^+ state of ^{150}Sm, 50.000 grams of powdered neodymium oxide (Nd_2O_3) enriched to 93.60% ^{150}Nd were leased from Oak Ridge National Laboratory. This corresponds to 42.870 g Nd metal and 40.13 g ^{150}Nd. The Nd_2O_3 is sealed in an acrylic holder with a cavity measuring 5.72 cm in diameter and 0.72 cm deep. These dimensions were chosen with the coincidence efficiency of the HPGe detectors in mind (see Section 4.2).

3.2.4 Passive Shielding

The first goal of shielding is to reduce the number of gamma rays produced outside the sample from reaching the detectors. To absorb these gamma rays, high-Z material is placed around the detector setup. The TUNL-ITEP setup has a lead house built around and beneath it. The thickness is about 6 inches (about 15 cm) on all sides. At 500 keV, relatively near our region of interest, the attenuation of 15 cm of lead is $>10^6$. A likely contaminant in lead shielding is ^{210}Pb, which has a half-life of 22.2 years.

Within the lead shield, there is a layer of 3/4 inch thick Oxygen Free High Conductivity (OFHC) copper plates. OFHC copper has a purity of 99.99%, but can still be activated via (n,α) to ^{60}Co by cosmic ray neutrons. Aside from this disadvantage, OFHC copper has low concentrations of ^{208}Tl (<0.005 Bq/kg), ^{214}Bi (<0.02-0.17 Bq/kg), and ^{40}K (<0.2 Bq/kg)[20]. Using another absorbing material such as copper inside the lead shield can reduce the gammas from the daughters of ^{210}Pb.

3.2.5 Active Shielding

Another way to reduce the background, especially the Compton continuum, is to employ active shielding. This type of shielding can discriminate when a gamma ray is scattered out of the detector leaving only part of the energy deposited, or when a gamma ray comes from outside the system. The HPGe detectors are surrounded by a sodium iodide (NaI) annulus with two plastic plate scintillators on the endcaps. The NaI(Tl) crystal is housed inside of low-background aluminum. The annulus has dimensions of 12.5 cm and 35.6 cm for the inner and outer diameters, respectively, and is 50 cm long. Six standard 3 inch diameter photomultiplier tubes (PMTs) are installed on each end of the NaI annulus, though using only three on each side provided adequate coverage. The plastic plate scintillators are 10 cm thick and 30 cm × 30 cm square. Each plastic plate has two 2 inch PMTs on opposite sides. All the PMTs are biased to 1320 V.

Because of its proximity to the HPGe detectors, the NaI annulus is particularly vital to the veto process. The plastic scintillators function to veto particles which would not be seen by the annulus, *i.e.*, they travel nearly horizontal, along the axis of the annulus. This seems unlikely for a primary particle, but secondary interactions in the shielding, or Compton scattering in the detectors could result in such a condition.

3.2.6 Kimballton Underground Research Facility

The Kimballton Underground Research Facility (KURF) is a relatively new facility located at the Kimballton mine run by Chemical Lime Company. The Kimballton mine is located in Ripplemead, Virginia about 25 miles northwest of Blacksburg, Virginia. It is an operating limestone mine with over 50 miles of drifts and a current maximum depth of 2300 feet. Our present facility is located at the 14th level at a depth of 1700 feet. This depth corresponds to about 1450 m.w.e. The mine has drive-in access, which allows for the installation of self-contained laboratory modules.

FIGURE 3.3: (Color online) On the left can be seen the laboratory area with only the concrete pad present. On the right is the completed laboratory structure containing the TUNL (left side) and NRL (right side) trailers.

Prior to Fall 2007, practically no laboratory infrastructure existed at the facility aside from a concrete pad and a connex trailer belonging to the Naval Research Laboratory (NRL). By the end of October 2007, the concrete pad had been sealed, and a laboratory structure had been constructed in which the NRL trailer was installed (see Figure 3.3). In early January 2008, the TUNL connex was transported from Duke and installed at KURF (see Figure 3.4). Finally, a 600 gallon liquid nitrogen tank was delivered to the facility. The TUNL-ITEP double-beta decay setup commenced operation at KURF in late January 2008 and is currently one of three operating experiments taking place there.

The TUNL-ITEP double-beta decay setup and its electronics are installed inside of a clean room plastic tent, which circulates air through HEPA filters. Though the space is not operated as a clean room, the plastic curtains and HEPA filtration keep the electronics and general area free from diesel particulate (generated by the mine vehicles), which is a fine, black dust. The connex trailer itself has air circulated through a heat pump with standard filters. These are changed at every visit, and help keep the office space of the connex clean. The heat pump also keeps the trailer at a constant temperature. Since the humidity in the mine approaches 100%, a dehumidifier is also employed. Because of not infrequent power fluctuations and outages, the detector electronics and data-acquisition system power is routed through an uninterruptible power supply (UPS). The UPS, once equipped with new batteries, keeps the power running for approximately five hours.

An auto-fill system for the HPGe detectors allows the setup to be truly remote. Two 240-liter LN dewars are filled by hand from the large 600 gallon tank. These are referred to as the buffer dewars, and they are each connected to the HPGe detectors via a manifold. Each buffer dewar is equipped with a solenoid valve, as are each of the outputs of the manifold. Each detector dewar is connected to an outlet of the manifold. The solenoid valves on the inside are powered by a controller. Each detector dewar is equipped with a thin aluminum rod onto which three temperature sensors are placed. One at the top signals when the dewar is full, and the lower two signal a fill condition, and an alarm condition in case the fill does not occur as expected. Once the "fill" sensor becomes warm, the controller opens the solenoid valve for a fill. The solenoids on the two outside buffer dewars are powered by an IP switch, which allows a remote user to log on and select which valve should be opened. In this way, the detectors can be filled from one buffer dewar until it is empty, and the other dewar can then be selected. In principle, this can supply the detectors with LN for six weeks.

A DSL line runs from the surface of the mine to the KURF building to provide broadband internet access to the experimental areas. From the modem, it is routed to the TUNL connex. A computer, referred to as "pluto," which runs a LINUX operating system acts as a network bridge between TUNL and KURF. The network bridge allows all the computers at KURF to be part of the TUNL local area network (LAN). In this way, users physically located at TUNL may easily start and stop runs and transfer data. Several cameras are positioned around the facility to monitor

Figure 3.4: (Color online) A view of the TUNL-ITEP double-beta decay setup from the door of the TUNL connex trailer.

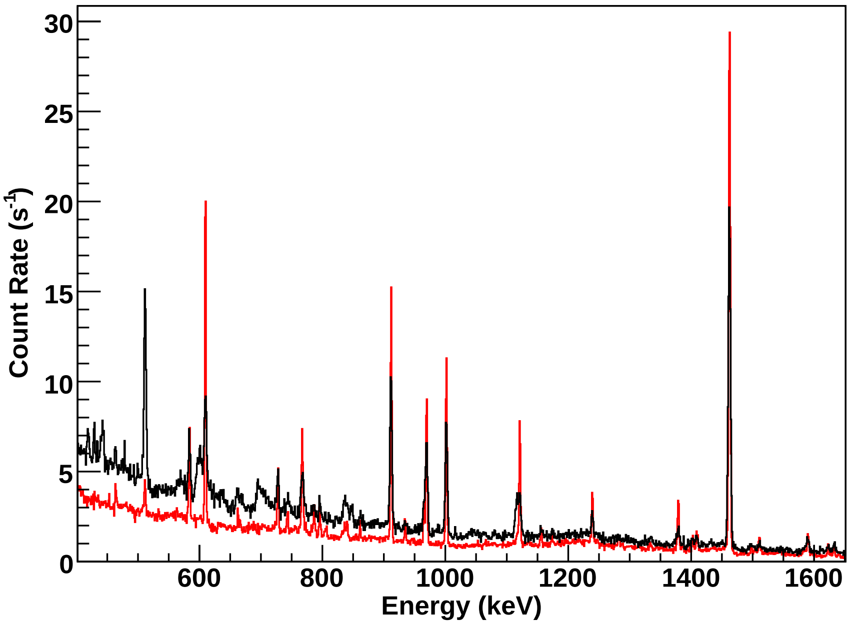

FIGURE 3.5: (Color online) Normalized data taken at ground level (black) and at KURF (red).

liquid nitrogen levels on the buffer dewars, high-voltage levels, and the fill process. Pluto uploads these pictures to an external website every 30 minutes. Finally, pluto also manages several email alerts which inform the facility users when LN fills are taking place, when the power has gone out and the setup is running on the UPS, and when the UPS fails (an additional small UPS powers the modem long enough for pluto to send this final message).

The TUNL-ITEP double-beta decay apparatus was previously operated above ground in the TUNL Low Background Counting Facility (LBCF), a shielded room in the basement of the Duke Physics Building. Due to contamination of our enriched ^{150}Nd source with ^{232}Th decay products, the background was too high in our regions of interest to extract a competitive half-life limit for this particular decay while operating at ground level [26]. The source was sent back to Oak Ridge National Laboratory for purification, causing a one-year delay in the actual measurement of

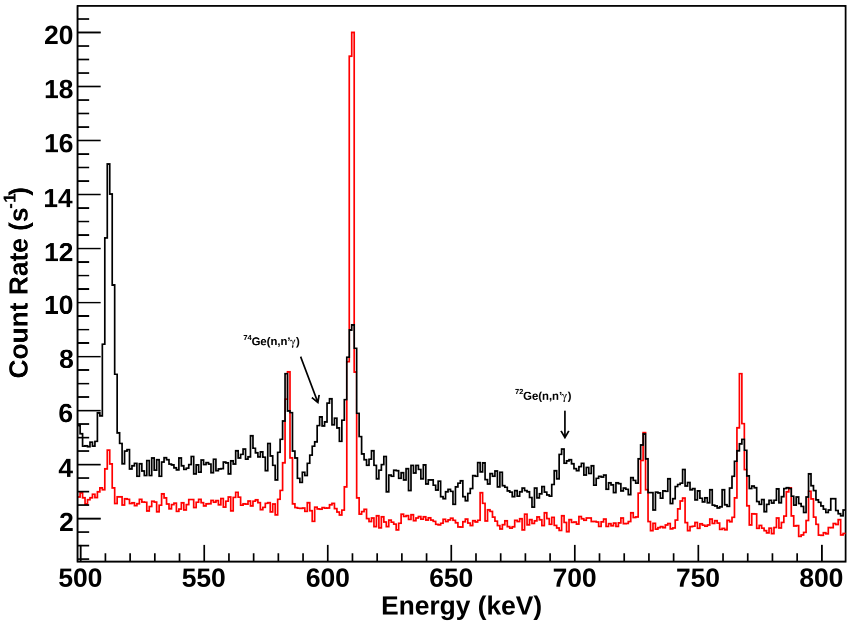

FIGURE 3.6: (Color online) A closer look at Figure 3.5. The reduction of the 511 keV γ–ray line and the asymmetric peak from neutron capture on ^{74}Ge and ^{72}Ge is evident.

^{150}Nd.

In the meantime, the apparatus was applied to investigate 0νECEC in ^{112}Sn [27]. In this case, the regions of interest are 618 keV and 1253 keV. Figure 3.5 shows normalized spectra taken at the TUNL LBCF and at KURF with an enriched ^{112}Sn sample in place. There is a strong line present at 392 keV due to the decay of ^{113}Sn ($T_{1/2}$ =115 days) which is a contaminant in the ^{112}Sn sample, resulting from prior exposure to neutron beams. Thus, the data shown in Figure 3.5 are above 400 keV. The Compton scattering from this line masks the reduction we would see at 334 keV, but the background reduction factors for each of our regions of interest above 392 keV can be seen in Table 3.3. While many of the gamma–ray lines in Figure 3.5 are intrinsic to our setup and thus not reduced by moving underground, the reduction of cosmic–ray background is apparent. The 511 keV peak is reduced by a factor of

Energy (keV)	Reduction Factor	Isotope of Interest
407	2.17	^{150}Nd
618	2.66	^{112}Sn
1253	2.42	^{112}Sn

Table 3.3: Background-reduction factors

ten, and the neutron capture by ^{74}Ge at 596 keV and ^{72}Ge at 691 keV is no longer distinct as can be seen in Figure 3.6.

3.2.7 Electronics

The electronics setup processes the signal initiated in either HPGe detector before it is accepted and processed by the data-acquisition (DAQ) system. In a coincidence setup, the timing of the electronics is very important. In a coincidence system with high count rate, a very high timing resolution must be accomplished. Since the TUNL-ITEP double-beta decay setup is designed to be a low count rate system, the time-resolution requirements are relaxed.

There are two main sections to the electronics setup; one is for the purpose of the coincidence measurement between the two HPGe detectors and the other is an anti-coincidence between each HPGe detector and the NaI annulus plus plastic scintillator shields. The electronics components which process the signal up to the analog-to-digital converter (ADC) in the DAQ are NIM standard. The NIM modules are linked by coaxial cables.

As shown in Figure 3.7, a signal produced in one of the HPGe detectors is first transmitted through a preamplifier and is then sent to an amplifier for shaping and amplification. There are two outputs of the amplifier module. The unipolar output is sent to the ADC via a delay amplifier set to 4.75 μs. This delay is chosen to coordinate the signal with the separate timing signal which opens the gate to the

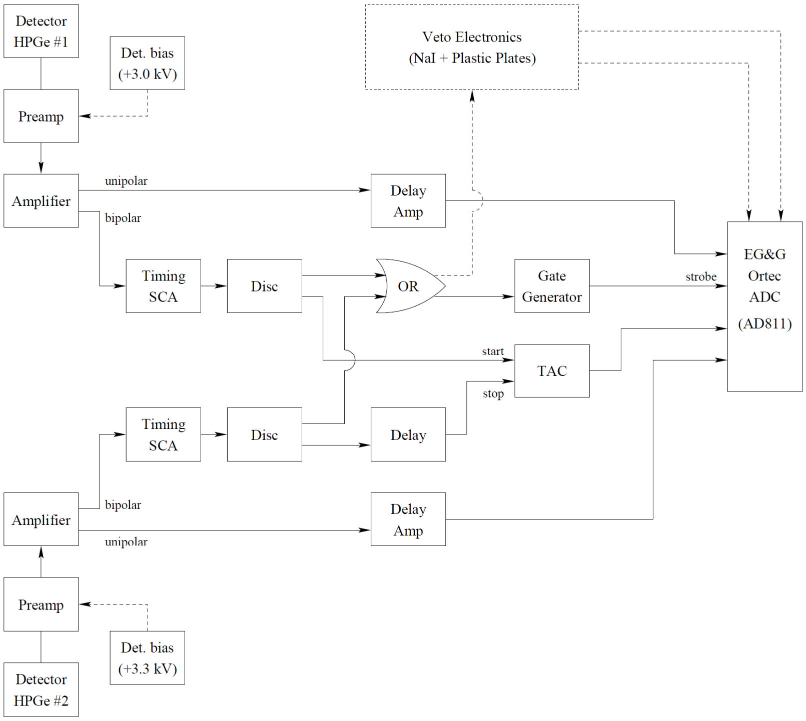

FIGURE 3.7: Diagram showing the electronics for the primary coincidence between the HPGe detectors.

ADC. The pulse height of this unipolar signal is proportional to the energy deposited in the HPGe detector.

The bipolar output of the amplifier is sent first to a timing single-channel analyzer (SCA) whose output is a logic signal which represents the arrival of the original signal. This signal is sent to a discriminator. One of the discriminator outputs is sent to start the time-to-amplitude converter (TAC). For detector 1, this signal is sent directly to the ”start” input of the TAC, but for detector 2, the corresponding signal is first directed through a delay of 1 μs before being sent to the ”stop” of the TAC. The TAC output is sent to the ADC. The other discriminator output goes to a logic module which is set to deliver a logic pulse if there is a signal in either

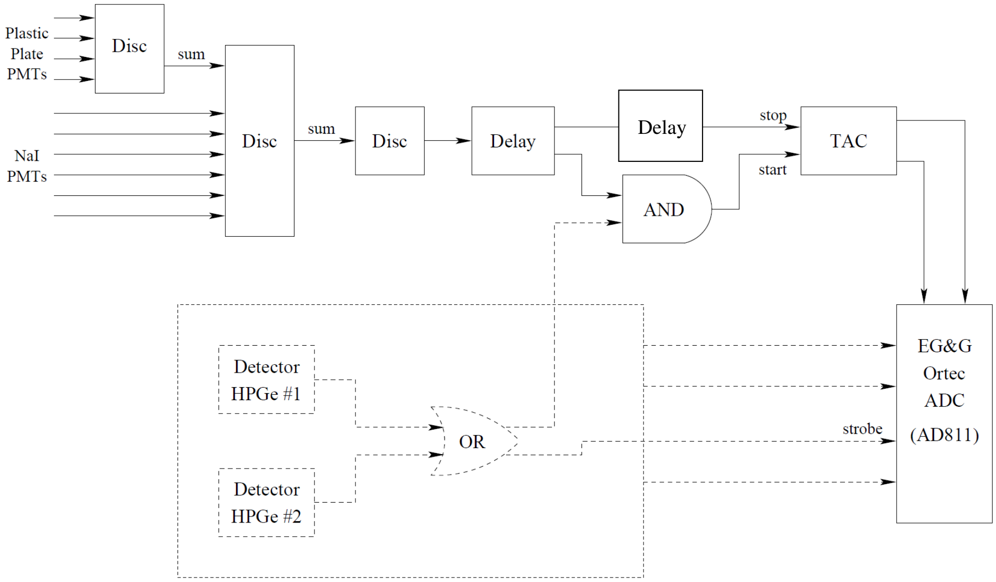

Figure 3.8: Diagram showing the electronics for the veto detectors surrounding the HPGe detectors.

HPGe detectors. One output of this OR gate triggers the ADC, and the other goes to another logic circuit which produces a logic signal if there is also a corresponding signal in the veto electronics.

The intention of this coincidence measurement is to detect a signal in coincidence with both HPGe detectors, but not in any of the veto detectors. Therefore, the energy of the signal coming from the veto detectors is not relevant; only the fact that the veto counters have fired in coincidence with either HPGe detector is important. The outputs of the PMTs which collect the scintillation light from both the NaI crystal and the plastic shields are summed, sent to a discriminator, and delayed to coincide with the signals from the HPGe detectors. This output is sent to the logic unit mentioned in the previous paragraph which performs an AND gate on the veto and HPGe signals. If there is a signal in either HPGe detector and a signal in the veto counters, an output is sent to start the veto TAC. The stop is a delayed copy of the veto signal, and the TAC output is sent to the ADC.

3.2.8 Computer Interface

After making it to the ADC, the signal must now be digitized and sent to the DAQ. The ADC used in this setup is an Ortec AD811. This module is a Computer Automated Measurement and Control (CAMAC) module in a CAMAC crate. It contains eight ADCs which can each accommodate 11 bits, or 2047 channels. Of these eight ADCs, five are utilized: one for each HPGe detector, one for the timing between the two HPGe detectors, and two for the timing between either HPGe and the veto counters.

The strobe input is supplied by the gate generator in the electronics circuit which is triggered by a signal from either HPGe detector. The strobe input begins the digitization process of any peaks found in the eight ADC channels. The AD811 takes approximately 80 μs to process an analog signal and output a digital signal, and afterwards generates a "look-at-me" (LAM) signal to the CAMAC controller. The CAMAC crate controller is a Wiener CC32. The CC32 module interfaces the CAMAC crate with the data-acquisition host computer.

The DAQ system used is the CEBAF On-line Data Acquisition (CODA) program, first developed at Jefferson Laboratory in Newport News, Virginia. Each CODA data file contains the energy deposited in each detector and the three TAC spectra. These files are converted to ROOT files for analysis via the TUNL Real-time Analysis Package (TRAP). This package is still under development. TRAP creates a ROOT tree which contains event-by-event data for each detector [1].

4

Analysis

4.1 Calibration of Gamma-ray Spectra

In a perfect low-background setup, there would be no prominent peaks and calibration could be a difficult job. However, as detailed in Section 4.3.1 it is very difficult to get rid of all background sources. In a positive light, these background peaks are extremely well-known and so provide a very reliable energy calibration.

In the TUNL-ITEP setup, there are a few contaminants that are inherent to the setup or to the sample that are used for calibration purposes. A wide range of energies were chosen to ensure a calibration valid over the entire spectrum. Peaks used were the 238.6 keV from the β-decay of ^{212}Pb in the ^{232}Th decay chain, the annihilation peak at 511.0 keV, the ^{40}K peak at 1460.8 keV, and the ^{205}Bi electron capture peak at 1764.3 keV. These peaks are labeled in Figure 4.1. A ROOT script automated the process by fitting the peaks of interest, obtaining their centroids, and creating an energy vs. channel plot. The points were fitted with the ROOT MINUIT fitting procedure to a first degree polynomial. The y-intercept and slope of the line as well as the centroids of each peak were written out to a data file, which easily allows for monitoring the stability of the detectors over a long period of time. New ROOT data files are then created which contain trees with the newly calibrated singles spectra as branches.

The effect of the NaI annulus veto can clearly be seen in Figure 4.1. The Compton continuum is reduced by about a factor of two, and several peaks which are associated with other gammas are also greatly reduced. In particular, the 511.0 keV photon is always emitted with at least one other 511.0 keV photon, and as a result, is reduced by a factor of 9.4. In contrast, many of the prominent peaks such as 1460.8 keV are not emitted with any other photon, and thus are not affected by the veto.

To determine the coincidence events, relevant windows, called TCuts, are first defined in a ROOT script. All the data files are chained together, and events are projected into the histograms if they meet the TCut conditions. The events in detector 2 are plotted versus the events in detector 1. Only the events which meet the coincidence timing requirement (about 4 μs) between the two detectors and the anti-coincidence timing requirement (about 10 μs) between the detectors and the veto are plotted in this spectrum (see Figure 4.2). A few features in this graph are the diagonal lines and the horizontal and vertical lines. The diagonal lines are the result of a photon from a strong background peak which deposits part of its energy in one detector, and the rest of it in the other one. The horizontal and vertical lines are the result of true coincidences between a strong background peak and a Compton scattered gamma-ray from a member of the associated cascade. The high-intensity spot in the upper right is a pulser which was used to determine the dead time. The use of the pulser was discontinued after a short time due to the low count rate; the dead time was always less than 0.5%.

In the two-dimensional spectrum, the events of interest would occur at (334 keV, 406.5 keV) and (406.5 keV, 334 keV). The significance of the counts in the two-dimensional regions of interest can best be seen by projecting them onto the x- or

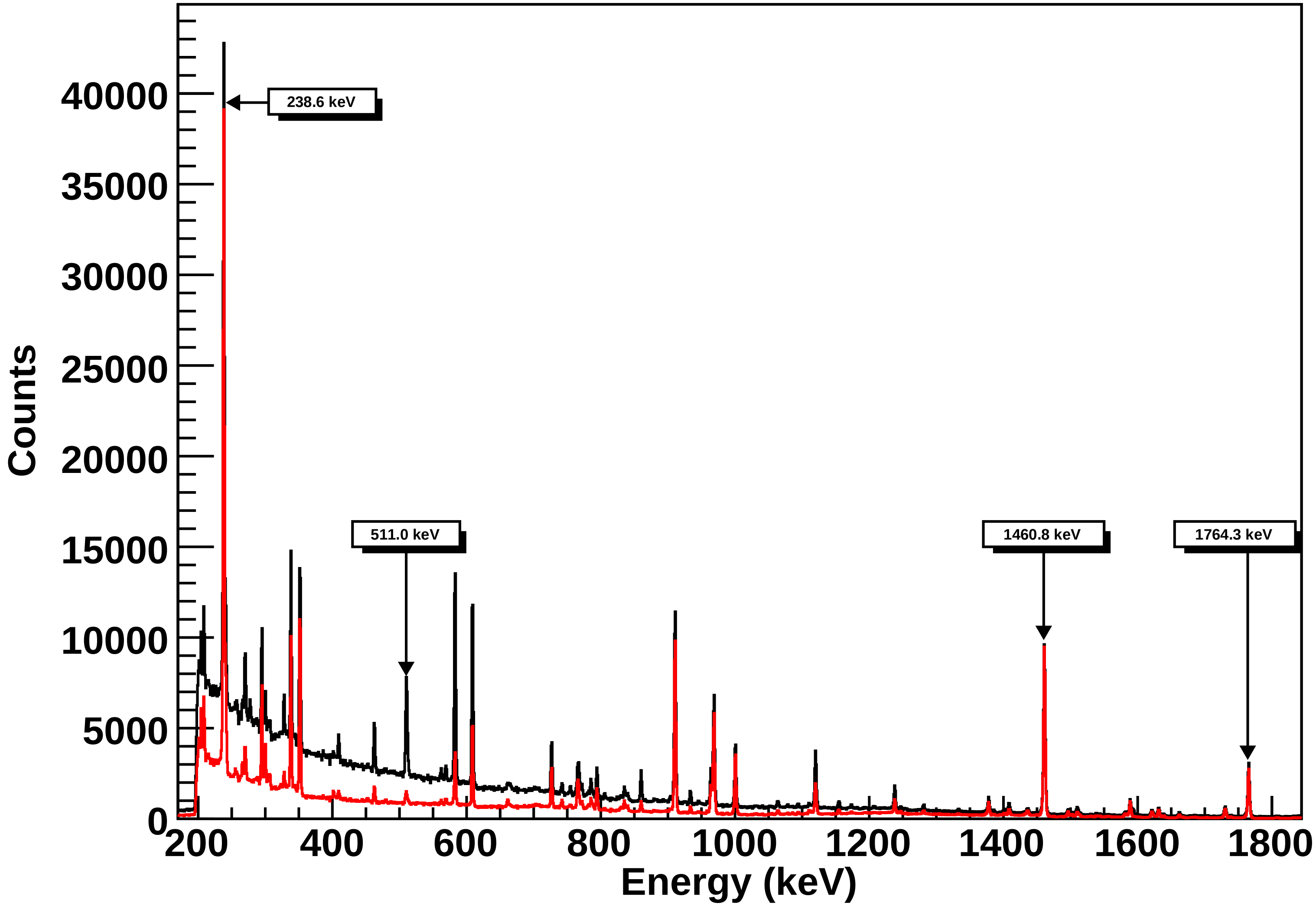

FIGURE 4.1: An example of a singles spectrum taken at KURF for about 250 days. The labeled peaks are used in calibration. The black line is before the NaI veto is applied, and the red line is after.

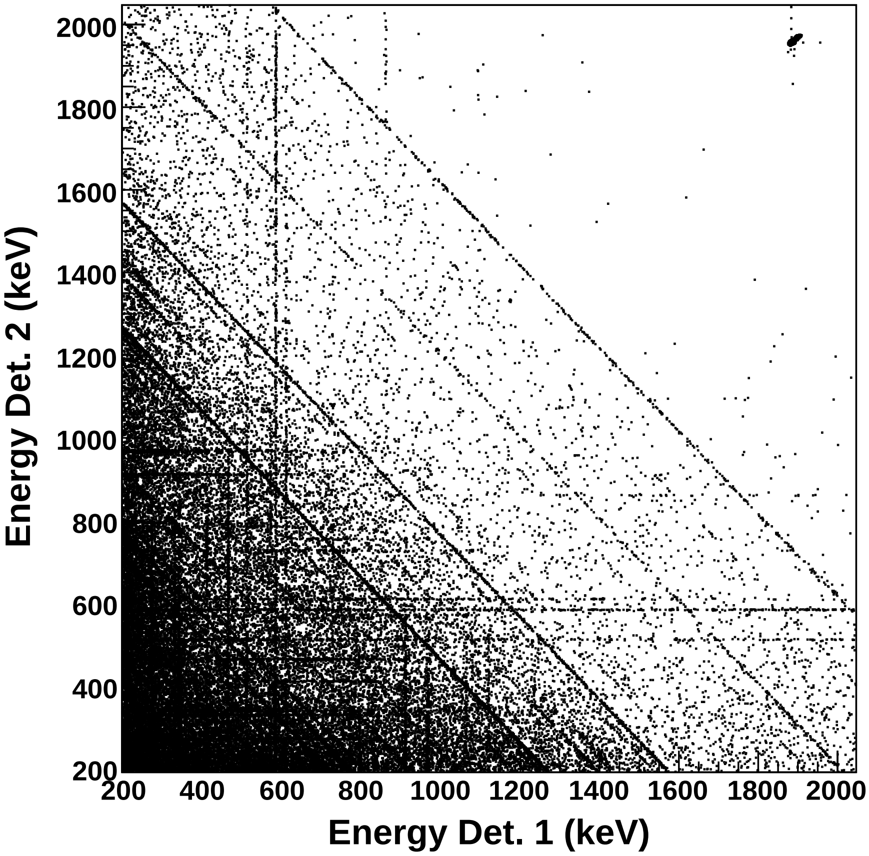

Figure 4.2: An example of a two-dimensional spectrum taken at KURF for about 250 days. Energy in detector 2 is plotted against energy in detector 1. Bins are 1 keV x 1 keV. See text for an explanation of the features of the plot.

y-axis. To accomplish this, a TCut is applied to events in one detector, and all the events which occur in the other detector in coincidence are projected into a histogram. This results in four histograms; two are in coincidence with 334 keV in detectors 1 and 2, and two are in coincidence with 406.5 keV in detectors 1 and 2. The corresponding histograms can then be summed so that all events in coincidence with a 334 keV photon are in one histogram, and vice versa, reducing the number of histograms to two (see Figure 4.3).

To evaluate the background within the regions of interest, regions in which no

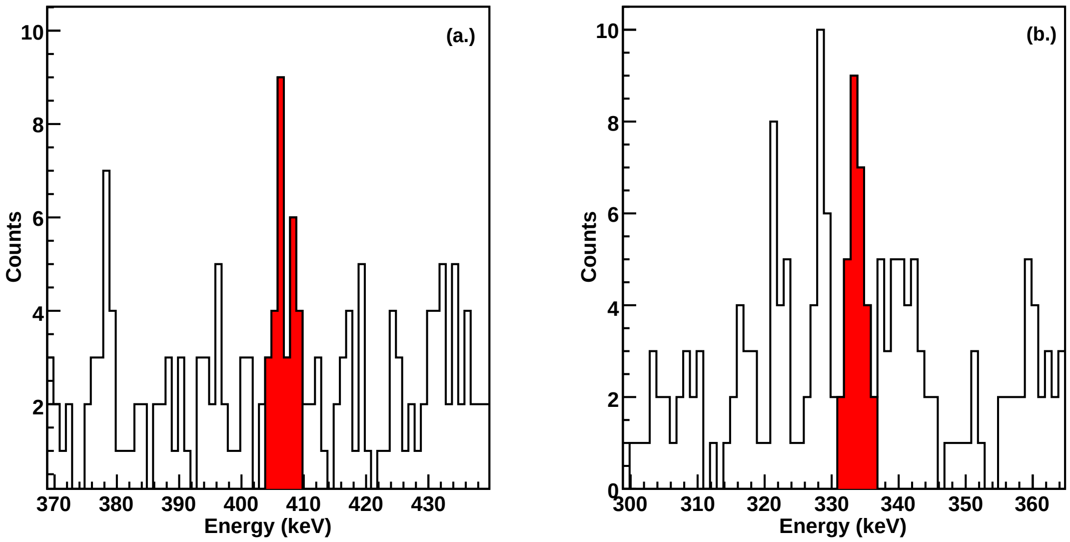

FIGURE 4.3: (Color online) Coincidence data from 391 days of run time. Spectrum (a) is in coincidence with 333.9 keV, and (b) is in coincidence with 406.5 keV. The energy coincidence cut shown is ±3.0 keV. Bins shaded in red are within the regions of interest.

apparent peaks existed were integrated and averaged over the energy range. The validity of this background average is dependent upon how well a peak-free area can be known. To this end, an effort was made to identify all significant peaks near the regions of interest. This also shows that the peak located within the region of interest is statistically significant and not surrounded by sizable background events. A quick calculation can also verify that these coincidences are not accidental. The event rate seen by each detector is about 0.25 events/s, and the coincidence timing window is 4 μs. The accidental rate can be calculated by multiplying the rate in detector 1, the rate in detector 2, and the timing window width. This calculation results in a coincidence rate of about 8 events in the entire counting time. These should be distributed evenly over the entire two-dimensional spectrum, and so, do not contribute to events within the region of interest. In fact, since some of the events counted in the event rate are true coincidental events, this is an overestimate of the coincidence event rate.

4.2 Coincidence-Efficiency Measurement

In order to properly interpret the events seen in Figure 4.3, the coincidence efficiency of the two HPGe detectors must be known. This measurement was originally completed for the initial measurement of the half life of ^{100}Mo double-beta decay to excited final states in ^{100}Ru as seen in [23]. After completing a second 450 days of counting ^{100}Mo, a second efficiency measurement was done with more data points to further reduce the systematic error in the half-life measurement. This efficiency measurement and its application to the ^{150}Nd half-life determination is discussed below.

The radioactive source used to measure the efficiency was ^{102}Rh, which was produced at TUNL via the reaction ^{102}Ru(p,n)^{102}Rh initiated with 5 MeV incident protons on a natural ruthenium target (31.6% ^{102}Ru). This particular source was chosen for several reasons. First, the $0^+_1 \rightarrow 2^+_1 \rightarrow 0^+_{gs}$ decay sequence not only results in γ rays in coincidence, but also mimics the decay scheme of the excited final 0^+_1 state of ^{100}Ru. Therefore, corrections for the angular distribution are unnecessary. The associated γ ray–energies, 468.6 keV and 475.1 keV, are also close to those of ^{100}Ru (539.5 keV and 590.8 keV), the daughter nucleus of ^{100}Mo. Finally, the 207.3 ± 1.7 day half-life of ^{102}Rh [16] is long enough to allow shorter lived contaminants to decay away prior to measurement. The activity of the source was determined by comparing the intensity of the 475.1 keV γ–ray peak to that of the 661.6 keV γ–ray peak from a calibrated ^{137}Cs source.

Because the ^{100}Mo sample used for the measurement of the half-life time in [23] and [28] was in the form of a 10.6 cm diameter and 1.1 cm thick disk, the radial dependence of the 468.6 keV - 475.1 keV coincidence efficiency across the detector faces was crucial. This still applies for the ^{150}Nd sample, where the active material

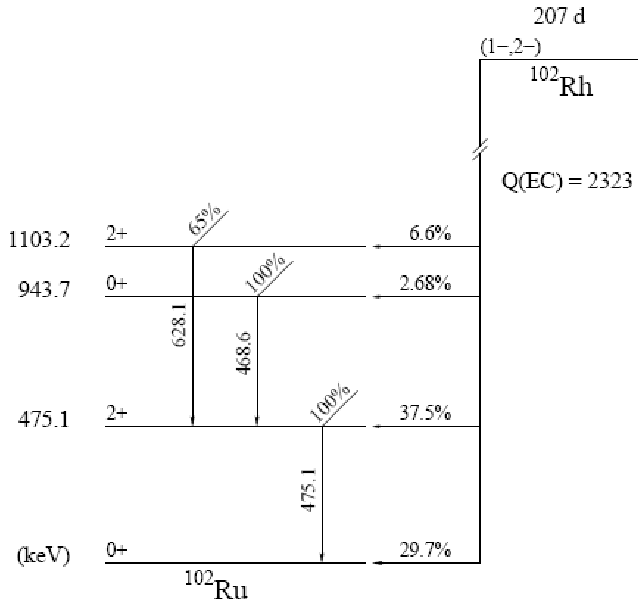

FIGURE 4.4: Decay scheme for ^{102}Rh showing the $0_1^+ \rightarrow 2_1^+ \rightarrow 0_{gs}^+$ sequence used for the coincidence efficiency measurement.

is 5.72 cm in diameter. We sandwiched our $1 \times 1 \times 0.5$ mm^3 ruthenium/rhodium source (in the following referred to as ^{102}Rh source) between ten disks (five on each side) of 10 cm diameter and 0.1 cm thickness of natural molybdenum to ensure that the overall thickness was the same as in the original $2\nu\beta\beta$ decay experiment on ^{100}Mo. This procedure yields the same average γ–ray attenuation provided the energy difference between the γ–ray pairs (468.6 keV - 475.1 keV versus 539.5 keV - 590.8 keV) is properly taken into account. Furthermore, it enables the ^{102}Rh source to be positioned not only at different radii, but also at different locations along the z axis, *i.e.*, along the common axis of the two HPGe detectors.

The previous coincidence efficiency measurement [23] was made along the radius r on the front faces of the HPGe detectors at the four locations r=0, 2, 4 and 5 cm, *i.e.*, in only one direction, assuming cylindrical symmetry of the detectors. The current measurements were performed across the entire diameter and in two perpendicular directions, *i.e.*, horizontally and vertically. Near the center we used 0.5 cm increments to better determine the efficiency in that region. A total of 25 data points were obtained in this manner between -4.5 cm $\leq r \leq$ 4.5 cm with the ^{102}Rh source sandwiched between two 0.5 cm–thick molybdenum disks. The measuring time for each data point varied between 12 and 48 hours, always obtaining at least 8000 coincidence events. At each location of the ^{102}Rh source the number of 468.6 keV – 475.1 keV coincidences was determined from the two–dimensional data area of pulse height in HPGe detector 1 versus pulse height in HPGe detector 2 (see Fig. 4.5).

The data were analyzed using the ROOT C/C++ Interpreter. The analysis program used gates and projections (see Fig. 4.6) along the axes to set close gates around the coincidence peaks and, after background subtraction, obtained the yields in each peak. The time-normalized yields were then corrected for dead time (<3%) and normalized to the activity of the ^{102}Rh source, taking into account its half-life. In order to obtain the efficiency for the ^{150}Nd $2\nu\beta\beta$ decay to the 0_1^+ state of ^{150}Sm the yields had to be corrected not only for the difference in attenuation between the ^{102}Ru and ^{100}Ru γ–ray lines of interest for ^{100}Mo, and the ^{102}Ru and ^{150}Sm γ–ray lines for ^{150}Nd, but also for the energy-dependent detection efficiency of our two identical HPGe detectors. For that purpose, the relative detection efficiency was measured with sources chosen to cover a wide range of energies: ^{137}Cs (661.657 keV), ^{60}Co (1173.228 keV, 1332.49 keV), ^{22}Na (511.000 keV, 1274.537 keV), and ^{152}Eu (411.1165 keV, 444 keV, 778.9045 keV, 867.378 keV, 964.1 keV, 1085.836 keV, 1112.074 keV, 1408.011 keV). See Figures 4.7 and 4.8 for these data with fit.

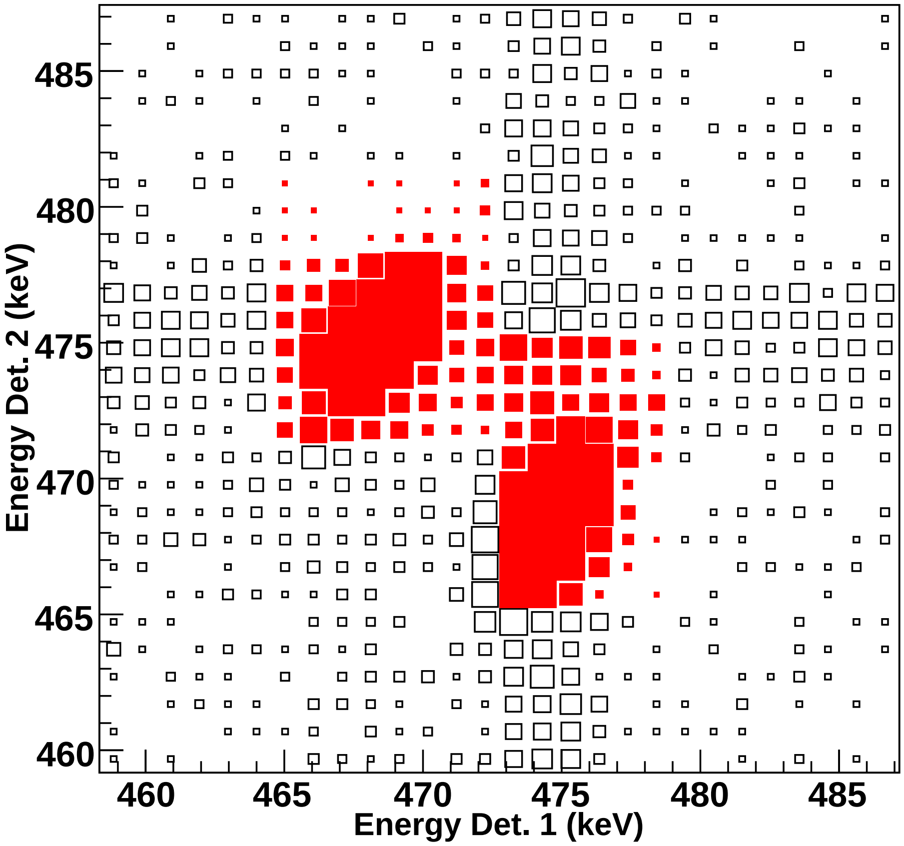

FIGURE 4.5: (Color online) Pulse height of HPGe detector 2 versus pulse height of HPGe detector 1 with the events associated with the 468.6 keV - 475.1 keV decay sequence of ^{102}Ru shaded in.

There are three steps to be taken to correct the ^{102}Rh data to reflect the coincidence efficiency for this ^{150}Nd source. First, by obtaining a fit to the relative efficiency data, the efficiency of either detector at any energy can be determined. This information is then utilized to scale the 468.6 keV-475.1 keV coincidence yields to the 334 keV-406.5 keV region of interest. The yields must be multiplied by this factor:

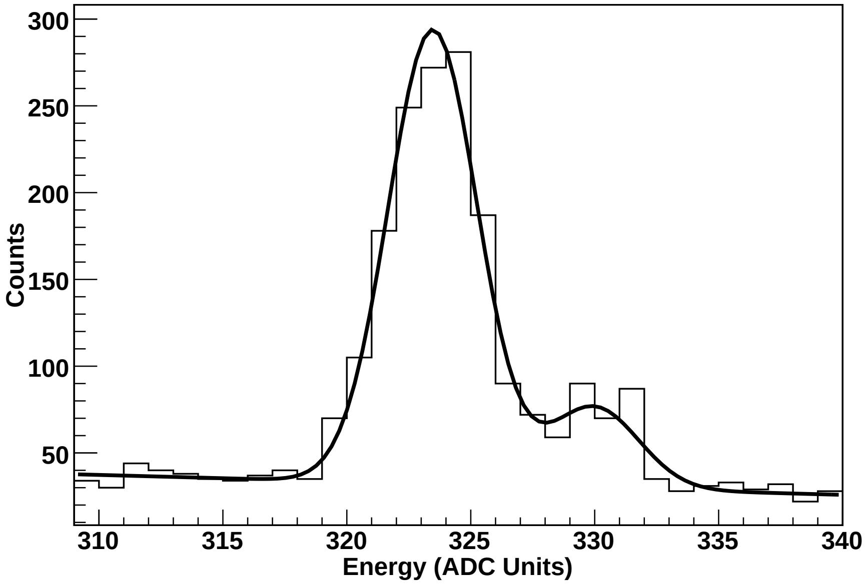

FIGURE 4.6: An example of a projection of the pulse height distribution from Fig. 4.5 onto the HPGe detector 2 axis and fit to data.

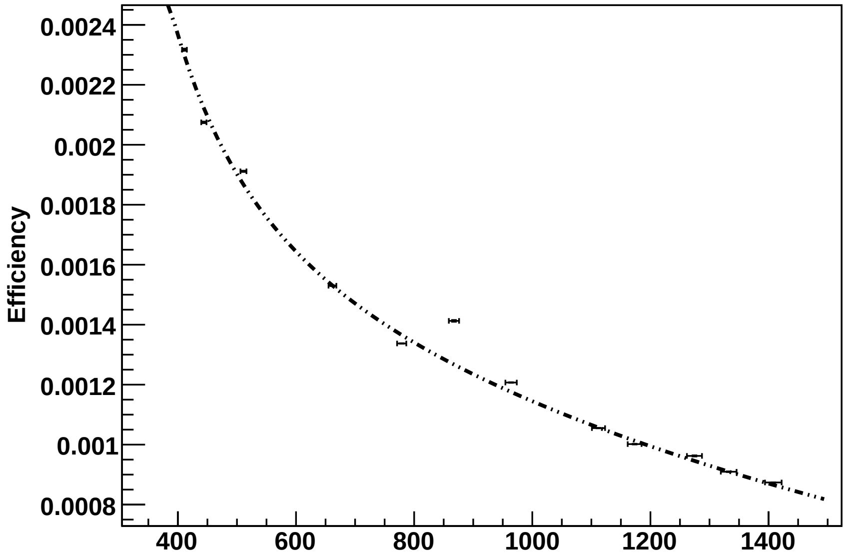

FIGURE 4.7: The relative efficiency for detector 1 operated in singles mode. The dashed curve is the fit to the data. The "outlier" at 867 keV has been previously observed for our ^{152}Eu source.

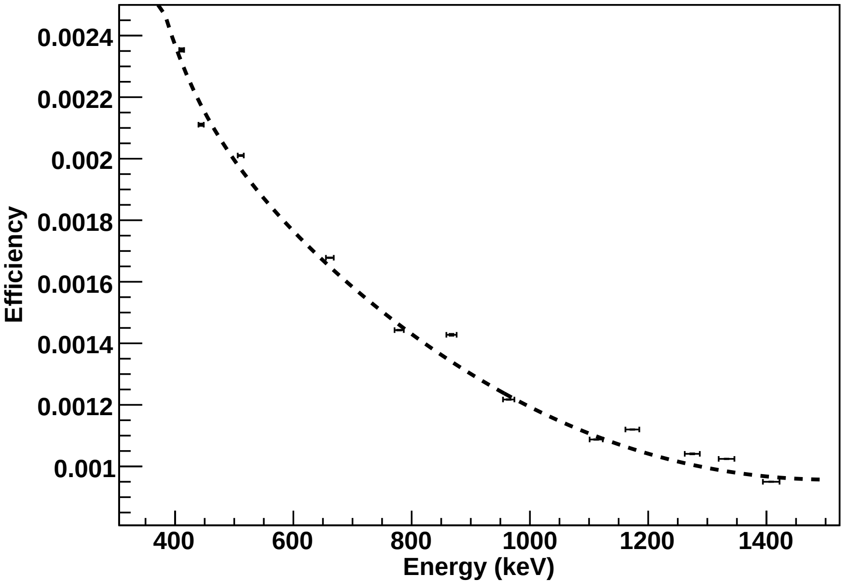

FIGURE 4.8: The relative efficiency for detector 2 operated in singles mode. The dashed curve is the fit to the data. Here, more weight was given to the data closer to the energy region of interest.

$$\frac{\epsilon_{\gamma\gamma}(334-406.5)}{\epsilon_{\gamma\gamma}(468-475)} = \frac{\epsilon_{1\gamma}(334)\epsilon_{2\gamma}(406.5)+\epsilon_{1\gamma}(406.5)\epsilon_{2\gamma}(334)}{\epsilon_{1\gamma}(468)\epsilon_{2\gamma}(475)+\epsilon_{1\gamma}(475)\epsilon_{2\gamma}(468)} = 1.64, \tag{4.1}$$

where the subscripts 1γ and 2γ refer to the relative efficiency of detectors 1 or 2 at that particular energy.

The different attenuation properties of the materials must then be taken into account. As the original coincidence efficiency measurement was taken for the ^{100}Mo measurement, molybdenum metal was used as the attenuator. The attenuator in this case is Nd_2O_3. The attenuation coefficients for 334 keV and 406.5 keV were obtained for this material from XCOM, a photon cross-sections database online at NIST [39]. This factor is then calculated:

$$\frac{A_{Nd_2O_3}(334)\times A_{Nd_2O_3}(406.5)}{A_{Mo}(468)\times A_{Mo}(475)} = 1.19, \tag{4.2}$$

where $\mathrm{A}_{Nd_2O_3}(\mathrm{E}_\gamma)$ and $\mathrm{A}_{Mo}(\mathrm{E}_\gamma)$ are the survival probabilities of a photon of energy E_γ in $\mathrm{Nd_2O_3}$ and molybdenum metal, calculated from the attenuation coefficients. Note that the attenuation must be calculated with 0.5 cm attenuation distance for the molybdenum metal, and 0.39 cm attenuation distance for the $\mathrm{Nd_2O_3}$.

Finally, the slight geometric change must be taken into account. The coincidence efficiency measurements were taken with 1 cm of molybdenum between the two detectors. The ^{150}Nd source is 0.78 cm thick, so the detectors are closer together. This is reflected in a change in the solid angle of the detectors available to the source. For a uniform circular disk source which emits isotropically aligned with a circular disk detector, both of which share a common axis through their centers, the solid angle may be calculated by solving the integral

$$\Omega = \frac{4\pi a}{s}\int_0^\infty \frac{exp(-dk)J_1(sk)J_1(ak)}{k}dk, \tag{4.3}$$

where the $J_1(x)$ are the Bessel functions of x, a is the radius of the detector, s is the radius of the source, and d is the separation between the source and detector faces [31]. There is not an analytic solution to this integral, so it was solved numerically via Mathematica. The solid angle must be calculated for the geometry with which the coincidence efficiency was measured, called Ω_{Mo}, and for the geometry in the current measurement, called Ω_{Nd}. The final scaling factor for the measured yields is then

$$\frac{\Omega_{Nd}}{\Omega_{Mo}} = 1.39. \tag{4.4}$$

Figure 4.9 shows the corrected yields for the ^{150}Nd experiment as a function of radius. As has been expected, the radial dependence of the coincidence efficiency was almost identical for the horizontal and vertical scans, within error associated

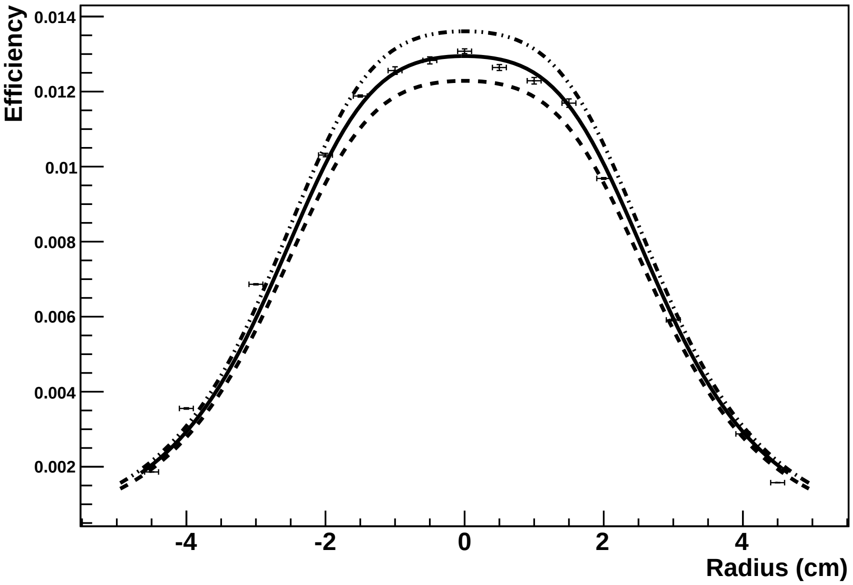

FIGURE 4.9: Average of coincidence detection efficiency data obtained for the horizontal and vertical scans as a function of r for the $E_{\gamma1}$=334.0 keV and $E_{\gamma2}$=406.5 keV coincidence. The data were taken with the^{102}Rh source ($E_{\gamma1}$=468.6 keV and $E_{\gamma2}$=475.1 keV) and then corrected for detection efficiency and attenuation differences between the two γ–ray pairs involved, and a geometric correction was applied. The curve through the data presents a least–squares fit. The upper and lower curves indicate the ±5.1% scale uncertainty associated with our data.

with the exact location of the ^{102}Rh source. Figure 4.9 shows the average of the horizontal and vertical efficiencies as a function of r. The error bars represent the statistical uncertainty of the data. Here, the effect of the position uncertainty of the ^{102}Rh source is added in quadrature to the statistical uncertainty. The coincidence efficiency is rather small, close to 1.3% in the -1 cm $< r <$ 1 cm range and then dropping smoothly to about 0.2% at r=4 cm. The size of the cavity of the Nd_2O_3 holder takes advantage of this effect, concentrating the powder in the most efficient region of the detectors.

The curve through the data points in Fig. 4.9 is a least-square fit using the functional form

$$\epsilon_{\gamma\gamma}(r) = \frac{a}{1 + br^2 + cr^4}, \tag{4.5}$$

where a, b, and c are free parameters and r=0 refers to the center on the front face of the HPGe detectors. A careful inspection reveals a slight asymmetry in the coincidence efficiency, providing slightly larger values for r< -2 cm. The lower (dashed) and upper (dashed-dotted) curves shown in Fig. 4.9 represent our systematic uncertainty of 5.1%, including the ±3% scale uncertainty associated with the ^{137}Cs γ-ray source.

The radial contribution to the coincidence efficiency was calculated using

$$\epsilon_r = \frac{2\pi \int \epsilon_{\gamma\gamma}(r) r dr}{2\pi \int r dr}, \tag{4.6}$$

where $\epsilon_{\gamma\gamma}(r)$ is the best fit obtained from an asymmetric fit to the data. This value is then corrected by the z-dependence of the coincidence efficiency measured in the present work and confirmed by Monte-Carlo simulation, where z is the distance from the face of the detector. There is a 10% decrease in efficiency at the center of the 1 cm thick molybdenum disk compared to the front and back faces. The resulting efficiency value for the ^{150}Nd geometry is ϵ_{tot}=(0.992±0.051)%, where the total uncertainty of 5.1% is due to the contributions listed in Table 4.1. They include an estimated 3% uncertainty due to the slightly irregular shape of our ^{150}Nd container.

For completeness, Figure 4.10 compares the previous results obtained in [23] for ^{100}Mo (data with error bars) to the fit through the present data. The agreement is good.

Briefly, the issue of angular correlation should be addressed for coincidence gamma rays. Gamma rays emitted in a cascade will have an angular correlation which depends on the types of decay sequence (such as $0^+ \rightarrow 2^+ \rightarrow 0^+$) and the multipolarities

Table 4.1: Summary of systematic error contributions.

Uncertainty Contribution	%
Intensity of Calibration Gamma Source	3%
Energy and Attenuation Correction Factor	1%
z-Dependence Correction Factor	1%
Geometry of ^{150}Nd Source	3%
Non-Symmetrical Efficiency Curve	2.4%
Dead Time	0.15%
Uncertainty in ^{102}Rh Half-Life	0.15%
Total	5.1%

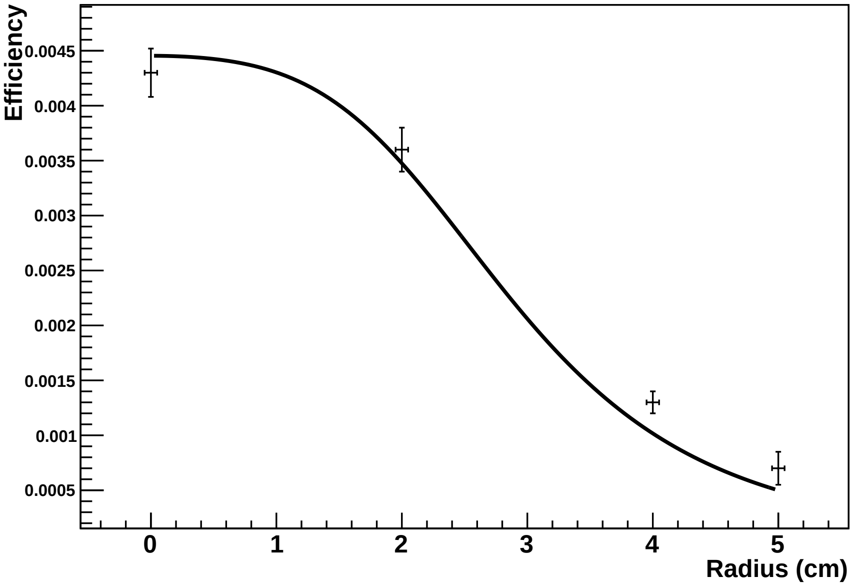

FIGURE 4.10: Plotted are the data points acquired in the previous efficiency measurement described in [23]. The curve is the fit to the data points acquired in the newer measurement, published in [28].

associated with these transitions. The present measurement is most concerned with the $0^+ \rightarrow 2^+ \rightarrow 0^+$ decay sequence, but the $2^+ \rightarrow 2^+ \rightarrow 0^+$ also plays a role for ^{150}Nd.

The general angular distribution for multipole radiation is given by

$$W(\theta) = 1 + \sum_{k=1}^{L} a_{2k} cos^{2k}\theta, \tag{4.7}$$

where the coefficients, a_{2k}, depend on the angular momenta of the initial and final states of the nucleus, I_i and I_f, and the angular momentum L transferred to the photon. For $0^+ \rightarrow 2^+ \rightarrow 0^+$ transitions, which proceed only through electric quadrupole (E2) radiation, the angular correlation is given by

$$W(\theta) = 1.250 - 3.75cos^2\theta + 5.00cos^4\theta, \tag{4.8}$$

where θ is the angle between the two gamma rays.

Due to the selection rules, there is no mixing of multipolarities for this transition, so all $0^+ \rightarrow 2^+ \rightarrow 0^+$ transitions follow this angular correlation. Since the ^{102}Rh source used for the efficiency measurement also decayed by $0^+ \rightarrow 2^+ \rightarrow 0^+$, no angular distribution corrections need to be made to the efficiency for detection of $0^+ \rightarrow 2^+ \rightarrow 0^+$ transitions.

For the $2^+ \rightarrow 2^+ \rightarrow 0^+$ however, the angular distribution is not so straightforward. In the first part of the transition, the photon can be a product of either magnetic dipole (M1) or electric quadrupole (E2) radiation. The fraction of gamma rays which participate in M1 or E2 is different for each $2^+ \rightarrow 2^+ \rightarrow 0^+$ transition. The coefficients a_{2k} were measured for the $2_2^+ \rightarrow 2_1^+ \rightarrow 0^+$ transition in ^{150}Sm and are given in Equation 4.9. [24] The distributions in Equations 4.8 and 4.9 are plotted in Figure 4.11. The angular correlation for the $2_2^+ \rightarrow 2_1^+ \rightarrow 0^+$ transition is much more isotropic than the $0^+ \rightarrow 2^+ \rightarrow 0^+$,

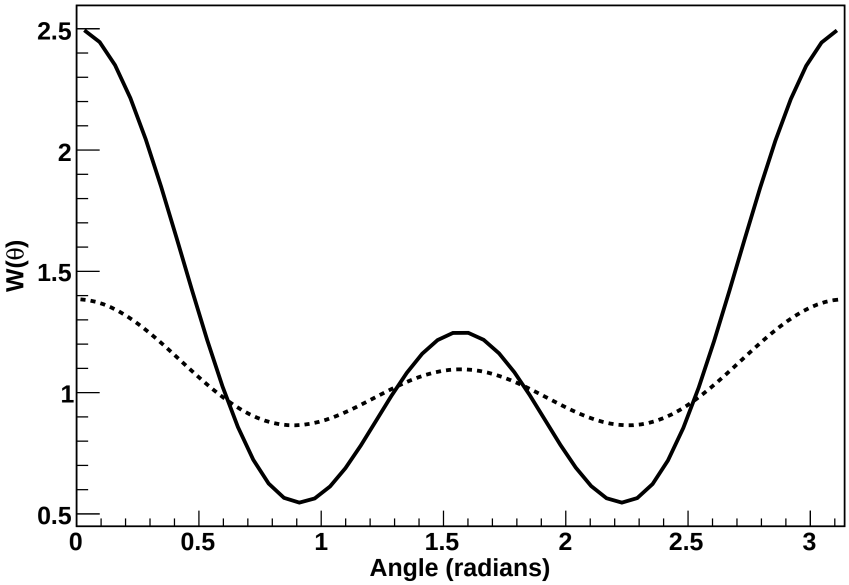

FIGURE 4.11: Plotted are the angular correlations shown in Equations 4.8 (solid curve) and 4.9 (dotted curve).

$$W(\theta) = 1 + 0.055cos^2\theta + 0.33cos^4\theta. \tag{4.9}$$

By comparing the singles count rate to the coincidence count rate, a measure of the angular contribution over a solid angle can be obtained. To correct for this contribution, this value was divided out for each radial measurement and multiplied by the average angular correlation obtained from Equation 4.9.

4.3 Rejection of Background Candidates

To correctly interpret the results of the data analysis, a thorough understanding of the types of potential background candidates must be obtained. In this section, the types of backgrounds which can contribute to the region of interest will be discussed. Specifically, it must be verified that there are no other sources which can produce a 334.0 keV gamma ray in coincidence with a 406.5 keV gamma ray.

Type of Rock	^{40}K Bq/kg	^{238}U Bq/kg	^{232}Th Bq/kg
Limestone	90	27	7

Table 4.2: Typical concentrations of naturally occurring radioactive isotopes in limestone. [45]

4.3.1 Background Sources

Natural Decay Chains

All materials, unless processed to remove them, naturally contain some amount of Potassium (K), Thorium (Th), and Uranium (U). The natural abundance of ^{40}K is 0.0117 % and has a half life of 1.248×10^{9} y. Thorium and Uranium contribute to natural radiation via three natural decay chains. The isotopes ^{232}Th, ^{235}U, and ^{238}U start these three chains, which end at ^{208}Pb, ^{207}Pb, ^{206}Pb respectively, all stable lead isotopes. Since the TUNL-ITEP double-beta decay setup is located in a limestone mine (see Section 3.2.6), typical concentrations of these isotopes in limestone are of interest and are listed in Table 4.2.

Radon can also be a worrisome contaminant as it is gaseous and can plate out on surfaces in the detector setup. Radon is a by-product of the natural decay chains. In the ^{232}Th series, the radon isotope is ^{220}Rn, with a half life of 55.6 s. In ^{235}U, the radon isotope is ^{219}Rn with a half life of 3.92 s, and in ^{238}U, the radon isotope is ^{222}Rn with a longer half life of 3.82 days. Because of the ^{232}Th contamination in the ^{150}Nd sample, ^{220}Rn is definitely present; any naturally occurring contamination from ^{220}Rn is in addition to the sample contamination. The natural abundance of ^{235}U is only 0.72% compared to the natural abundance of ^{238}U, which is 99.27%; therefore, it is unlikely that there will be noticeable contamination from ^{219}Rn.

Mean values for radon concentration are 5-10 Bq/m^{3} in the free air. There can be large fluctuations due to geography, time of day, and season. The maximum at night is approximately two times the daily minimum, and the summer maximum is about three times the winter minimum. Geographically, radon concentrations are higher away from coastlines in continental locations, and are lower on islands and near the coast, in general. [45] Evidence of ^{222}Rn is found by detecting gamma emissions from its daughters, specifically, in the β^- decay of ^{214}Bi to ^{214}Po. In Figure 4.12, the characteristic 609.320 keV gamma-ray emission was monitored over time. The decay rate seen in the detector was corrected for the gamma-ray intensity of 45.49%, but as the efficiency of either HPGe detector is not known from all directions, the concentration of radon cannot be calculated. An effort was made to reduce the radon concentration in the air around the detectors by purging the detector cavity with the blow-off from the liquid nitrogen supply dewars. The purge appears to have made some progress in reducing radon concentration. Though the radon contamination does not lead to specific coincidence events in the regions of interest, it does produce some gamma rays uncomfortably close to the region of interest. Also, the contamination increases the Compton continuum and thus the constant background in the regions of interest.

Starting with ^{238}U, no gamma rays of note are produced until the metastable state of ^{234m}Pa β^- decays to ^{234}U. Though the gamma-ray energies for this decay are universally less than 1%, there is one gamma-ray emission of interest which occurs with energy 742.8 keV and intensity 0.11%. This gamma-ray transition is notable because it can Compton scatter directly into the region of interest. For the ± 3 keV gate around the region of interest, the 742.8 keV gamma ray could scatter with energies between 331 and 337 keV in coincidence with 411.8 and 405.8 keV, or between 403.5 and 409.5 keV in coincidence with 339.3 and 333.3 keV. This potential problem will be addressed in Section 4.3.2.

From ^{234}U to ^{226}Ra, no gamma rays of note are emitted. In the alpha decay of ^{226}Ra to ^{222}Rn, a very characteristic gamma ray is emitted at 186.2 keV and 3.59%

intensity. Though this is below our threshold, it would be interesting in the future to detect this gamma ray. ^{222}Rn then decays via the release of an alpha particle to ^{218}Po, which subsequently alpha decays to ^{214}Pb. There are a number of gamma rays associated with the next decay in the series, the β^- decay of ^{214}Pb to ^{214}Bi, the most intense of which are: 242.0 keV (7.251% intensity), 295.2 keV (18.42%), 351.9 keV (35.6%), and 786.0 keV (1.06%). None of the gamma-ray energies released in this decay are closer than 10 keV to the regions of interest. Another onslaught of gamma rays is associated with the β^- decay of ^{214}Bi to ^{214}Po. The most intense of these are: 609.3 keV (45.49%), 768.4 keV (4.895%), 1120.5 keV (14.92%), 1238.1 keV (5.83%), 1764.5 keV (15.30%), and 2204.1 keV (4.92%). Some very low-intensity gamma-ray energies in this decay are within our regions of interest. These are: 333.37 keV (0.065%), 334.78 keV (0.018%), and 405.72 keV (0.169%). Because neither of the transitions accompanied by the gamma rays near 334 keV occur in coincidence with the one at 405.72 keV, they are not expected to contribute to the regions of interest. The remainder of the decays down to stable ^{206}Pb do not produce any gamma rays of note [11].

The largest source of background from a natural decay chain is the ^{150}Nd sample itself. This sample was leased from Oak Ridge National Laboratory (ORNL) where it was enriched in the calutrons. The enrichment process also resulted in a contamination of ^{232}Th decay products. This contamination manifests itself in a multitude of gamma-ray emissions from the β^--decay of ^{228}Ac to ^{228}Th. Three of these characteristic gamma-ray emissions are in close proximity to the region of interest of the 333.9-406.5 keV coincidence. They are 328.000 keV, 338.320 keV, and 409.462 keV with intensities of 2.95%, 11.27%, and 1.92%, respectively [11]. Again, as in the ^{222}Rn decay chain, none of these gamma-ray energies occur in coincidence with each other. However, the 328.000 keV and the 338.320 keV gammas do appear in the summed event histogram shown in Figure 4.3 as excesses of counts to the left and

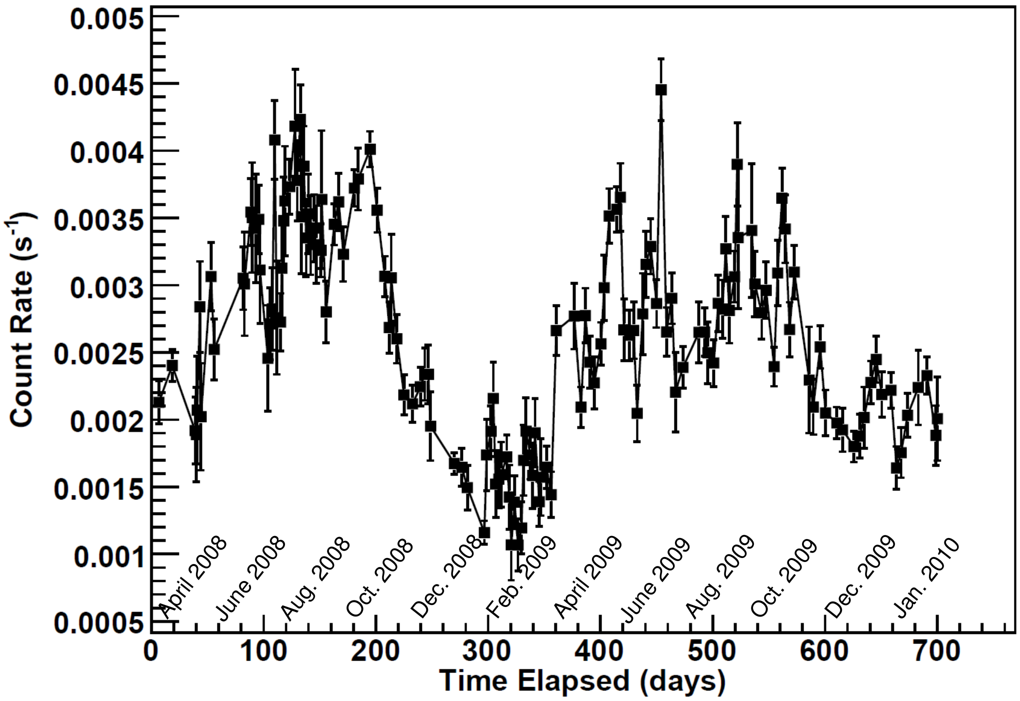

FIGURE 4.12: The radon contamination measured in decays of ^{214}Bi starting from April 2008. The LN purge was installed in October 2008. The seasonal dependence is especially noticeable.

right of the region of interest at 334 keV. This feature will be discussed further in Section 4.3.2.

Further down the ^{232}Th decay chain, there are other intense gamma rays which should be noted. In the β^- decay from ^{212}Pb to ^{212}Bi, the characteristic 238.6 keV gamma ray is emitted with an intensity of 43.6%. The next link in the chain, the ^{212}Bi β^- decay to ^{212}Po produces a 727.3 keV gamma ray at 6.67% intensity which can create a Compton scattering peak near the region of interest. ^{212}Po then alpha

Decay	ROI Gamma-Ray Energy (keV)	Intensity (%)	Coincidence Gamma-Ray Energy (keV)	Intensity (%)
^{228}Ac→^{228}Th	332.370	0.40	399.62	0.029
^{228}Ac→^{228}Th	332.370	0.40	419.42	0.021
^{228}Ac→^{228}Th	338.320	11.27	372.57	0.0067
^{228}Ac→^{228}Th	338.320	11.27	377.99	0.025
^{228}Ac→^{228}Th	338.320	11.27	399.62	0.029
^{228}Ac→^{228}Th	338.320	11.27	416.30	0.0132
^{228}Ac→^{228}Th	338.320	11.27	419.62	0.021
^{152}Eu→^{152}Gd	411.116	2.237	344.28	26.6
^{214}Bi→^{214}Po	405.72	0.169	304.2	0.019
^{214}Bi→^{214}Po	405.72	0.169	314.9	?

Table 4.3: Potential coincidences which could contribute near the region of interest (ROI).

decays to ^{208}Pb, the endpoint of this decay chain. ^{212}Bi can also alpha decay here to ^{208}Tl, whose decay via a β^- decay to stable ^{208}Pb produce some very intense gamma rays at 510.77 keV (22.6%), 583.2 keV (85.0%), 860.6 keV (12.5%), and 2614.5 keV (99.75%).

This decay chain can also contribute to the areas surrounding the regions of interest via true coincidences which will form peaks in the one-dimensional summed event spectrum. In Table 4.3 these coincidences are listed. Because the statistics are so low, and the intensities of these coincidences often so small, it is difficult to verify that they explain any excesses of counts in the areas around the region of interest.

Oddly, a higher count rate of the ^{228}Ac-associated gamma rays is seen in detector 2. In the past, the ^{150}Nd sample was in two batches, which were mixed during the purification process. It appears that this mixture is not homogeneous.

There are two other contaminants to the sample which can be seen in the two-dimensional spectrum, and in one case, contribute to the background near the ROI. The first of these is ^{176}Lu, which β^- decays to ^{176}Hf. Lutetium is a rare-earth metal which forms the same oxide structure, Lu_2O_3, as Neodymium. The natural abundance of the isotope ^{176}Lu is 2.59% and it has a half life of 3.76×10^{7} years. The transition to ^{176}Hf does not emit gamma rays which contribute in the region of interest, but for neutrinoless double-beta decay experiments which may use enriched ^{150}Nd in the future, such as SNO+, the potential contamination by ^{176}Lu might be of interest.

The second rare-earth contaminant which has been found in this ^{150}Nd sample is ^{152}Eu. Again, Europium forms the same oxide structure as Neodymium, Eu_2O_3, and ^{152}Eu β^- decays to ^{152}Gd and emits (among others) a gamma ray at 344.3 keV (26.6%) in coincidence with a gamma ray at 411.1 keV (2.24%). The TCut which defines the 406.5 keV ROI cuts into the tail of this coincidence which appears in the two-dimensional spectrum. This seems to account for an excess of counts near 344 keV.

4.3.2 Identification of Natural Background in Data

Because the background discussed in the previous section cannot ever be completely removed, its contribution in and around the region of interest must be understood. Mostly, these decays contribute in a general way to the Compton continuum, but a few of the gamma-ray emissions make contributions in the one-dimensional histograms discussed in Section 4.1. The first specific natural background lines to be discussed are the 742.8 keV gamma ray emitted in the decay of ^{234m}Pa, the 768.4 keV gamma ray emitted in the decay of ^{214}Bi, and the 727.3 keV gamma ray emitted in the decay of ^{212}Bi.

Examining the singles spectrum near these energies, it can immediately be observed that the 742.8 keV full-energy peak is substantially smaller than the surrounding 727.3 keV and 768.4 keV full-energy peaks. If the one-dimensional coincidence spectrum is then examined, the full-energy Compton scattering peaks attributed to 727.3 keV and 768.4 keV can be identified. By comparing the intensity of the full-

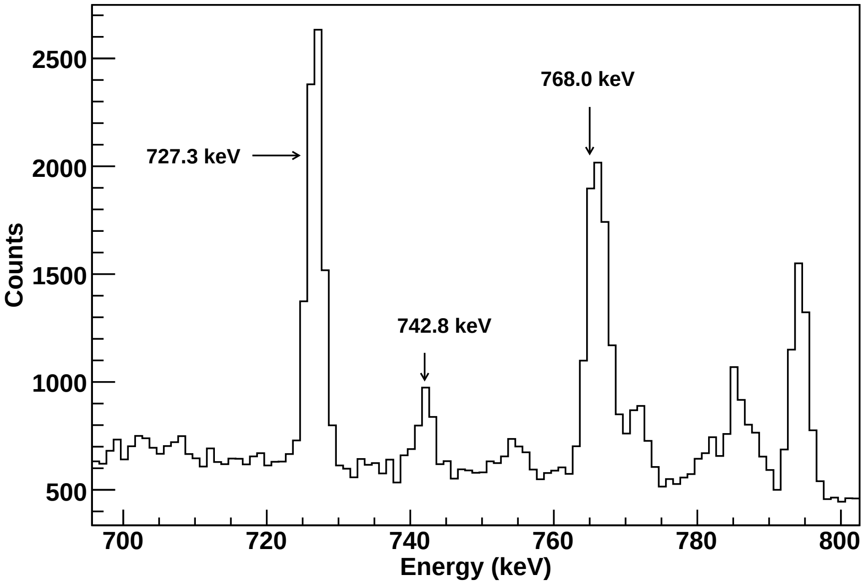

FIGURE 4.13: A comparison of the 742.8 keV gamma-ray peak from the decay of ^{234m}Pa to surrounding peaks.

energy Compton scattering peaks to the intensity of the full-energy singles peak, it can be seen that the 742.8 keV full-energy Compton scattering peak would not contribute above background in the region of interest (see Figure 4.14).

The other background which contributes in the areas surrounding the region of interest for 334 keV are the gamma rays emitted in the decay of ^{228}Ac to ^{228}Th which have energies of 328.000 keV and 338.320 keV. In the two-dimensional spectrum near the regions of interest, these gamma-ray transitions are responsible for creating vertical and horizontal lines at the aforementioned energies which extend up to 1400 keV. As discussed in Section 4.1, these are formed when the full energy of a gamma-ray transition is deposited in one detector in coincidence with a Compton-scattered gamma ray in the other detector which does not deposit its full energy. The effect of the one-dimensional summed event spectrum is to take a cross section of the two-dimensional energy spectrum. Thus, when the cross section is taken across one of

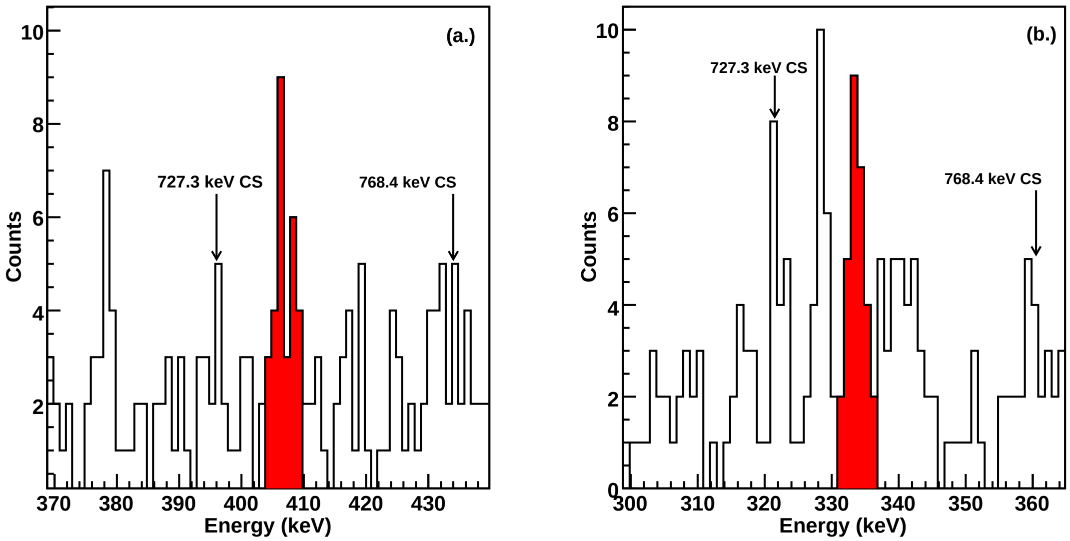

FIGURE 4.14: (Color online) Same as Figure 4.3 with the Compton scattering peaks from 727.3 keV and 768.4 keV labeled.

these horizontal or vertical lines, an excess of counts in the one-dimensional spectrum can occur. This is the cause of the ”peaks” which occur noticeably at 328 keV, and less definitely at 338 keV.

Two issues arise from this realization that the cross section of Compton scattering coincidences can create peaks in the one-dimensional summed event spectrum. The first of these is whether a peak can be expected in the other one-dimensional spectrum from a Compton-scattering coincidence with the 409.5 keV peak in the decay of ^{228}Ac to ^{228}Th. The second of these also helps in the discussion of the previous issue, and that is related to the intensities of the Compton-scattering coincidence peaks. The intensities of the full-energy peaks for 328.000 keV, 338.320 keV, and 409.462 keV are 2.95%, 11.27%, and 1.92%, respectively, but the Compton-scattering coincidence peaks do not appear to follow these intensities. To understand the contribution of the 409.5 keV Compton scattering, the intensities must be calculated using the branching ratios to all states which make a transition through the 328.000 keV level, the 396.078 keV level (through which transition results in the 338.320 keV gamma ray), and the 1431.979 keV level (through which transition results in the 409.462 keV gamma ray). It can be found that 2.9% of all ^{228}Ac decays to ^{228}Th proceed in coincidence with 328.000 keV with energies large enough to Compton scatter into the 406.5 keV region of interest. Similarly, the percentage of decays in coincidence with 338.320 keV is 2.3%, and for 409.5 keV, only 0.26%. Thus, it makes sense that the excesses of counts in the 328.000 keV and 338.320 keV areas are of a comparable size, and it can be deduced that only one-tenth of those counts are expected at 409.5 keV.

4.3.3 Cosmic-Ray Backgrounds

Cosmic rays are an ubiquitous form of background. For a low-background counting system such as the TUNL-ITEP double-beta decay setup, cosmic rays could account for a significant portion of the background. Primary cosmic radiation can be either of galactic or solar origin and is made up of about 70% protons, 20% helium nuclei, and 10% heavier nuclei. They enter the atmosphere with energies ranging from 10^4 to 10^{10} GeV. When these primary particles interact with the atmosphere, the result is a huge assortment of secondary particles including pions, muons, electrons, protons, neutrons and gamma rays with energies as high as hundreds of MeV. About 80% of the charged-particle secondary radiation at sea level consists of muons, with an intensity of one muon per cm^2 per minute [20], [45]. The muons themselves are quite penetrating, and also result in the production of fast neutrons, which can activate detector materials and shielding.

Fast neutron flux at sea level is the result of the muons interacting with high-Z materials. The neutrons can then interact in materials via (n, p), (n, α), (n, 2n), and (n,n'γ). Reducing this background contribution can be done by going underground. The muon flux at different overburdens in units of meters water equivalent (m.w.e.)

is shown in Figure 4.15 [8]. By installing the TUNL-ITEP double-beta decay setup at KURF, the effect of the muon flux was noticeably reduced.

Cosmic-ray background could permeate the regions of interest via proton and neutron reactions on nuclei near or within the source, resulting in production of the excited state in the final nucleus which would appear like a double-beta decay event. It must be shown that the events seen in the region of interest were not produced by any other mechanism than double-beta decay.

Proton Activation

One of the most dangerous potential background candidates results from proton activation of the ^{150}Nd nucleus. A significant proton flux through the apparatus could result in the (p,n) activation of ^{150}Nd, producing the nucleus which would be the intermediate state in double-beta decay, ^{150}Pm. ^{150}Pm can then β decay to ^{150}Sm with a half-life of 2.68 hours. This β decay can produce the excited-state decays which would be attributed to a double-beta decay event.

Proton activation can occur not only during the experiment, but any time the source has been subjected to a significant proton flux, such as in air transport, or while it was above ground. Because the half life of the activated nucleus is so short, any activation due to transport would have died away long ago, and so the only concern in this case would be continual activation during the experiment.

As has been shown, the cosmic-ray flux has been significantly reduced by going underground. Even so, because of the extremely long half life of double-beta decay, even a small flux is reason for concern. Even though it is unlikely that a primary cosmic-ray proton can penetrate the overburden at KURF, secondary interactions like (n,p) may certainly occur.

To investigate the (p,n) case, the β decay of ^{150}Pm must be studied. As can be seen in Figure 4.16, only 1.4% of the β decays feed the 0^+_1 excited state. It should also

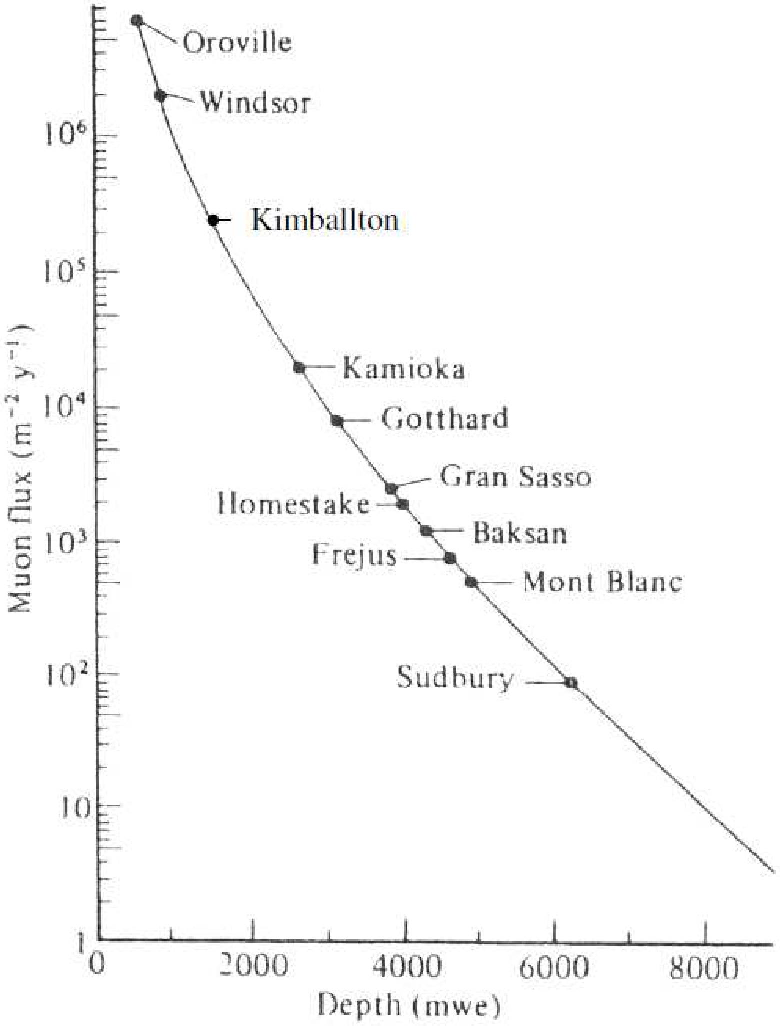

FIGURE 4.15: The reduction in the cosmic muon flux vs. the overburden in m.w.e. for various underground sites, not including Kimballton [8]. The Kimballton point was added by knowing the m.w.e. depth to see what reduction was gained.

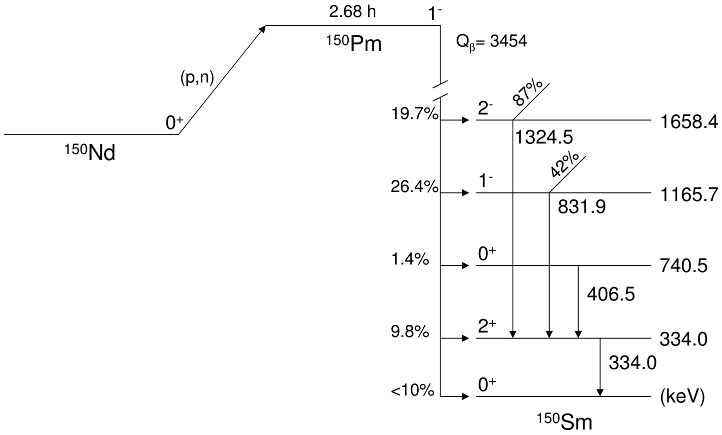

FIGURE 4.16: The decay scheme of ^{150}Pm β decay after (p,n) activation of ^{150}Nd.

be noted that 19.7% of the β decays feed the 2^- state at 1658.4 keV, and 26.4% feed the 1^- state at 1165.7 keV. Both of these states decay emitting a 1324.5 keV gamma or a 831.9 keV gamma, respectively, in coincidence with the 334.0 keV gamma. The probability of these decays are much larger than the probability of the decay to the 0_1^+ excited state, so searches for these higher excited-state coincidences will reveal the possible contribution to the double-beta decay regions of interest. Indeed, no coincidences were observed at either 1324.5-334.0 keV or 831.9-334.0 keV making it extremely unlikely that (p,n) activation of ^{150}Nd contributes to the background in the regions of interest.

Neutron Background

Finally, a significant neutron flux through the detectors and source disk provides another source of background. The lead brick enclosure discussed in Section 3.2.4

is not very effective in stopping neutrons; the cross section for neutron capture is rather small. The source of a neutron flux could be due to primary cosmic-ray flux, or from secondary interactions occurring in the room or in the setup. Neutrons can be produced by high-energy protons interacting in the lead. A variety of interactions are available once a neutron flux is present, such as (n,γ) capture, (n,n'γ), elastic scattering, or even (n, 2n).

The presence of a neutron flux can be checked by examining the γ-ray energy singles spectrum for characteristic neutron interactions with germanium nuclei. Neutrons which scatter inelastically off germanium nuclei in the crystal generate peaks which are broadened due to the recoil of the nucleus. Referring again to Figure 3.6, when the TUNL-ITEP double-beta decay setup was operated at the LBCF, at 596 keV and at 691 keV there are peaks with the distinctive sawtooth shape originating from (n,n'γ) on ^{74}Ge (which is 36.5% naturally abundant) and ^{72}Ge (27.4%). Once at KURF, though, these peaks are indistinguishable from background.

5

Results and Conclusions

Now that the background, theory, method of detection, and analysis procedure have been addressed, the results of the study of ^{150}Nd double-beta decay to excited final states can be discussed. In this chapter, these results and their significance will be presented.

5.1 Double-Beta Decay of ^{150}Nd to 0_1^+

As stated in Section 4.1, obtaining the raw data is a straightforward procedure following the accumulation of coincidence data. There are no complex data processing or analysis routines. The strength of the data lies in its simplicity; the data is compiled over the entire counting period, and any positive peaks in or near the region of interest must be identified.

In the search for double-beta decay of ^{150}Nd to the 0_1^+ state (740.5 keV) of ^{150}Sm, data were accumulated over a total of 391 days. Recall that identification of this decay involves the simultaneous detection of the coincidence de-excitation ($0_1^+ \rightarrow 2_1^+ \rightarrow 0_{gs}$) gamma-ray photons with energies of 334.0 keV and 406.5 keV. The branching ratio for this cascade is 100%. Gamma-ray energy spectra in coincidence

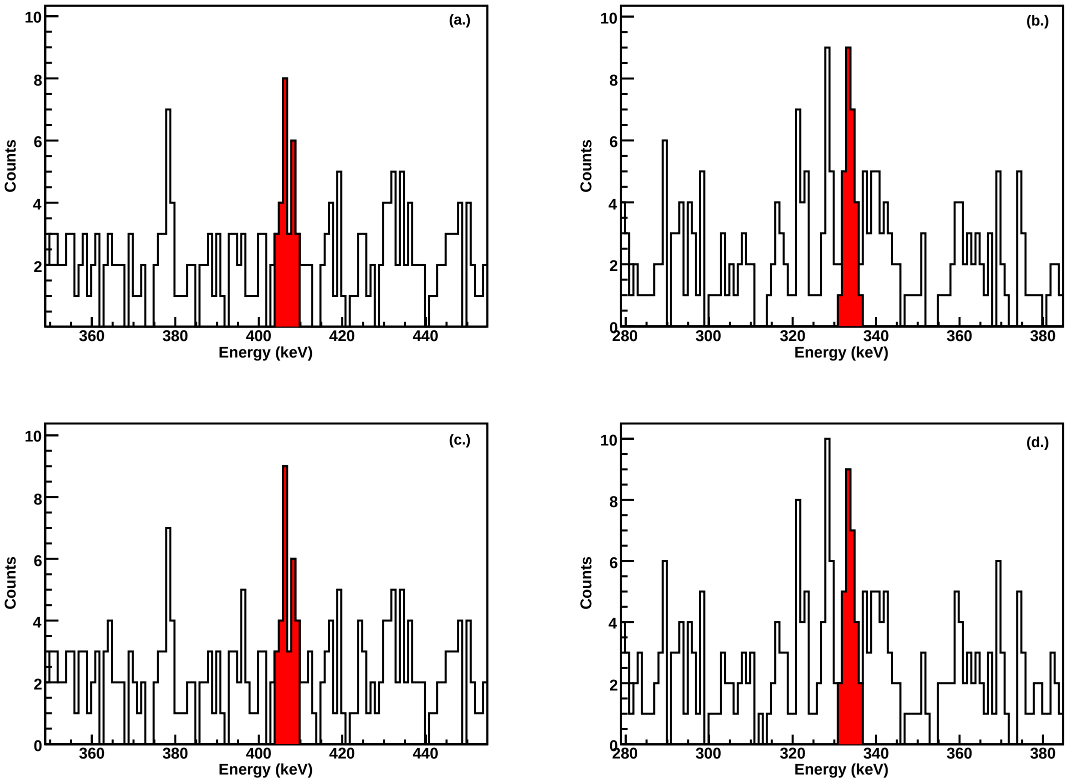

FIGURE 5.1: Coincidence data from 391 days of run time. Spectra (a.) and (c.) are in coincidence with 333.9 keV, and (b.) and (d.) are in coincidence with 406.5 keV. The energy coincidence cut shown is ±2.5 keV on Detector 2 and ±3.0 keV on Detector 1 in spectra (a.) and (b.), and ±3.0 keV on both detectors in spectra (c.) and (d.). Bins shaded in red are within the regions of interest.

with 334.0 keV and 406.5 keV, presented in Figure 5.1 shows the detection of the coincidence events. There are two coincidence widths shown in Figure 5.1. The width of the coincidence window in the upper two spectra is ±2.5 keV for Detector 2 (due to its slightly better resolution and the excess of ^{228}Ac decays seen by this detector), and ±3.0 keV for Detector 1. For the bottom two spectra, the coincidence window is ±3.0 keV. Though there are other peaks near the region of interest, the excess of counts at the correct energy is undeniable. The significance of the events in the region of interest depends on the identification of the surrounding background peaks.

The half-life calculation can be accomplished through the use of the definition in Equation 5.1,

$$T_{1/2} = \frac{ln2N_0t\epsilon_{\gamma\gamma}^{tot}}{N_{\gamma\gamma}}. \tag{5.1}$$

Here, N_0 is the number of ^{150}Nd nuclei in the sample, t is total counting time (391 days or 1.07 years), $\epsilon_{\gamma\gamma}^{tot}$ is the total coincidence detection efficiency for the 334-406.5 keV cascade, and $N_{\gamma\gamma}$ is the number of detected coincidence events minus background. The neodymium sample obtained from Oak Ridge National Laboratory consists of 50.00 g of Nd_2O_3, which corresponds to 42.87 g of Nd. This is enriched to 93.60% ^{150}Nd, which is 40.13 g ^{150}Nd. The value of N_0 is then 1.612×10^{23} nuclei of ^{150}Nd. As mentioned in Section 4.2, the coincidence efficiency for the 334.0-406.5 keV cascade is $\epsilon_{\gamma\gamma} = (0.992 \pm 0.051)\%$.

Strictly speaking, in evaluation of background, existing peaks should be removed from the spectrum before background integration. To this end, effort must be made to identify all background peaks surrounding the regions of interest. In low-background counting experiments, this is a difficult endeavor due to the small statistics involved. In Figure 5.1 (a.) and (c.), it is apparent that there is a peak located at 379 keV which can be attributed to a coincidence between gamma rays emitted from a cascade from the 1531.5 keV level in ^{228}Th. Thus, it is excluded from the background integration. In Figure 5.1 (b.) and (d.), the region from 315 keV to 345 keV was excluded from the background integration. These background integrations results in an average background of 2.0 counts per keV. In spectra (a.) and (b.) in Figure 5.1, the region of interest is taken to be 5.5 keV wide, and in (c.) and (d.), it is 6.0 keV wide. There are 27 raw events in (a.) and (b.), and 29 raw events in (c.) and (d.). After subtracting the background from the raw events, an average of 16.5 ± 5.5 events was obtained. Inserting this into Equation 5.1, the following value is obtained.

$$T_{1/2} = (0.72^{+0.36}_{-0.18} \pm 0.04(syst.)) \times 10^{20} years. \tag{5.2}$$

As radioactive decay is a truly random process, it should also be verified that the events in the region of interest are properly distributed over time. If, for instance, some of the events occurred in a sudden burst, another process could be indicated. In the case of a random process, the intervals between events behave in a well-understood manner. The distribution can be described as

$$P(t) = re^{-rt}, \tag{5.3}$$

where r is the average rate of events and t is the time interval between successive events. In this case, 29 events were detected over 391 days, which gives a rate of $r = (0.07 days)^{-1}$. Figure 5.2 shows the distribution of the time intervals between successive events. The function defined by Equation 5.3 is plotted over the distribution. The distribution does behave as a random process.

5.2 Double-Beta Decay of ^{150}Nd to Higher Excited States

The double-beta decay of ^{150}Nd to higher excited states of ^{150}Sm was also studied. Following Figure 3.1, the coincidence energies for these three cascades are 712.2 keV - 334.0 keV, 859.9 keV - 334 keV, and 921.2 keV - 334 keV. Note that the 712.2 keV transition and the 859.9 keV transition are both $2^+ \rightarrow 2^+ \rightarrow 0^+$ decays, and the efficiency must be adjusted accordingly. As seen in Figure 5.3, no events were detected above background for any of these decays, meaning that half-life limits may be set for double-beta decay to these states. The half-life limit is given by

$$T_{1/2} > \frac{ln2 N_0 t f_b \epsilon^{tot}_{\gamma\gamma}}{N_d}, \tag{5.4}$$

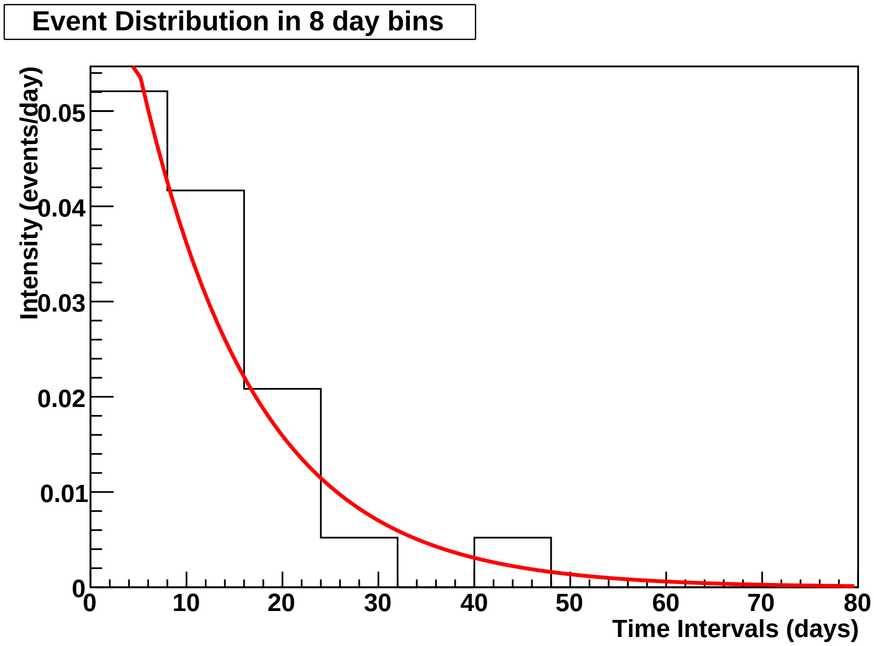

FIGURE 5.2: (Color online) Shown is the distribution of the time intervals between successive events. The solid line is not a fit, but a plot of Equation 5.3. The distribution behaves as expected for a random process.

where f_b is the branching ratio for the particular cascade. N_d is a value chosen as recommended by the Particle Data Group [22]. It is determined by a statistical estimator which is derived for a process obeying Poisson statistics. The definition of N_d is given as the desired upper limit on the signal above background, and it depends on the chosen level of certainty. For double-beta decay half-life limits, reporting the 90% confidence level (CL) has become standard. For the 90% CL, N_d is the maximum signal which will be observed in 90% of all random repeats of the experiment, or there is a less than 10% chance of observing a count rate above N_d.

The first case to be considered is the $2^+_2 \rightarrow 2^+_1 \rightarrow 0^+_{gs}$ transition, which proceeds through the emission of a 712.2 keV gamma ray in coincidence with the 334.0 keV gamma ray. The $\epsilon_{\gamma\gamma}$ for this transition is (0.275±0.014)%, and the branching ratio is 89%. The accumulated data can be seen in Figure 5.3 (a.) and (b.). The background is 2.5 counts per keV. The large peak seen at 707.4 keV in spectrum (a.) is a coincidence peak in the ^{228}Ac decay to ^{228}Th (the associated gamma ray in the decay has an energy of 332.0 keV). The peak labeled at 1001.0 keV in spectrum (b.) is a Compton scattering peak from the decay of ^{234m}Pa to ^{234}U. The typical Compton scattering coincidence peaks at 328 keV and 338 keV can also be seen. With 8 counts in the region of interest, a positive signal is not detected. The half-life limit is found to be $T_{1/2} > 2.17 \times 10^{19}$ years.

The next case is the $2_3^+ \rightarrow 2_1^+ \rightarrow 0_{gs}^+$ transition, which proceeds through the emission of a 859.9 keV gamma ray in coincidence with the 334.0 keV gamma ray. The accumulated data are shown in Figure 5.3 (c.) and (d.). The $\epsilon_{\gamma\gamma}$ for this transition is (0.275±0.014)%, and the branching ratio is 45%. The background is 0.8 counts per keV. In spectrum (b.), another coincidence peak associated with the 332.0 keV gamma ray in the decay of ^{228}Ac can be seen at 824.9 keV. With 4 counts in the region of interest , a positive signal is not detected. The half-life limit is found to be $T_{1/2} > 3.79 \times 10^{19}$ years.

Finally, the transition $0_2^+ \rightarrow 2_1^+ \rightarrow 0_{gs}^+$ proceeds through the emission of a 921.1 keV gamma ray in coincidence with the 334.0 keV gamma ray. The accumulated data are shown in Figure 5.3 (e.) and (f.)). The $\epsilon_{\gamma\gamma}$ for this transition is (0.595±0.030)%, and the branching ratio is 91%. The background is 0.8 counts per keV. The only peak in this spectrum is at 911.0 keV which is a Compton scattering coincidence peak. With 6 counts in the region of interest a positive signal is not detected. The half-life limit is found to be $T_{1/2} > 9.17 \times 10^{19}$ years.

5.3 Conclusions

The results from the counting of ^{150}Nd for 391 days by the TUNL-ITEP double-beta decay setup at Kimballton Underground Research Facility have been presented. These results are the culmination not only of over a year of experimental counting time, but also several years of preparation and establishment of TUNL's first remote

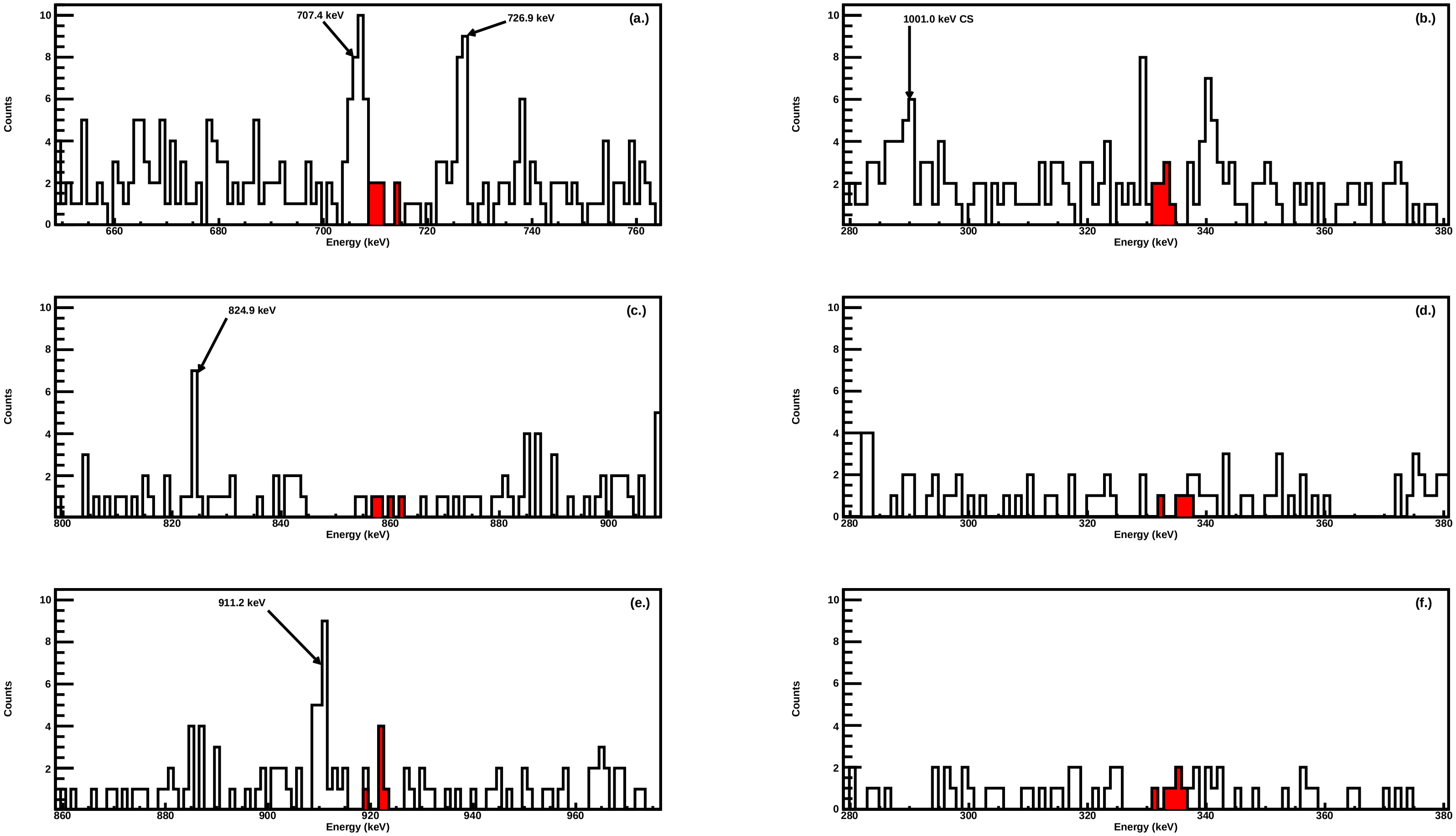

FIGURE 5.3: Coincidence data for the higher excited states. Spectra (a.) and (b.) are in coincidence with 334.0 keV and 712.2 keV, respectively, (c.) and (d.) are in coincidence with 334.0 keV and 859.9 keV, respectively, and (e.) and (f.) are in coincidence with 334.0 keV and 921.2 keV, respectively. The coincidence-energy window is ± 3.0 keV.

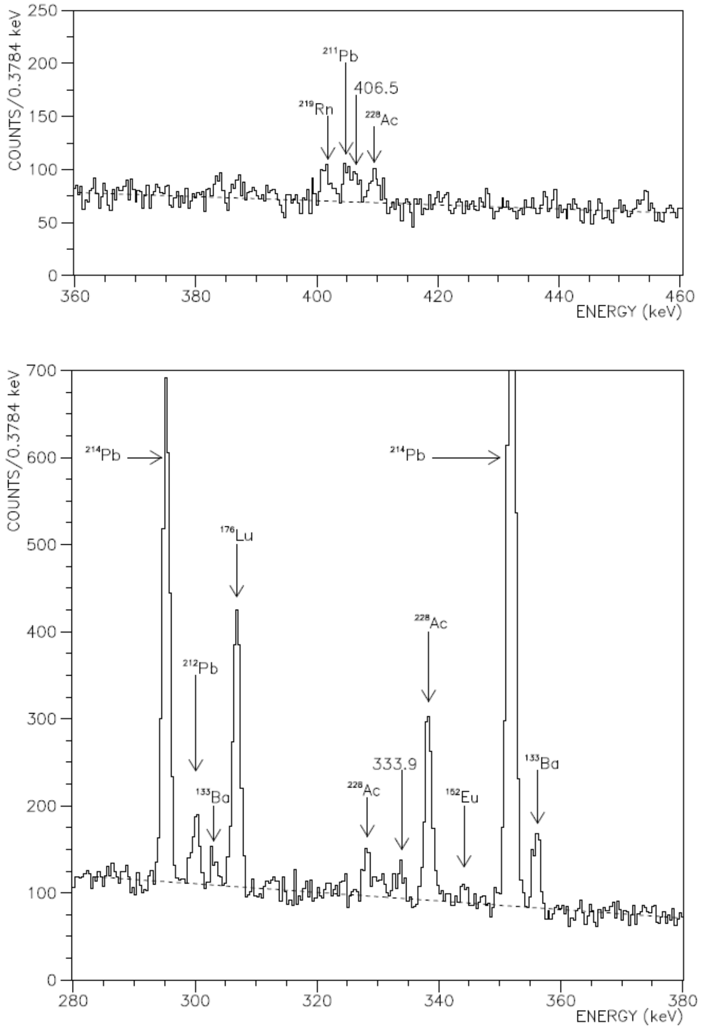

FIGURE 5.4: Results from Barabash *et al.* [6].

underground laboratory. The significance of this result will now be discussed.

The major result from this experiment is the observation of the 334.0 keV - 406.5 keV coincidence which confirms the double-beta decay of ^{150}Nd to the 0_1^+ state of ^{150}Sm. Though this decay has been observed recently by Barabash *et al.* [6], this is the first measurement which confirms that the coincidence has taken place.

Though the setup of Barabash *et al.* is rather simple, employing only one HPGe detector, there are still inherent difficulties to making a low-background measurement. Because of the coincidence mechanism used in the present work, there were many potential background candidates which could be discarded from the start. These background candidates continue to plague the measurement made by Barabash *et al.* [6], who rely on observation of the 334.0 keV or 406.5 keV peak in a singles spectrum, as shown in Figure 5.4. The reliability of this result is dependent upon the fit to the background spectrum and the simulation of the potential contaminants in the regions of interest. Their result, $T_{1/2} = 1.33^{+0.36}_{-0.23}(stat.)^{+0.27}_{-0.13}(syst.) \times 10^{20}$ years does agree within error to the present result, $T_{1/2} = (0.72^{+0.36}_{-0.18} \pm 0.04(syst.)) \times 10^{20}$ years. As mentioned in Section 2.4.1, the agreement with the theoretical prediction is about an order of magnitude off, but considering the significant uncertainty in theoretical calculations, this is not so bad.

The limits to the excited states are summarized in Table 5.1 and include limits determined by Barabash *et al.* [6]. The limits determined in [6] are about an order of magnitude better than the limits found in the present work. Roughly, this can be accounted for by comparing the exposure time × efficiency for each transition in [6] and the present work. The exposure in [6] is 1732 kg-h, compared to the exposure in the present experiment of about 375 kg-h. In addition, the efficiency in a singles experiment is considerably higher than in a coincidence measurement.

There are steps which could be taken to attempt to improve the effectiveness of the current setup. The move underground significantly decreased cosmic-ray related background. A major reduction in the background surrounding the regions of interest would be best accomplished by removing the ^{232}Th daughters from the ^{150}Nd sample. Though steps were taken which removed much of the ^{232}Th itself, ^{228}Ra is still present, which feeds the short-lived ^{228}Ac that contributes the most in the region of interest. ^{228}Ra has a half life of 5.75 years, so over time this contamination will die away. If more material could be obtained without decreasing the coincidence

Transition	Gamma-Ray Energies (keV)	Efficiency (%)	$T_{1/2}$ ×10^{20} y (this work)	$T_{1/2}$ ×10^{20} y [6]
$0_1^+ \rightarrow 2_1^+ \rightarrow 0_{gs}^+$	334.0-406.5	0.992±0.051	$(0.72^{+0.36}_{-0.18} \pm 0.04(syst.))$	$1.33^{+0.36}_{-0.23}(stat.)^{+0.27}_{-0.13}(syst.)$
$2_2^+ \rightarrow 2_1^+ \rightarrow 0_{gs}^+$	334.0-712.2	0.275±0.014	> 0.217	> 8.0
$2_3^+ \rightarrow 2_1^+ \rightarrow 0_{gs}^+$	334.0-859.9	0.275±0.014	> 0.379	> 5.4
$0_3^+ \rightarrow 2_1^+ \rightarrow 0_{gs}^+$	334.0-921.2	0.595±0.030	> 0.971	> 4.7

Table 5.1: A summary of the results found in this work and compared to [6].

detection efficiency some improvement could be gained.

Another improvement could be made by more thoroughly purging the radon from the detector cavity. The temporary purge which was set up initially did seem to have some small effect over time. A radon-purge tent would be one way to refine this effect.

A duplicate setup is currently being constructed in the LBCF at TUNL. In this setup, clover detectors will be used which will allow for segmentation cuts on the coincidence data. This should allow for a greater efficiency in detecting the coincidence events, as there will be more coverage of the angular distribution. For example, in the TUNL-ITEP double-beta decay setup, gamma rays emitted at an angle such that the energy of both are deposited in one detector do not register as a double-beta decay occurence. The use of the clover detectors will allow for a coincidence between individual segments so that such events can be discerned.

There are lessons to be learned from this counting experiment for future large-scale double-beta decay experiments using ^{150}Nd. At the time of writing, SNO+ is planning to use natural neodymium in their search for $0\nu\beta\beta$ decay in ^{150}Nd. However, if in the future they decide to use an enriched sample, the contaminants found in the present sample can serve as an example for the types of backgrounds to be expected. Efforts to either refine the enrichment process, or improve the purification process would need to be made.

Finally, throughout the analysis of this data, it was noted that there is a significant dearth of published gamma-ray coincidence data. Interpretation of this type of data could be very useful because of the ability to detect very low amounts of radiation through coincidences. This type of analysis could be utilized toward nuclear non-proliferation purposes.

Bibliography

[1] Mohammad Ahmed. `http://www.tunl.duke.edu/~daq/node47.html`, 2003.

[2] V. Artemiev, E. Brakchman, A. Karelin, V. Kirichenko, A. Klimenko, O. Kozodaeva, V. Lubimov, A. Mitin, S. Osetrov, V. Paramokhin, A. Pomansky, A. Smolnikov, T. Tsvetkova, S. Vasilyev, and O. Zeldovich. Half-life measurement for ^{150}Nd $2\beta 2\nu$ decay in the time projection chamber experiment. *Phys. Lett. B*, 345:564, 1995.

[3] A. S. Barabash. Average and recommended half-life values for two-neutrino double-beta decay: Upgrade '05. *Czech. J. Phys.*, 56(5):437–445, April 2006.

[4] A. S. Barabash. Double beta decay: present status. *arXiv:0807.2948*, July 2008.

[5] A. S. Barabash, F. Hubert, Ph. Hubert, and V. I. Umatov. Double beta decay of ^{150}Nd to the first 0^+ excited state of ^{150}Sm. *JETP Letters*, 79, 2004.

[6] A. S. Barabash, Ph. Hubert, A. Nachab, and V. Umatov. Investigation of $\beta\beta$ decay in ^{150}Nd and ^{148}Nd to the excited states of daughter nuclei. *Phys. Rev. C*, 79, 2009.

[7] J. Barea and F. Iachello. Neutrinoless double-β decay in the microscopic interacting boson model. *Phys. Rev. C*, 79:044301, 2009.

[8] Felix Boehm and Petr Vogel. *Physics of Massive Neutrinos.* Cambridge University Press, Cambridge, England, 1992.

[9] O. Castanos, J. G. Hirsch, O. Civitarese, and P. O. Hess. Double-beta decay in the pseudo SU(3) scheme. *Nucl. Phys.*, A571:276, 1994.

[10] E. Caurier. Shell model and nuclear structure. *Progress in Particle and Nuclear Physics*, 59:226, 2007.

[11] National Nuclear Data Center. `http://www.nndc.bnl.gov/chart/`, 2009.

[12] David O. Caldwell (Ed.). *Current Aspects of Neutrino Physics.* Springer, New York, 2001.

[13] C. Arpesella *et al.* Search for $\beta\beta$ decay of ^{96}Zr and ^{150}Nd to excited states of ^{96}Mo and ^{150}Sm. *Europhysics Letters*, 27:29, 1994.

[14] C. Arpesella *et al.* Looking for double beta decay of ^{150}Nd to excited states of ^{150}Sm by gamma ray spectroscopy. *Nucl. Phys. B (Proc. Suppl.)*, 70:249, 1999.

[15] M. C. Perillo Isaac *et al.* Preliminary results from a study of the double beta decay of ^{150}Nd. *Nucl. Phys. B (Proc. Suppl.)*, 48:244, 1996.

[16] M. Shibata *et al.* Beta-decay half-lives and level ordering of ^{102m,g}Rh. *Appl. Radiat. Isot.*, 49:1481, 1998.

[17] NEMO Collaboration: J. Argyriades *et al.* Measurement of the double beta decay half-life of ^{150}Nd and search for neutrinoless decay modes with the NEMO-3 detector. *arXiv:0810.0248v1*, October 2008.

[18] A. Franklin. *Are There Really Neutrinos?* Allan Franklin, New York, 2001.

[19] W. H. Furry. On transition probabilities in double beta-disintegration. *Phys. Rev.*, 56:1184, 1939.

[20] Gordon Gilmore. *Practical Gamma-ray Spectrometry.* John Wiley & Sons, Inc., West Sussex, England, 2008.

[21] M. Goeppert-Mayer. Double-beta disintegration. *Phys. Rev.*, 48:512, 1935.

[22] Particle Data Group. `http://pdg.lbl.gov/2009/reviews/rpp2009-rev-probability.pdf`, 2009.

[23] M. J. Hornish, L. De Braeckeleer, A. S. Barabash, and V. I. Umatov. Double beta decay of ^{100}Mo to excited final states. *Phys. Rev. C*, 74:044314, 2006.

[24] Masaharu Hoshi, Takanori Shimoshige, and Yaskukazu Yoshizawa. Nuclear structure study of ^{150}Sm. *J. Phys. Soc. Jap.*, 42:1091, 1977.

[25] F. T. Avignone III, S. R. Elliott, and J. Engel. Double beta decay, majorana neutrinos, and neutrino mass. *Rev. Mod. Phys.*, 80:481, 2008.

[26] M. F. Kidd, J. H. Esterline, and W. Tornow. Double beta decay of ^{150}Nd to excited final states. *TUNL Progress Report*, XLVI:22, 2007.

[27] M. F. Kidd, J. H. Esterline, and W. Tornow. Double-electron capture on ^{112}Sn to the excited 1871 keV state in ^{112}Cd: A possible alternative to double-beta decay. *Phys. Rev. C*, 78:035504, 2008.

[28] M. F. Kidd, J. H. Esterline, and W. Tornow. New results for double-beta decay of ^{100}Mo to excited final states of ^{100}Ru using the TUNL-ITEP apparatus. *Nucl. Phys. A*, 821:251–261, 2009.

[29] A. A. Klimenko, S. B. Osetrov, A. A. Smolnikov, and S. I. Vasiliev. Double-beta decay of ^{150}Nd and ^{76}Ge to excited states. *Gzech. J. of Phys.*, 52:589, 2002.

[30] A. A. Klimenko, A. A. Pomansky, and A. A. Smolnikov. Low background scintillation installation for double beta decay experiments. *Nucl. Inst. Meth. B*, 17:445, 1986.

[31] Glenn F. Knoll. *Radiation Detection and Measurement.* John Wiley & Sons, Inc., Hoboken, New Jersey, 2000.

[32] J. Kotila, J. Suhonen, and D. S. Delion. Description of the two-neutrino $\beta\beta$ decay of ^{100}Mo by pnMAVA. *J. Phys. G: Nucl. Part. Phys.*, 37, 2010.

[33] K. S. Krane. *Introductory Nuclear Physics.* J. Wiley & Sons, New York, 1988.

[34] Ch. Kraus, B. Bornschein, L. Bornschein, J. Bonn, B. Flatt, A. Kovalik, B. Ostrick, E. W. Otten, J. P. Schall, Th. Thummler, and Ch. Weinheimer. Final results from phase II of the Mainz neutrino mass search in tritium β decay. *Eur. Phys. J. C*, 40, 2005.

[35] E. Majorana. Teoria simmetrica dell'elettrone e del positrone. *Nuovo Cimento*, 14:171, 1937.

[36] R. N. Mohapatra and P. B. Pal. *Massive Neutrinos in Physics and Astrophysics.* World Scientific, Singapore, 1998.

[37] A. Morales, J. Morales, R. Nunez-Lagos, J. Puimedon, J. A. Villar, A. Larrea, and E. Garcia. A search of the neutrinoless decay of ^{76}Ge to the first excited state of ^{76}Se in the Canfranc tunnel. *J. Phys. G.: Nucl. Part. Phys.*, 17:S211, 1991.

[38] Direct Observation of NU Tau. `http://www-donut.fnal.gov/`, 2001.

[39] National Institute of Standards and Technology. `http://physics.nist.gov/PhysRefData/Xcom/Text/XCOM.html`, 2009.

[40] Donald H. Perkins. *Introduction to High Energy Physics.* Cambridge University Press, Cambridge, 2000.

[41] G. Racah. Sulla simmetria tra particelle e antiparticelle. *Nuovo Cimento*, 14:327, 1937.

[42] F. Reines. The neutrino: from poltergeist to particle. *Rev. Mod. Phys.*, 68:317, 1991.

[43] A. De Silva, M. K. Moe, M. A. Nelson, and M. A. Vient. Double β decays of ^{100}Mo and ^{150}Nd. *Phys. Rev. C*, 56:2451, 1997.

[44] J. Suhonen. Two-neutrino double beta decay to excited states. *Czech. J. Phys.*, 48:253, 1999.

[45] Páll Theodórsson. *Measurement of Weak Radioactivity.* World Scientific, Singapore, 1996.

[46] S. I. Vasil'ev, A. A. Klimenko, S. B. Osetrov, and A. A. Smol'nikov. Experimental search for double beta decay of ^{96}Zr to excited levels of ^{96}Mo. *JETP Lett.*, 61:358, 1995.

[47] M. Saleh Yousef, V. Rodin, A. Faessler, and F. Simkovic. Matrix elements of two-neutrino double beta decay in deformed nuclei. *Nucl. Phys. B (Proc. Suppl.)*, 188:56, 2009.

Biography

Mary Frances Kidd was born in Kingsport, Tennessee on February 14, 1982. She graduated from Tennessee Technological University with a B.S. in Physics in 2004, after which she began attending graduate school at Duke University. She was a teaching assistant from 2004-2006, and a graduate research assistant from 2007-2010. She completed a M.A. in Physics from Duke University in 2007. In 2009, she became a Henry W. Newson Fellow. After earning her PhD from Duke University, she will begin a postdoctoral position at Los Alamos National Laboratory in New Mexico.

Publications

1. M. F. Kidd, J. H. Esterline, W. Tornow, A. S. Barabash, V. I. Umatov, "New results for double-beta decay of ^{100}Mo to excited final states of ^{100}Ru using the TUNL-ITEP apparatus," Nuclear Physics **A821**, 251 (2009).
2. M. F. Kidd, J. H. Esterline, W. Tornow, "Double-electron capture on ^{112}Sn to the excited 1871 keV state in ^{112}Cd: A possible alternative to double-beta decay," Phys. Rev. C **78**, 035504 (2008).